

UNIVERSITÀ DEGLI STUDI DI PISA
FACOLTÀ DI INGEGNERIA

DIPARTIMENTO DI INGEGNERIA MECCANICA,
NUCLEARE E DELLA PRODUZIONE



TESI DI LAUREA
in
INGEGNERIA NUCLEARE

**Kinetics of phase growth during the Cu-Sn
diffusion process and the Nb₃Sn formation.
Optimization of superconducting properties.**

CANDIDATA
Sara Mattafirri

RELATORI
Prof. Carlo Angelini

Prof. Ing. Fabio Fineschi

Prof. Ing. Salvatore Lanza

Dott. Ing. Emanuela Barzi

Ing. Jean Michel Rey

26 Luglio 2002

ANNO ACCADEMICO 2001/2002

ACKNOWLEDGEMENTS

I would like to thank warmly all those who helped me so much during this year in Fermilab. In particular my supervisor Emanuela Barzi for guiding me enthusiastically day after day and for revising my thesis manuscript with extreme care, Jean Michel Rey for introducing me to the studies on the diffusion process in intermetallics, Alexander Zlobin for his precious advices and Jay Hoffmann for teaching me how to work in a material laboratory.

I also want to thank Crisitan Boffo who encouraged me in studying in depth many scientific aspects and provided helpful suggestions in writing my thesis manuscript and Alessandro Cerri who advised me in how to approach the error evaluation techniques.

Finally, many thanks to Peter Limon, Robert Kephart, Fabio Fineschi, Salvatore Lanza, Carlo Angelini, John Tompkins and Mike Lamm who gave me the unique opportunity to come and do research in such a great laboratory as Fermilab.

INDEX

ACKNOWLEDGEMENTS.....	i
------------------------------	----------

FOREWORD.....	vi
----------------------	-----------

1 THE TEVATRON AND BEYOND.....	1
---------------------------------------	----------

1.1 Introduction.....	1
-----------------------	---

1.2 High energy accelerators	2
------------------------------------	---

1.3 Next generation machines.....	4
-----------------------------------	---

1.4 Superconducting magnets	6
-----------------------------------	---

1.5 Other applications of superconductivity	9
---	---

1.5.1 Magnetic resonance imaging	9
--	---

1.5.2 Energy storage	9
----------------------------	---

1.5.3 Controlled thermonuclear fusion	10
---	----

1.5.4 Magnetohydrodynamic power generation	11
--	----

1.5.5 DC motors and AC machines	11
---------------------------------------	----

1.5.6 Magnetic levitation	12
---------------------------------	----

1.5.7 Power Transmission Lines.....	12
-------------------------------------	----

1.6 Summary	13
-------------------	----

2 SUPERCONDUCTIVITY.....	14
---------------------------------	-----------

2.1	Introduction.....	14
2.2	Meissner effect and London equations	18
2.3	Thermodynamics properties	21
2.3.1	Thermodynamic critical field of bulk materials	23
2.3.2	Superconductivity as a phase transition.....	23
2.4	Cooper pairs.....	24
2.5	Type II Superconductors.....	26
2.6	Magnetic flux quantization	31
2.7	Hard superconductors	32
2.7.1	Flux pinning.....	32
2.7.2	Magnetization of a hard superconductor	33
2.7.3	Critical state model	34
3	SUPERCONDUCTING MATERIALS.....	36
3.1	Introduction.....	36
3.2	Conductors for use in magnet.....	38
3.2.1	Degradation and training	38
3.2.2	Copper stabilization	39
3.2.3	Flux jumping.....	40
3.2.4	Filamentary composites	41
3.3	Niobium Titanium.....	42
3.4	Niobium Tin.....	44
3.4.1	The bronze process	46
3.4.2	The internal tin process.....	47
3.4.3	The modified jelly roll process	49
3.4.4	The powder in tube process	51
3.5	Magnet winding and heat treatment approach.....	53
3.6	Summary.....	56
4	GROWTH KINETICS OF INTERMETALLIC COMPUONDS BY DIFFUSION PROCESS	58

4.1	Introduction.....	58
4.2	Formation of intermetallics by diffusion process	59
4.3	Diffusion coefficient and activation energy.....	65
4.4	Mechanism of diffusion in intermetallics	73
4.5	Nb ₃ Sn formation	76
4.5.1	Thermodynamic considerations.....	75
4.5.2	Nb ₃ Sn layer growth.....	78
4.6	Cu-Sn intermetallic compounds.....	80
4.7	Summary	83
5	INTERMETALLIC LAYER MEASUREMENTS	84
5.1	Introduction.....	84
5.2	Cu-Sn samples	85
5.2.1	Cu-Sn models design	85
5.2.2	Cu-Sn casting technique	87
5.2.3	Cu-Sn samples heat treatment procedure.....	90
5.3	Nb-Sn-Cu samples	91
5.3.1	Nb-Sn-Cu samples design.....	91
5.3.2	Nb-Sn-Cu samples heat treatment procedure	93
5.4	Samples preparation for microscopic analysis.....	93
5.4.1	Strands mold for optical microscopy	94
5.4.2	Strand Mold for Scanning Electron Microscopy	95
5.4.3	Samples cut.....	95
5.4.4	Samples polishing	96
5.5	Layer thickness measurement experimental method.....	97
5.6	Summary	99
6	CRITICAL CURRENT MEASUREMENT	101
6.1	Introduction.....	101
6.2	Critical current measurements experimental set up	101
6.2.1	The magneto cryostat.....	102

6.2.2	Electronics and data acquisition software.....	103
6.3	Sample preparation	105
6.4	Probe for critical current measurements.....	107
6.5	Experimental evaluation of I_c and J_c	109
6.6	n value and residual resistivity ratio	110
6.6.1	n value.....	110
6.6.2	RRR	111
6.7	B_{c20} Evaluation.....	112
6.8	Summary	113
7	ERRORS EVALUATION	114
7.1	Introduction.....	114
7.2	Errors on the thickness measurement	115
7.2.1	Statistical errors on the Cu-Sn phases thickness.....	115
7.2.2	Statistical errors on the Nb_3Sn	119
7.2.3	Systematic errors on the Cu-Sn phases thickness.....	119
7.2.4	Systematic errors on the Nb_3Sn thickness	127
7.3	Errors on temperature	129
7.4	Errors on time	129
7.5	Errors on I_c and J_c	130
7.6	Errors on B_{c20}	132
7.7	Summary	133
8	RESULTS ON THE CU-SN SYSTEM.....	135
8.1	Introduction.....	135
8.2	Cu-Sn phase growth over the Cu-Sn models.....	136
8.2.1	Diffusion model	136
8.2.2	Heat treatments	137
8.2.3	Diffusion sample observation	138
8.2.4	Phase growth kinetics and E and k_0 evaluation.....	142

8.2.5	Discussion.....	146
8.3	Cu-Sn growth kinetics over the strands	147
8.3.1	Heat treatments	148
8.3.2	Samples observation and comparison between the thickness growths.....	148
8.3.3	Discussion about the Growth comparison	154
8.3.4	Discussion about the heat treatment optimization	155
8.4	Effecte of partly reacting Nb ₃ Sn before winding on the strand critical current.....	156
8.5	Summary.....	159
9	RESULTS ON THE Nb₃Sn FORMATION AND SUPERCONDUCTING PROPERTIES	161
9.1	Introduction.....	161
9.2	Nb ₃ Sn growth kinetic investigation	162
9.2.1	Heat treatments	163
9.2.2	Diffusion samples observation.....	165
9.2.3	Nb ₃ Sn Growth Kinetic.....	166
9.3	Superconducting properties	170
9.3.1	I_c, J_{cl}, B_{c20} for IT strand.....	170
9.3.2	RRR and n value for IT strand	174
9.3.3	I_c, J_{cl}, B_{c20} for PIT strand.....	175
9.3.4	RRR and n value for PIT strand	178
9.3.5	Discussion.....	179
9.4	Summary.....	182
	CONCLUSIONS.....	184
	APPENDIX A (E and k_θ : fit results).....	186
	APPENDIX B: (Cu-Sn growth kinetics in MJR strand)	189
	APPENDIX C: (IT and PIT SC in function of the Nb₃Sn area)	190
	BIBLIOGRAPHY	194

FOREWORD

A strong effort to develop new high field superconducting magnets for next generation accelerators is presently invested in the High Field Magnet Project (HFM) of the Technical Division at Fermilab. This thesis work was performed within the Strand and Cable R&D program, whose main task is the development of high J_c superconducting strands and cables that could achieve the requirements for the future generation of accelerator magnets. This mission is pursued in collaboration with industry, universities, and other National Laboratories.

A delicate step in Nb_3Sn magnet technology is the high temperature heat treatment needed to form the superconducting phase by diffusion process in Nb/Sn composite strands.

To optimize the low temperature stages, performed on the strands to diffuse the Sn in the Cu matrix, the kinetics of phase growth in the Cu-Sn system was studied. The diffusion constants of the Cu-Sn intermetallic phases were evaluated using Cu-Sn models. Then the behavior of strands produced with the Internal Tin and the Modified Jelly Roll technologies was studied and compared with the model predictions.

To optimize the high temperature stage of the cycle, the growth of the Nb_3Sn intermetallic compound was investigated for two different strand designs (Internal Tin and Powder-in-Tube) as a function of heat treatment time and temperature. In addition, for both strands the critical current density at 4.2 K was measured as a function of magnetic field, and the upper critical field was evaluated for all heat treatment temperatures and times.

Furthermore, the feasibility of winding partly reacted cables to reduce the magnet manufacturing time and cost was also explored.

CHAPTER

I

THE TEVATRON AND BEYOND

1.1 INTRODUCTION

A strong effort is presently spent at Fermilab in developing new high field superconducting magnets for next generation accelerators. The vanishing electrical resistance of superconducting coils and their ability to provide magnetic fields far beyond those of saturated iron is the main motivation for the use of superconductor technology in all new large proton, antiproton and heavy ion circular accelerators. Superconductivity does not only open the way to much higher particle energies, but at the same time leads to a substantial reduction of operating costs. Beam energies in the TeV regime are hardly accessible with standard technology, due to the enormous power they would require. The electrical power consumption of an accelerator cryogenic plant may easily be 1-2 orders of magnitude lower than the power needed in an equivalent warm machine of the same energy. In this chapter some highlights on superconducting magnets and other superconductors applications are described.



Figure 1.1 Fermilab site.

1.2 HIGH ENERGY ACCELERATORS

A discussion of the scientific motivations of the strong effort going on all over the world to build accelerators of higher and higher energy is beyond the scope of this thesis. Still the main themes of today's particle physics are mentioned here below.

High energy machines are mainly motivated by the need of understanding the origin of symmetry breaking of electroweak interactions of elementary particles, the origin of their masses and of the masses of the force carriers, the reason why matter predominates over anti-matter in the universe. Besides completing our present understanding of the Standard Model, future observations will also hopefully lead to extend the theory and eventually reach the unification of gravity with the other forces. New observations might also lead to understand what is the composition of dark matter in the universe. Most of these searches are carried out by smashing particles of very high energy into each other, and by analyzing the nature and the characteristics of the new particles produced at the expense of the collision energy. These interactions are obtained

either by blasting high momentum particles onto a fixed target or by making them collide head-on among themselves. In head-on colliders, in order to achieve high event rates, the particles are bunched together and the bunches are formatted into high intensity beams. For the deepest studies of particle structures and for the production of more massive new particles, higher and higher energies are needed, and of course the more complex are the accelerators. Accelerators can be divided in two types:

- Linear accelerators;
- Circular accelerators.

In a linear accelerator, charged particles travel along a straight trajectory and go through a number of accelerating structures. An outstanding example is the 45 GeV electron/positron LINAC at SLAC, Stanford University, CA, USA. In the last years the possibility of building an e^+/e^- linear accelerator as the next “big machine” has become more feasible within the scientific community. Two international projects are trying to fix the energy limit for these machines to the TeV level. The first one is the Next Linear Collider (NLC) a 32 Km long warm accelerator mostly supported by a US – Japan collaboration. The second is TESLA (TeV Energy Superconducting Linear Accelerator) a 33 Km long superconducting accelerator mostly supported by the European countries. Moreover two other projects are pursued: CLIC (Compact Linear Collider) at CERN and JLC at KEK. The amount of money and the effort necessary to design and build these accelerators pushes the international community to create strong collaborations while Fermilab is one of the most probable candidate sites for the realization of these machines.

In a circular accelerator, the beam is circulated many times in a closed orbit along which a number of accelerating stations are present. Bending magnets and focusing elements are distributed over the accelerator arcs to keep the particles, during acceleration, on the same orbit and within the accelerator acceptance. Beside Fermilab's Tevatron, LHC at CERN, Geneva, Switzerland, and HERA at DESY, Hamburg, Germany, are examples of circular accelerators. Tevatron is a 1 km radius superconducting ring able to accelerate protons and antiprotons to a maximum energy of 1 TeV.

LHC is under construction and will be completed in 2006. It is a proton-proton Collider of maximum energy 7x7 TeV. HERA is a proton-electron collider, whose superconducting proton ring has an energy of 820 GeV, whereas its electron/positron ring has an energy of 28 GeV.

1.3 NEXT GENERATION MACHINES

In a few years (possibly in 2006), the LHC proton-proton collider at CERN will operate in the circular tunnel where LEP was in function until the 2001. For a given accelerator energy the two parameters that can be adjusted, the radius of the machine and the field of its magnets, are not independent of each other. The higher the field in the magnets, the smaller is the machine. With a circumference of 27 km and an 8.4 T bending magnetic field, the LHC proton beams will reach a maximum energy of 7 TeV each. Since the LHC collides protons on protons, special "2 in 1" magnets are employed, which accommodate the two separate beams circulating in opposite directions. Being the machine approximately circular, bending radius, bending field, and beam energy are related by the simple relationship:

$$E_{GeV} = 0.3qB_m r, \quad (1.1)$$

where:

q is the particle charge [units of electron charge],

B_m is the bending field of the magnets [T],

r is the radius of the circular accelerator [m].

A fraction of the LHC magnets are being built in the US, and Fermilab is the most important center for the US LHC project. Superconducting NbTi technology was chosen for the LHC magnets, as was done for the Tevatron first and for HERA next, with maximum dipole fields of 4.5 T and 6.2 T respectively. The nominal operating field of LHC is 8.4 T. Because of their higher field, the use of superconducting magnets allows for reduction of tunneling costs. However as the field increases, better superconductor properties are required, raising costs again. Superconducting NbTi is a ductile alloy

which is ideal for manufacturing composite strands, for making cables out of them, and eventually wind magnet coils. Nevertheless, with an upper critical field (see Chapter 2) of about 11.5 T at 4.2 K, the LHC NbTi coils would have to be pushed near their critical current limits to operate at 8.4 T. A safe operation point was achieved at LHC by lowering the magnet operating temperature to 1.9 K (superfluid helium). At this temperature the NbTi upper critical field rises to 14 T. This choice moved the technological effort more onto the cryogenic system than on the superconducting material R&D.

More cost-effective solutions are presently being studied for a post-LHC Very Large Hadron Collider (VLHC) [1, 2]. At the Snowmass_96 Summer Study on New Directions for High Energy Physics (HEP), a goal was set of a 50 TeV x 50 TeV proton-proton collider with a 3 TeV injector. Fermilab could possibly have been the site for the VLHC. Figure 1.2 shows how the new machines could have been integrated at Fermilab [3]. In 2001 a detailed Design study for a Staged Very Large Hadron Collider was presented.

A two stage project have been proposed in order to allow the reduction of costs and the possibility to commission the machine in a reasonable time scale while pushing the energy level to the cutting edge limits.

A 233 km long tunnel will initially accommodate low field super-ferric magnets in order to reach an energy of 40 TeV. These magnets will be replaced during the second stage (after the scientific potential of the first stage will be fully realized) by 12T high filed magnets that will allow to reach an energy of 175 TeV with twice the luminosity.

Whereas for the low field magnets NbTi can be used, in the case of the high field option other kinds of superconductors have to be considered. Multifilamentary Nb₃Sn is one of the most promising materials. Strand and cable R&D is actively pursued by Fermilab within the High Field Magnet Project (HFM), using different Nb₃Sn technologies and as a benchmark, the strand design developed for the International Thermonuclear Experimental Reactor (ITER).

1.4 SUPERCONDUCTING MAGNETS

Keeping the charged particles confined around a circular orbit requires both bending and focusing forces generated by electromagnetic fields. The Lorentz force is given by:

$$\vec{F} = e(\vec{E} + \vec{v} \times \vec{B}), \quad (1.2)$$

where :

E is the electric field,

e is the electron charge,

v is the particle velocity, and

B is the magnetic field.

The electric term in equation 1.2 must be used for acceleration, while the magnetic term that does not generate work can only be used for bending. At high energy, where $v=c$, a magnetic field of barely 1 T generates the same Lorentz force as an electric field of 3×10^8 V/m. Although they do not increase the particle energy, magnetic field are thus very effective in bending the trajectory. Magnetic dipole fields perpendicular to the plane of the particle trajectory are used to bend the beams. Quadrupole fields around the beam axis focus the particles, and longitudinal electric fields are used to accelerate them.

A noticeable difference to be taken into account in comparing a conventional and a superconducting magnet is that in the former the field is present almost only in the iron sector, while in the latter the field surrounds the entire space around it. This configuration significantly constraints the choice of the structural materials.

The focusing lattice most frequently used in a circular accelerator is a series of identical cells, each containing a focusing (F) and defocusing (D) quadrupole magnets separated by drift (O) spaces (FODO lattice). In between the focusing cells are positioned the dipole bending magnets. This structure is called separated function, to distinguish it from systems with integrated functions, where the bending magnets have radial dependent bending field that is also capable of performing the required focusing. Using magnets with separated functions allows greater design and operation flexibility.

The challenging requirements in superconducting magnet design are [4]:

- Field strength. The general rule is the higher the field strength, the better. Not only bending, but also focusing and defocusing is more efficient at higher fields;

- Field quality. Since the beam has to circulate many times around the same orbit, small imperfections in the field decrease the beam lifetime;
- Magnet bore size. The cost of the magnet increases dramatically with the bore size. However, from the point of view of beam acceptance, the larger the bore size, the better it is. At high energy, the beam size can be small but induced fields misalignments and other factors may force to make the acceptance much larger than beam size;
- AC-DC behavior. To keep the particle in orbit during acceleration, the magnets have to be ramped. However at maximum beam energy and in collider mode operation, the field must be very stable for many hours;
- Radiation hardness. The magnet has to survive in a high radiation area for the entire expected life of the machine;
- Reliability. The malfunctioning of a single magnet can cause the loss of the entire beam. With more than one thousand magnets in the ring, this clearly imposes strict reliability requirements on each of them.
- Cost. Because of the large number of magnets, both their production and their maintenance cost should be kept as low as possible.

Despite the anticipated strong saving in operating cost, the introduction of superconducting magnets generated other problems like:

- Persistent eddy currents. Eddy currents in the superconducting filaments are induced during the magnet current ramp. Because of the vanishing resistance of the material, they do not decay and generate dipolar and higher multipolar fields;
- Quench behavior. If one of the critical parameters in the superconductor is exceeded the magnet quenches to the normal resistance state. The machine must be protected from possible damage, and must be able to recover quickly from quenches;
- Cryogenics. An accurate study on the cryogenic plant and transport lines is needed in order to avoid high costs for refrigeration.

In a bending magnet of the high energy machines under consideration, the sagitta at the magnet exit is negligible with respect to the magnet length. Therefore the key elements of the magnet design are coil cross section and conductor distribution over it. Given bore

size and magnetic field, conductor volume and field quality should be optimized by a careful design of these parameters.

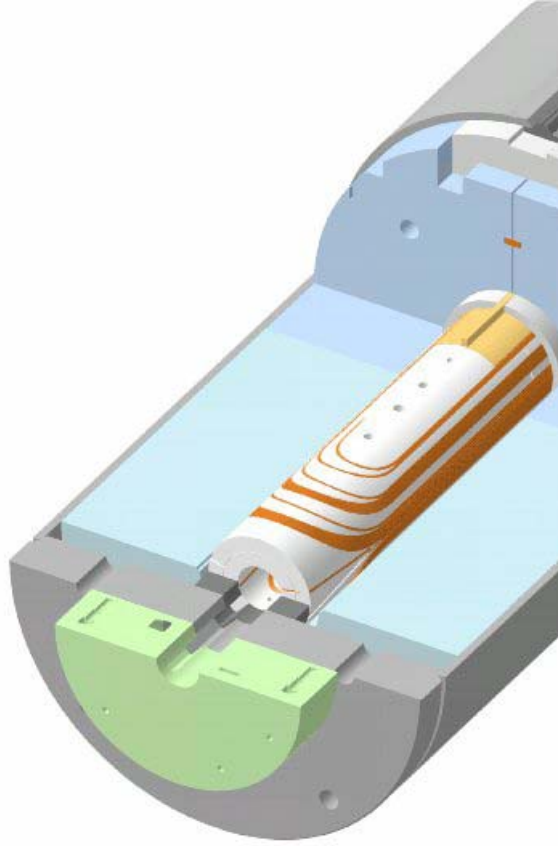


Figure 1.2 Cos(θ) design magnet

Presently two different magnet designs with different coil configurations are studied at the TD. The first one, Cos(θ), presents a complex distribution of the superconductor along the cross section that allows the maximization of the field inside the bore with optimal field quality. The second one, Common Coil, presents a simpler design that leads to cheaper production costs while more superconductor is necessary on the cross section to obtain the same field level of the Cos(θ). As already mentioned, field quality is also very important. This parameter directly affects beam optics and beam stability. Important sources of field errors are misalignments of the conductor and of the iron yoke on magnet cross section, iron saturation, coil deformation under Lorentz forces, and the superconductor magnetization.

1.5 OTHER APPLICATIONS OF SUPERCONDUCTIVITY

The realization of high field magnets for high energy physics is one of the most fascinating and difficult applications of superconductivity, but there are many other important fields in which superconductors can possibly be used. This is especially true, after the discovery in 1986 of high temperature superconductors, where T_c is greater than 77 K (liquid nitrogen temperature). Applications and present R&D projects include [5]:

- Magnetic resonance imaging;
- Energy storage;
- Controlled thermonuclear fusion;
- Magnetohydrodynamic power generation;
- DC motors and AC machines;
- Magnetic levitation;
- Power lines.

1.5.1 Magnetic resonance imaging

Superconducting magnets are used routinely in many hospitals in magnetic resonance imaging (MRI) applications. In this technique, a magnetic field is used to align the spins of hydrogen atoms (mostly contained in H_2O molecules), and an electromagnetic pulse is then given to excite spin orbit transitions. When the pulse is over, the spins go back to the original state emitting a characteristic electromagnetic wave. The wave can be detected by direction-sensitive sensors and used to create two-dimensional pictures of the human body. MRI is widely used to diagnose tumors, especially in sensitive parts of the body like the brain, where intrusive techniques are risky.

1.5.2 Energy storage

Storage superconducting magnets have been proposed as a large reservoir of energy (Superconducting Magnetic Energy Storage SMES) in order to balance the daily variations in the electricity demand. When the available electric power grid exceeds the demand, the SMES can adsorb and store energy. This electromagnetic energy can be dumped back into the network to satisfy increased demand during the peak hours.

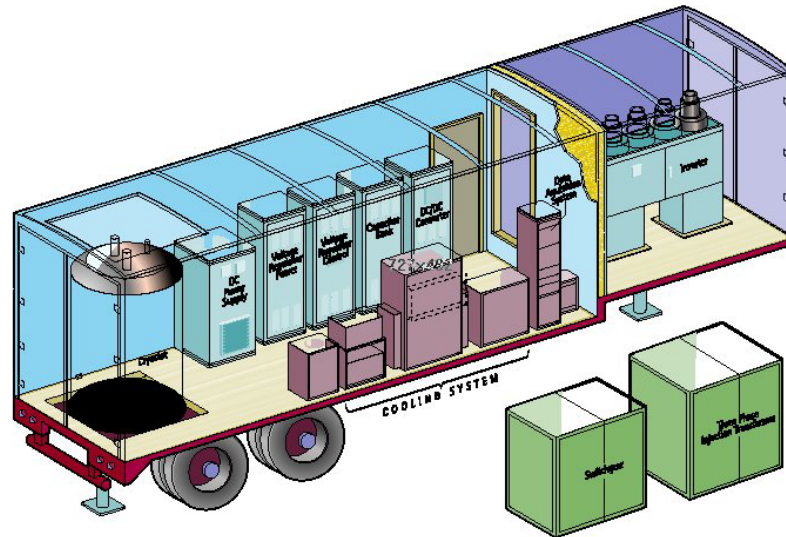


Figure 1.3 SMES

For years this device has been available only for military purposes, but with the improvement of the technology it is now possible to use SMES as a regular back up for factories that need reliable energy sources or to deliver energy to temporary locations with a portable device as shown in Figure 1.3.

1.5.3 Controlled thermonuclear fusion

Magnetic confinement of hot plasma may be the most promising way to achieve commercial production of power from controlled thermonuclear fusion. Given the extreme confinement fields required, superconducting coils are the only possible choice. The Joule loss of conventional copper magnets would be 100 times greater than the power required for refrigeration. The most advanced project in this field is ITER, a tokamak fusion reactor, shown in Figure 1.4.

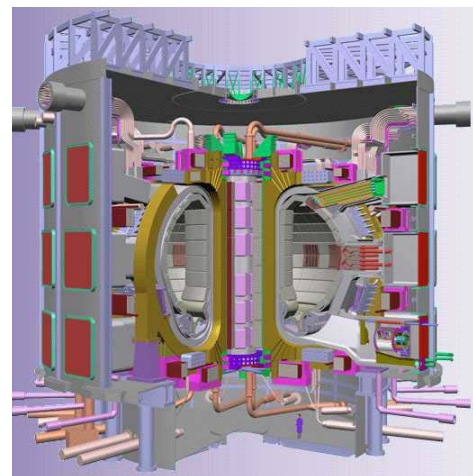


Figure 1.4 ITER design.

The magnetic field to confine and stabilize the high temperature plasma is generated by two types of coil systems: toroidal coils and poloidal coils. Fusion reactions take place when the plasma is sufficiently hot and dense, and contained long enough for the nuclei to start fusing together in an energy positive process. This international experiment is supported by Europe, Japan and Russia. USA decided to withdraw from the collaboration in 1998.

1.5.4 Magnetohydrodynamic power generation

Magnetohydrodynamic generation is a technique for the direct conversion of thermal to electrical energy. The principle of this method is based on the induction of an EMF by means of a transverse magnetic field in a hot gas flow, and subsequent extraction of a DC power. The purpose of using superconducting magnets is the same as for the fusion reactors, the energy produced has to exceed the power input. This technology will possibly become of commercial interest before thermonuclear fusion, contributing significantly to fossil fuel energy saving.

1.5.5 DC motors and AC machines

The superconducting technology applied to electric motors would allow to reduce sizes and to reach higher efficiency. The advantages are most evident in big motors, especially those for marine propulsion. The hardest problem is to build a rotating cryostat, and to transmit the torque between zones at room and at low temperature. The same problem has to be solved as for AC generators. In this case, the design of a cryostat rotating at 50-60Hz with a high centrifugal acceleration of some 5000g rises many technical issues. The introduction of high temperature superconductors helped in solving this problem and in 2001 a 5000 Hp AC motor was built by American Superconductors. In the near future some compact motors for naval propulsion will be available in the market for military applications.

1.5.6 Magnetic levitation

One of the most fascinating applications of superconductivity is magnetic levitation. The idea of designing vehicles floating on magnetic fields is not new, but the introduction of superconducting magnets made it approachable, by means of high magnetic fields, low weights, and low energy consumption. Magnetic levitation applied to train transport is especially pushed in Japan. Some prototypes have already been built, and a record speed of 577 km/h has been reached. Moreover a new project has started in the US with the goal to build a fast line to connect the big cities on the atlantic cost. The first step will be to connect Washington to Baltimore with future extension to Philadelphia and New York. The advantages of these vehicles are high speeds, no contact with the ground, no moving parts, and no noise.

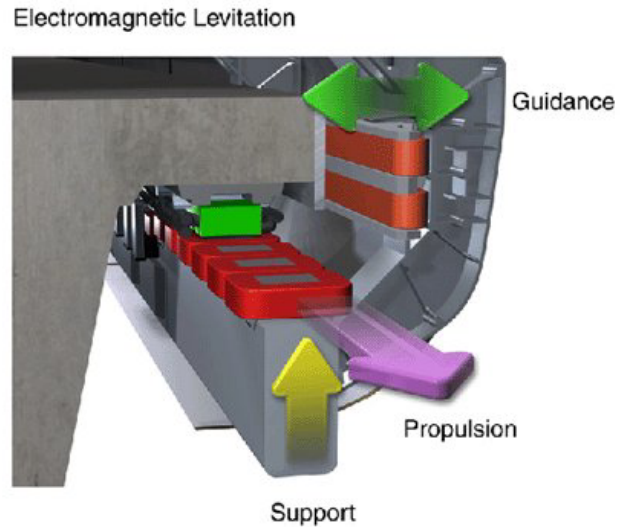


Figure 1.5 Magnetic levitation principle

1.5.7 Power Transmission Lines

The design and construction of high power transmission lines is one of the latest achievements for the Superconducting materials applications. Thanks to the development of high temperature superconductors (HTS) is now possible to build cables able to carry MWatts with almost zero losses and without the need of costly helium

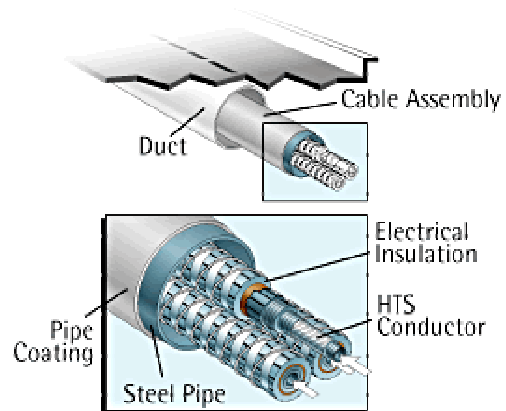


Figure 1.6 Power line cable

liquefaction plants or cryogenic lines.

The most remarkable project has been developed by the city of Detroit in collaboration with the Italian factory Pirelli Cavi.. Three 150 m long HTS cables replaced 9 copper cables to carry 100MW of power reducing the energy losses to zero and delivering electricity to over 14.000 customers.

1.6 SUMMARY

In summary, the advantages of a superconducting circular accelerator are that the magnetic field can be greatly increased, with a reduction in the ring diameter, and a greatly reduced power consumption.

The main requirements for superconducting magnets in particle accelerators are high field uniformity and low cost. For the former, composite wires with very fine filaments are needed to reduce their magnetization and the associated field error. To reduce the cost, the critical current density should be pushed as high as possible.

CHAPTER

II

SUPERCONDUCTIVITY

2.1 INTRODUCTION

Superconductivity was first observed in 1911 by the Dutch scientist H. Kamerlingh Onnes, who was investigating the electrical resistance of metals at very low temperatures using liquid helium. It was known from previous works that the electrical resistivity of a metal fell when cooled below room temperature, but it was unknown what exactly happened close to 0 K. Onnes found out that at temperatures in the liquid helium range (4.1 to 1 K) the resistivity remained finite. Its value, determined by impurities and dislocations of the metal lattice, was called *residual* resistivity [7].

To avoid the effect of impurities Onnes used mercury that can be easily distilled because of its liquid state at room temperature. He discovered that after reaching the residual value, mercury's resistance dropped suddenly to zero in the vicinity of 4.25 K [8], as shown in Fig. 2.1. Similar transitions were found in lead at 7.2 K and in tin at 3.7 K, and the phenomenon was determined to be quite

general. The temperature at which the resistivity dropped to zero was called critical temperature (T_c).

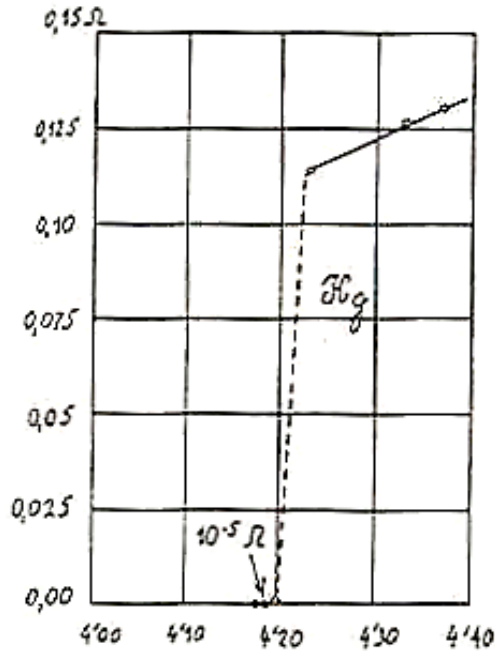


Figure 2.1 Onnes plot of mercury resistance versus temperature.

To check whether the resistance was really zero or just too small to be measured, Onnes cooled a ring of Tin below the critical temperature in a small applied magnetic field. The ring was then removed from the field to induce a current in it. There was no deducible decay of the current over several days. More recent measurements have extended this time to years. Such experiments allow for an upper limit of the superconductor resistivity [9] of about $10^{-24} \Omega \text{ cm}$, which is to all intents and purposes, zero (for

comparison the cryogenic resistivity of high purity copper is $10^{-9} \Omega \text{ cm}$).

Onnes was well aware from the very beginning that superconductivity might have important implications for electrical technology. In 1913 he constructed a lead coil and attempted to use it at 4.2 K (below T_c) to generate high magnetic fields. The result was disappointing, the coil quenched to the normal state at an internal field of a few fractions of T. Further experiments in an externally applied field [10] revealed that sharp quenching at a relatively low magnetic field, termed critical field (B_c) was typical of all known pure metal conductors. In summary, magnetic quenches occur by exposing the superconductor to an externally applied magnetic field or by winding the superconductor into a coil which, when excited, generates a field sufficient to quench the material.

For a superconducting wire, if an applied current is made sufficiently high, the field generated at the surface of the wire will rupture superconductivity. This current is called critical current (I_c).

The independent parameters T_c , B_c and I_c , are used to define the critical surface of the superconducting state, as shown in Figure 2.2.

In the following years, the technological developments in cryogenics allowed to better study superconductors. W. Meissner and R. Ochensfeld made a significant discovery in 1933 [11]. They proved that in a

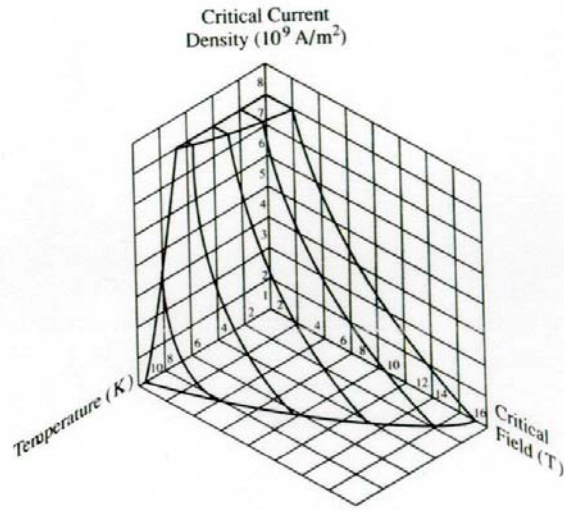


Figure 2.2 Critical surface for NbTi.

weak external magnetic field, a superconductor completely expels the magnetic flux from its interior, and that the zero induction is an intrinsic property of the superconducting state. This also implied that the transition to the superconducting state could be treated as a phase transition.

Magnetic field expulsion is known as Meissner-Ochsenfeld effect, and was modeled by F. London two years later by introducing two equations in addition to Maxwell's equations [12,13]. Although London's phenomenological two-fluid model correctly described absolute diamagnetism and zero resistance to a dc current, it did not attempt to resolve the microscopic mechanism of superconductivity at the level of electrons, that is, to answer the question "Why?". Moreover, it always predicted that the energy required to create the interface between adjacent normal and superconducting regions was negative (*i.e.* negative surface energy, σ_{ns}), against experimental evidence.

The above contradiction was reconciled by a theory proposed in 1950 by V. L. Ginzburg and L. D. Landau, which was phenomenological, but took into account also quantum effects [14, 15]. Its breakthrough was to assign a unique wave function to the entire ensemble of superconducting electrons, thus establishing their coherent behavior. This idea enabled the prediction of many beautiful macroscopic quantum effects in superconductivity.

In 1957, by applying the Ginzburg-Landau theory to superconducting alloys, A. Abrikosov developed a theory of the so-called type II superconductors [16]. It turned out that superconductors can be divided in types I and II according to the sign of their surface energy σ_{ns} , *i.e.* the energy required to create an interface between adjacent normal and superconducting regions, being respectively positive or negative. To this latter category belong most superconducting alloys and chemical compounds, as for example brittle intermetallics with the A15 crystal structure. When the field is increased beyond the Meissner phase, type II superconductors allow flux penetration inside the material in the form of quantized vortex lines, consenting superconductivity up to very high fields (called upper critical field, B_{c2}). The application of type I superconductors is of less interest, as mentioned below.

Still no theory could yet explain “What were those superconducting electrons?”. This question was finally answered in 1957 by the microscopic theory of superconductivity of J. Bardeen, L. Cooper and J. Schrieffer, known as BCS theory [17]. This theory is based on the assumption that the supercurrent is not carried by single electrons, but by pairs of electrons, of opposite momenta and spins, attracted by the interaction between electrons and phonons. These so-called *Cooper pairs* obey Bose-Einstein statistics and they all occupy the same ground state as a dissipation-free superfluid.

After the 1953 discovery of the superconducting A15 structure in V_3Si by Hardy and Hulm, and of Nb_3Sn in 1954 by Matthias et al., the first laboratory attempt to produce Nb_3Sn wire with the Powder-in-Tube process was made in 1961 by Kunzler et al..

In 1971, the Chevrel-phase compounds were discovered. Ternary molybdenum sulfide PbMo_6S_8 had a critical temperature of 15 K and an upper critical field of 60 T.

A new push in the field was given in 1986 by K. A. Muller and J. G. Bednorz's discovery of the first high T_c superconductor, a lanthanum, barium, copper and oxygen ceramic (LaBaCuO_4) that reached a critical temperature of about 40 K. For this discovery they won the Nobel Prize in 1988. The new enthusiasm that

was stirred into the scientific community led to Paul C. W. Chu and Maw-Kuen Wu's synthesis of $\text{YBa}_2\text{Cu}_3\text{O}_7$, with a T_c of 95 K [18]. For the first time, superconductivity was found to exist at temperatures above 77 K (boiling liquid nitrogen), opening the opportunity to cheaper cooling systems and, maybe, to commercial applications.

2.2 MEISSNER EFFECT AND LONDON EQUATIONS

The behavior of a superconductor in an external magnetic field was thoroughly investigated by Meissner and Ochsenfeld in the 1930s. They performed an experiment (scheme shown in Figure 2.3) in which a tin cylinder was first cooled down below T_c , and next placed in a magnetic field that was increased from zero up to a certain value B_0 . As expected from Faraday and Lenz law, a surface current was induced in the sample. At constant field, such current kept flowing in the material, and exactly cancelled the applied field in the interior reproducing a perfect diamagnetic state. The experiment was then replayed with an inversion of the two operations. The sample was first placed at room temperature in an external magnetic field B_0 , and next cooled down. Above T_c , the magnetic field penetrated its bulk, but below T_c , a surface current was generated and the

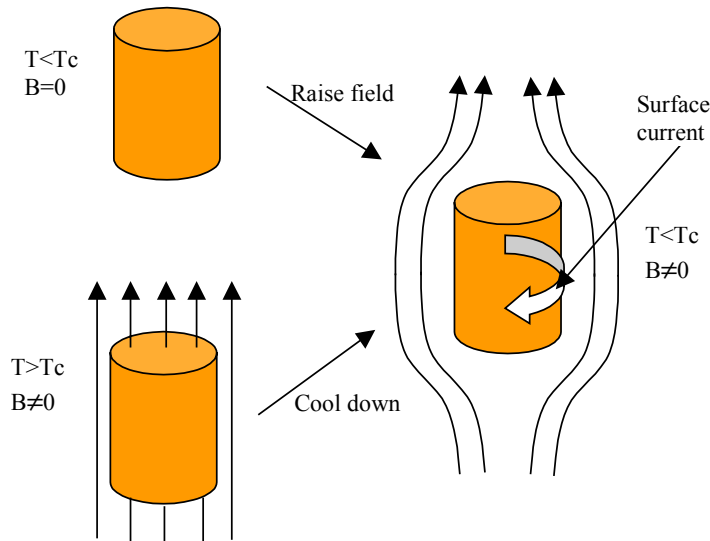


Figure 2.3 Meissner- Ochsenfeld effect.

magnetic field was expelled from the interior of the material. Lenz inductive law could explain only the former case, but not the latter, since the field had been kept constant. This showed that the superconductor was not simply an ideal conductor. The field inside the specimen was always zero independently of the specimen's history. To express this quantitatively, one can use 3rd Maxwell equation:

$$\nabla \times \vec{E} = -\frac{\partial}{\partial t} \vec{B}, \quad (2.1)$$

and integrate it at constant electric field, obtaining:

$$B = B(0). \quad (2.2)$$

Since for pure metals $B(0)$ is essentially zero, as Meissner and Ochsenfeld discovered in 1933, the relations below:

$$\vec{B} = \vec{B}_0 + \mu_0 \vec{M} = 0, \quad (2.3)$$

$$\vec{M} = \vec{B}_0 \chi \quad (2.4)$$

show that the magnetic susceptibility χ of a superconductor is strongly negative.

Fritz London gave a description of the phenomenon dividing all free electrons (of charge e and mass m) in the superconductor in two groups: *super-electrons* of density n_s , which generate supercurrents with zero resistivity, and normal electrons of density n_n [19]. The total density n is the sum of n_s and n_n . As the temperature increases from 0 to T_c , the density n_s decreases from n to 0. The equation of motion for superconducting electrons in an electric field and in a resistanceless mean is:

$$n_s m \dot{\vec{v}}_s = n_s e \vec{E}, \quad (2.5)$$

where v_s is the superfluid velocity and E is the electric field. Taking into account that the supercurrent density, \vec{J}_s , is:

$$\vec{J}_s = en_s \vec{v}_s, \quad (2.6)$$

one obtains the first London equation:

$$\dot{\vec{J}}_s = \frac{n_s e^2}{m} \vec{E}. \quad (2.7)$$

This equation describes the resistanceless property of a superconductor, since in stationary conditions there is no electric field generated inside.

Applying the curl operator to both members of equation 2.7, one can write 3rd Maxwell equation 2.1 as:

$$\frac{d}{dt} \left(\frac{m}{n_s e^2} \nabla \times \vec{J}_s + \vec{B} \right) = 0. \quad (2.8)$$

According to the classical theory of electromagnetism, the expression in the brackets is a constant. The new assumption made by London was that in the superconducting state, this constant is equal to zero, yielding:

$$\nabla \times \vec{J}_s = -\frac{n_s e^2}{m} \vec{B}. \quad (2.9)$$

This is second London equation, which describes perfect diamagnetism. Taking into account 4th Maxwell equation:

$$\nabla \times \vec{B} = \mu_0 \vec{J}_s, \quad (2.10)$$

equation 2.10 becomes:

$$\nabla^2 \vec{B} - \frac{1}{\lambda^2} \vec{B} = 0, \quad (2.11)$$

where:

$$\lambda = \sqrt{\frac{m}{\mu_0 n_s e^2}}. \quad (2.12)$$

It is worth mentioning that equation 2.11 can be obtained in a more sophisticated way, without any assumption, by solving a variational problem, namely by finding the function $B(x)$ corresponding to the minimum value of the superconductor free energy [20].

In the case of a superconducting semispace $x > 0$, whose surface lies on the plane $x = 0$, and with a magnetic field oriented along the y axis, equation 2.11 can be written as:

$$\frac{d^2 B_y}{dx^2} - \frac{1}{\lambda^2} B_y = 0, \quad (2.13)$$

whose solution is:

$$B_y(x) = B_0 \exp(-x / \lambda), \quad (2.14)$$

with the boundary conditions: $B(0) = B_0$, $B(\infty) = 0$.

According to this model, the magnetic field does not drop abruptly to zero at the boundary of a superconductor, but penetrates in the material with an exponential attenuation. The characteristic decay length λ is called London Penetration Depth. It follows from equation 2.6 that the supercurrent at the surface falls off over the same length. Typical values for λ are 20-100 nm. This behavior is typical of type I superconductors, and it strongly limits their application.

2.3 THERMODYNAMICS OF SUPERCONDUCTORS

It was clear by the late 1930's that the phenomenon of superconductivity had to be centered in the conduction electrons of a metal. The evidence for this was that the lattice properties were relatively unaffected at the superconducting

transition, whereas electronic parameters such as heat capacity, thermal conductivity, and electrical conductivity radically changed.

The transition from the perfectly diamagnetic superconducting phase to the non-magnetic normal phase is a *reversible* transition in the thermodynamic sense. Thermodynamic arguments can therefore be applied to a superconductor, using the temperature T and the magnetic field B_0 as thermodynamic variables.

2.3.1 Thermodynamic critical field of bulk material

The value of the critical magnetic field can be obtained by studying the effect that an applied magnetic field B_0 has on the free energy of a superconducting specimen. In any system, the stable state is that with the lowest free energy. The relevant quantity to be used in the comparison of the free energies of the superconducting and normal phases is Gibbs free energy density, g :

$$g = u - Ts + pv - B_0 M, \quad (2.15)$$

where u is the internal energy density, s the entropy density, v the specific volume, p the pressure, and M the magnetic dipole moment per unit volume.

Consider a long cylinder of superconductor. In the absence of a magnetic field, let the Gibbs free energy per unit volume of the superconducting state be $g_s(0)$, and that of the normal state be $g_n(0)$. When a magnetic field B_0 is applied parallel to the cylinder axis, at constant pressure and temperature, the superconductor free energy density changes by:

$$\Delta g_s(B_0) = - \int_0^{B_0} M(B') dB' = \frac{B_0^2}{2\mu_0}, \quad (2.16)$$

where $M = -B_0/\mu_0$, since magnetization exactly cancels the flux due to the applied field (equation 2.3). For a superconductor of volume V , Gibbs free energy G_s at a field B_0 can be written as:

$$G_s(B_0) = G_s(0) + \frac{B_0^2}{2\mu_0} V. \quad (2.17)$$

Instead, the free energy G_n of a metal in the normal state is constant with B_0 . The *critical field*, B_{cm} , is achieved when the free energy in the superconducting state, G_s , equals the free energy in the normal state, G_n :

$$\frac{B_{cm}^2}{2\mu_0}V = G_n - G_s(0), \quad (2.18)$$

Figure 2.4 illustrates the equilibrium point between these two states. $G_n - G_s$ can be interpreted as the Cooper pair condensation energy (see next section). B_{cm} is called *thermodynamic* critical field. For type I superconductors, it coincides with B_c , while in the type II case it lies between B_{c1} and B_{c2} .

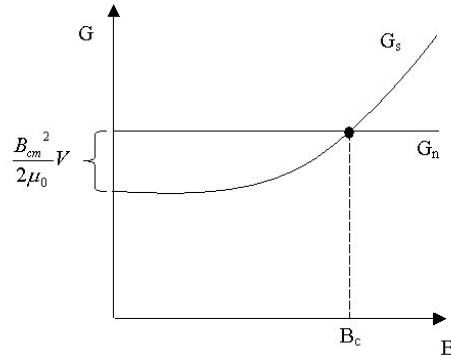


Figure 2.4 Free energy as a function of applied field.

2.3.2 Superconductivity as a phase transition

At constant pressure and constant applied magnetic field, the entropy per unit volume is given by:

$$s = - \left(\frac{\partial g}{\partial T} \right)_{p, B_0}, \quad (2.19)$$

From equations 2.17 and 2.18, one can write:

$$g_n - g_s(B_0) = \frac{1}{2\mu_0} (B_{cm}^2 - B_0^2), \quad (2.20)$$

Therefore:

$$s_n - s_s = -\frac{B_{cm}}{\mu_0} \frac{dB_{cm}}{dT}, \quad (2.21)$$

The right-hand side of this equation must be positive since dB_{cm}/dT is always negative. This shows that the entropy of the superconducting state is less than that of the normal state, *i.e.* the superconducting state has a higher degree of order than the normal state, in agreement with the BCS theory that predicts a highly correlated system of condensed electron pairs.

With zero applied magnetic field, the transition occurs at the critical temperature. At $T = T_c$, $s_n = s_s$ since B_{cm} falls to zero. This can be written as:

$$\left(\frac{\partial g}{\partial T} \right)_n = \left(\frac{\partial g}{\partial T} \right)_s. \quad (2.22)$$

A phase transition where not only g but also $\partial g/\partial T$ is continuous is known as a second-order phase transition. This implies two important characteristics. At the transition there is no latent heat, and there is a jump in the specific heat, c . The former follows from $dq = Tds$, the latter from the discontinuity of $\partial^2 g/\partial T^2$, whereas $c = -vT\partial^2 g/\partial T^2$.

However, in the presence of an applied magnetic field, the transition occurs at some lower temperature, where $B_{cm} > 0$. In such a case, the entropy of the normal state is greater than that of the superconducting state and latent heat is present. Heat must be supplied if the transition is to take place at constant temperature. In this case, g is continuous, but $\partial g/\partial T$ is not, and the superconducting-normal transition is of the first-order.

2.4 COOPER PAIRS

In 1957, Bardeen, Cooper and Schrieffer constructed a theory of superconductivity based on the interaction of electrons with the lattice vibration

or phonons of a solid. A key step in this work was the realization that below T_c a weak attractive interaction causes some of the conduction electrons to form Cooper pairs, a paired status with equal and opposite momentum at zero supercurrent. When a current is applied to the superconductor, all the pairs have the same momentum directed parallel to the electrical field. Due to this coherent motion the pairs do not collide with the lattice and there is no resistance.

When the first electron moves through the metal lattice, it attracts positive ions, but because of its inertia, the response of the lattice is not immediate. The shortest response time corresponds to the highest possible lattice frequency, which is called Debye frequency, ω_d . The maximum lattice deformation lags behind the electron by a distance, d :

$$d \approx v_f \frac{2\pi}{\omega_d} \approx 100 - 1000 \text{ nm}, \quad (2.23)$$

where v_f is the Fermi velocity which is on the order of 10^6 m/s. The second electron is attracted by the positive ion accumulation in the lattice deformation and the strongest effect is achieved when the two electrons follow adjacent

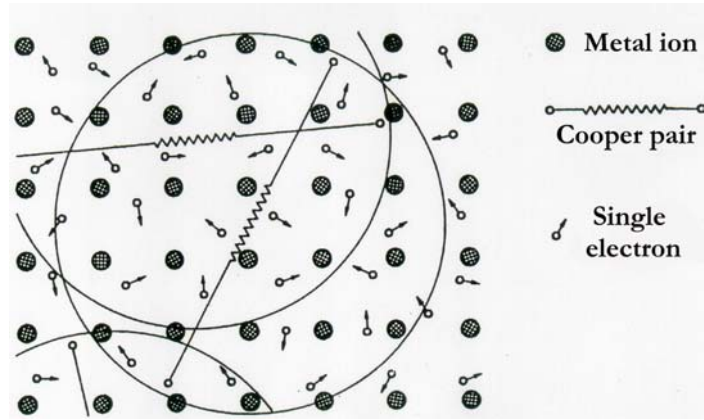


Figure 2.5 Cooper pairs.

tracks in the lattice and their distance is equal to d . This explains why a Cooper pair is a very extended object. As a consequence, Cooper pairs overlap each other, so that in the space occupied by a Cooper pair there are millions of others. This is very important for the BCS theory because the Cooper pairs must change their partners frequently in order to provide continuous binding. The binding energy of the Cooper pairs is very small, 10^{-4} - 10^{-3} eV, so that the pairs can only exist at low

temperatures where this energy is not overcome by thermal agitation. Because of their space extension, Cooper pairs differ considerably from other Bosons such as helium nuclei. They only exist in the BCS ground state and there is no excited state. An excitation is equivalent to breaking them up into single electrons. The BCS ground state is characterized by a macroscopic wave function and a ground state energy that is separated from the energy levels of the unpaired electrons by an energy gap of 2Δ . This gap is temperature dependent and at $T = 0$ it can be related to the critical temperature, T_c , through the following equation:

$$\Delta(0) = 1.76k_B T_c, \quad (2.24)$$

where k_B is the Boltzmann constant. Both Δ and T_c are proportional to the Debye frequency which in turn is inversely proportional to the square root of the atomic mass, M .

2.5 TYPE II SUPERCONDUCTORS

Type II superconductors, which include Nb, some alloys, compounds and high T_c superconductors, are characterized by two critical fields, called B_{c1} (1-10 mT) and B_{c2} (10-100 T). The discovery that the magnetic properties of alloy superconductors are radically different from those of pure metals seems to have first been made in Leiden. De Haas and Voogs [20] were studying the critical field for restoration of resistance of the lead-bismuth eutectic alloy ($T_c = 8.8$ K) at temperatures below 4.2 K. Whereas the B_c value of lead is about 0.055 T at 4.2 K, the corresponding value for Pb-Bi was found to be approximately 1.7 T. At 1.9 K the threshold value was even higher, approaching 2.7 T.

These high value of B_c stimulated a great deal of interest in the scientific world and during the 1930's several laboratories engaged in efforts to explain such effects. For most alloys it was found that there is a massive penetration of flux into the material at quite a low field, B_{c1} . However B does not become exactly

equal to B_0 above this critical field, since there is some residual diamagnetism and thus residual superconducting material forming a zero resistance path through the specimen. At a higher field, B_{c2} , even this residual material is quenched. Figure 2.6 shows the penetration of magnetic flux for magnetic fields exceeding B_{c1} , and the restoration of resistance for magnetic fields exceeding the upper critical field B_{c2} in alloy superconductors. The region between B_{c1} and B_{c2} was called mixed state.

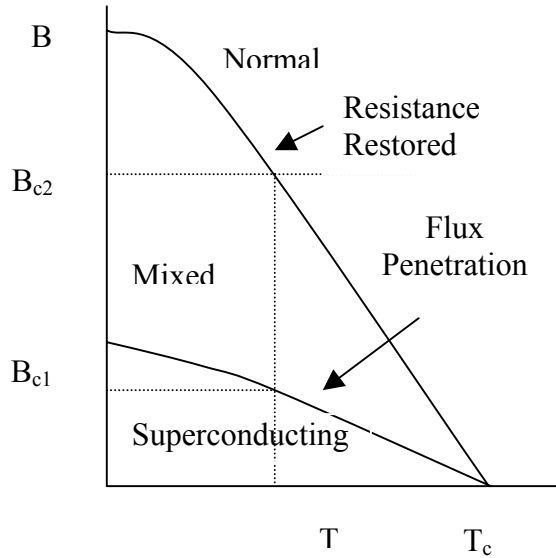


Figure 2.6 Temperature variations of upper critical field (resistance restoration) and lower critical field (flux penetration) for an alloy superconductor.

In summary, for external fields between zero and B_{c1} , the substance is in the Meissner phase, between B_{c1} and B_{c2} the material enters the *mixed phase*, where part of the magnetic flux penetrates the bulk in form of quantized flux tubes, and above B_{c2} the material is normal conducting.

The difference in magnetization behavior of

type I and type II superconductors is shown in Figures 2.7a) and b). In both cases, the area under the curve is the free energy difference between the normal and the superconducting state. Figure 2.7a shows a type I behavior. In the $(B_0, \mu_0 M)$ plane, the Meissner state is represented by a line with a slope equal to -1 that suddenly drops to zero at B_c , when the transition to the resistive state occurs. Figure 2.7b shows a type II behavior. The Meissner phase is shorter, but at B_{c1} the external field starts penetrating inside the bulk, and the magnetization drops smoothly to zero at B_{c2} .

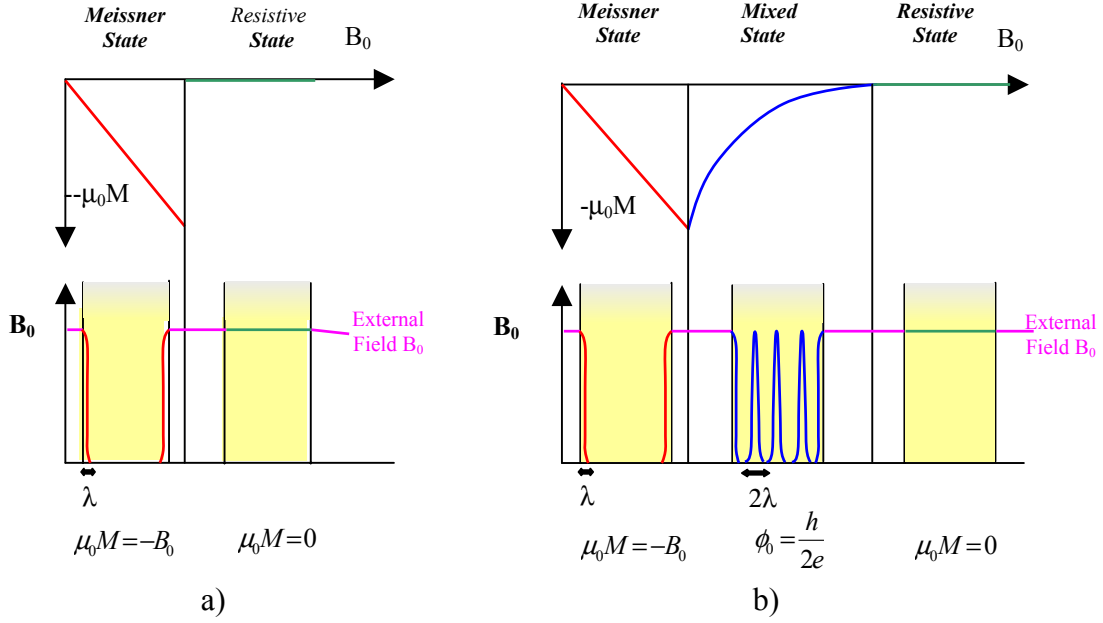


Figure 2.7 Magnetization behavior of type I (a) and type II (b) superconductors.

The first suggestion that a mixed state formed of alternating superconducting and normal zones would be energetically favored if the interface surface energy were negative was made in 1935. At a normal-superconducting boundary, the Cooper pair density does not jump abruptly from zero to its value in the bulk, but rises smoothly over a finite length ξ , called *coherence length*, as shown in Figure 2.8. In a conductor of unit area, exposed to a field B_{cm} parallel to its surface, the energy balance is as follow:

- The magnetic field penetrates a depth λ into the sample which corresponds to an energy gain since magnetic energy must not be driven out of this layer:

$$\Delta E_{mag} = \frac{B_{cm}^2}{2\mu_0} \lambda. \quad (2.25)$$

- On the other hand, because of the Cooper pair density rising over a length ξ , there is a loss in condensation energy:

$$\Delta E_{cond} = -\frac{B_{cm}^2}{2\mu_0}\xi. \quad (2.26)$$

There is a net energy gain if $\lambda > \xi$. The Ginzburg-Landau theory gives a more refined treatment of the phenomenon. The Ginzburg-Landau parameter is introduced as follows:

$$\chi = \lambda/\xi, \quad (2.27)$$

and the criterion for type I or II superconductivity is found to be:

Type I	$\chi < 1/\sqrt{2}$
Type II	$\chi > 1/\sqrt{2}$

The behavior of magnetic field and Cooper pair density at a normal-superconductor interface for type I and type II materials is shown in Figure 2.8.

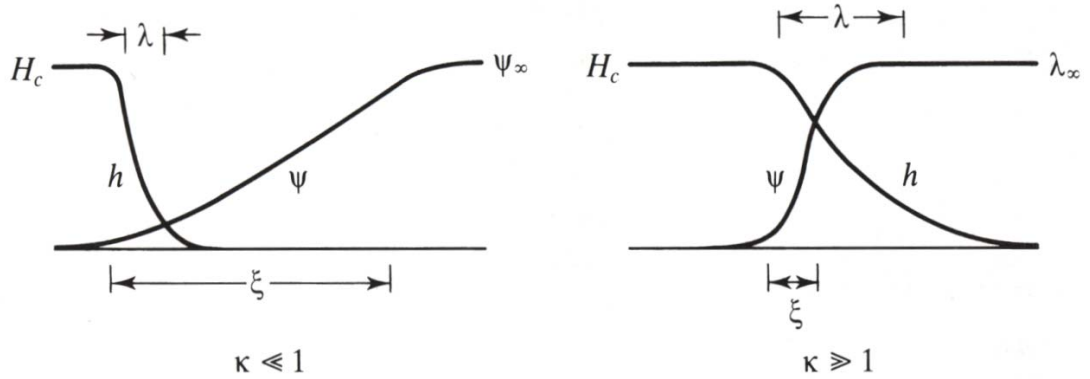


Figure 2.8 The decay of magnetic field and the rise of Cooper pair density at a normal-superconductor interface for type I (left) and type II (right) superconductors. In Figure, ψ represents the wavefunction of the superconducting electrons.

The coherence length is proportional to the mean free path of the conduction electrons in the metal. In alloys the mean free path is much shorter than in pure metals so they are always type II superconductors. In Table 2.1 are shown typical penetration depths and coherence lengths for type I and type II materials.

Material	Type	λ [10^{-9}m]	ξ [10^{-9}m]
Indium (In)	I	24	360
Lead (Pb)	I	32	510
Tin (Sn)	I	30	170
Niobium (Nb)	II	32	39
NbTi	II	300	5
Nb ₃ Sn	II	65	3

Table 2.1 Penetration Depths and coherence lengths of typical type I and II superconductors.

Further investigations on this subject were performed by Abrikosov, who developed a quantitative theory [21] such that the upper critical field is given by:

$$B_{c2} = \sqrt{2}\chi B_{cm} . \quad (2.28)$$

The lower critical field is given by:

$$B_{c1} = B_{cm} (\log \chi + 0.08) / \sqrt{2}\chi \quad (2.29)$$

for $\chi \gg 1$. χ was calculated by Gor'kov [22] in terms of normal metals parameters. It can be decomposed into a part arising from the pure metal electronic structure (clean limit), and a part arising from the scattering of electrons by impurities (dirty limit).

Some pure metals and compounds can be type II intrinsically, without the addition of large concentrations of impurities. In the case of pure metals the

crossover occurs for T_c around 8 K. Very high T_c materials such as the A15 compounds are strongly type II. Any type I superconductor can be converted to type II, in principle, if its normal state electrical resistivity can be increased enough. In addition, χ and B_{c2} for intrinsic type II materials, such as Nb_3Sn , can be increased by adding impurities. However, this process has a tendency to decrease T_c [23].

2.6 MAGNETIC FLUX QUANTIZATION

Both London and BCS theories predict that the magnetic flux trapped in the hole of a superconducting ring, produced by switching off an external magnetic field, cannot assume arbitrary values, but is quantized. The BCS elementary flux quantum is:

$$\Phi_0 = \frac{h}{2e}, \quad (2.30)$$

i.e. the Plank's constant divided by the charge of the supercurrent carriers. The London flux quantum is twice as big because the charge carriers in the London theory are single electrons. This phenomenon was experimentally seen in 1961 by Doll and Nabauer in Munchen, and by Deaver and Fairbank in Stanford, almost simultaneously.

Abrikosov predicted that a magnetic field penetrates a type II superconductor in form of flux tubes or *fluxoids*, each containing a single elementary quantum Φ_0 . The fluxoids arrange themselves in a triangular pattern to minimize the potential energy related to their mutual repulsion. The magnetic field lines are surrounded by a supercurrent vortex. The Cooper pair density drops to zero at the center of the vortex, so the core of a flux tube is normal conducting.

The area occupied by a flux tube is roughly $\pi\xi^2$. When an external field B_0 is applied, fluxoids keep moving into the specimen until their average field is equal to B_0 . The fluxoid spacing in the triangular lattice is in this case:

$$d = \sqrt{\frac{2\Phi_0}{\sqrt{3}B_0}}, \quad (2.31)$$

which amounts to 20 nm at 6 T. The upper critical field of a type II superconductor is reached when the current vortices of the fluxoids start touching each other, at which point superconductivity breaks down. In the Ginzburg-Landau theory the upper critical field is given by:

$$B_{c2} = \frac{\Phi_0}{2\pi\xi^2}. \quad (2.32)$$

The experimental observation of the fluxoid pattern was first performed by Essmann and Trauble. They used a lead-indium sample, cooled by liquid helium at 1.2 K. The liquid did not cover the upper surface of the sample. Iron was evaporated at some distance from the superconductor and in the 0.8 mbar helium atmosphere the iron atoms agglomerated to tiny crystals that were attracted by the magnetic field lines and stuck to the sample where the fluxoids emerged. After warming it up, a thin film was sprayed on the surface to allow the iron to be removed for observation in an electron microscope. The observation of the iron agglomerates showed a perfect triangular lattice as predicted.

2.7 HARD SUPERCONDUCTORS

2.7.1 Flux pinning

Despite their superconducting state, ideal type II superconductors show heat generation when carrying a transport current (in an applied magnetic field). This is due to *flux flow resistance*. The current exerts a Lorentz force on the flux lines and causes them to move perpendicularly to the current and to the field. To prevent such viscous motion, which dissipates heat, fluxoids have to be captured at *pinning centers* like defects or impurities in the crystal lattice. Imperfections

larger than the coherence length are needed to pin vortices. Pinning is necessary for high J_c 's and at present a large effort is spent in finding new ways to increase the pinning center density in Nb_3Sn .

For a superconducting slab in the yz plane with a transport current density along z and an external field along y , 4th Maxwell equation reads:

$$\frac{\partial B_y}{\partial x} = \mu_0 J_z, \quad (2.33)$$

which implies that a non-vanishing current density inside the conductor is necessarily coupled with a gradient in magnetic flux density. Such a gradient can only be maintained if flux pinning exists.

A type II superconductor with strong pinning is called a *hard superconductor*.

2.7.2 Magnetization of a hard superconductor

Hard superconductors exhibit a strong magnetic hysteresis, which is the origin of the persistent-current multipoles in superconducting accelerator magnets. While an ideal type II conductor without any flux pinning should show a completely reversible response to an external magnetic field, a hard superconductor is only reversible in the Meissner phase because then no magnetic field enters the bulk, so no flux pinning can happen. Above B_{c1} magnetic flux enters the sample and is captured at pinning centers. When the field is reduced again these flux lines remain bound and the specimen keeps a frozen-in magnetization even for vanishing external field. The field polarity has to be inverted to achieve $M = 0$, but the initial state can only be recovered by warming up the specimen to destroy

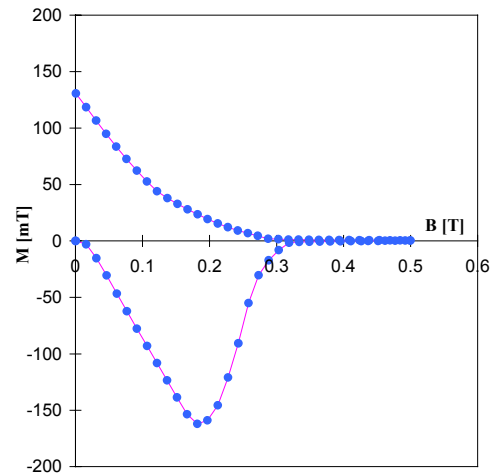


Figure 2.9 Nb hysteresis curve.

superconductivity and release all pinned flux quanta. A typical hysteresis curve is shown in Figure 2.9 for a Nb alloy.

2.7.3 Critical state model

Starting from the observation that the resistivity of a hard superconductor is almost a step function of current density, C. P. Bean (1962, 1964) proposed the so-called *critical state model*, according to which there are only two possible states for current flow in a hard superconductor [24]. The current density is either zero or equal to J_c . The Meissner phase is ignored. The critical state model has proved very successful in describing the magnetization of hard superconductors.

For an unmagnetized superconducting slab in the yz plane exposed to a magnetic field along y , 4th Maxwell equation can be written as follows:

$$\frac{\partial B_y}{\partial x} = \mu_0 J_c, \quad (2.34)$$

Up to some small value of B_0 , a bipolar current of density $\pm J_c$ is induced in the slab which penetrates to the depth necessary for the shielding field to cancel the applied field in the central region. In the region of current flow the magnetic field is linear, as shown in Figure 2.10a).

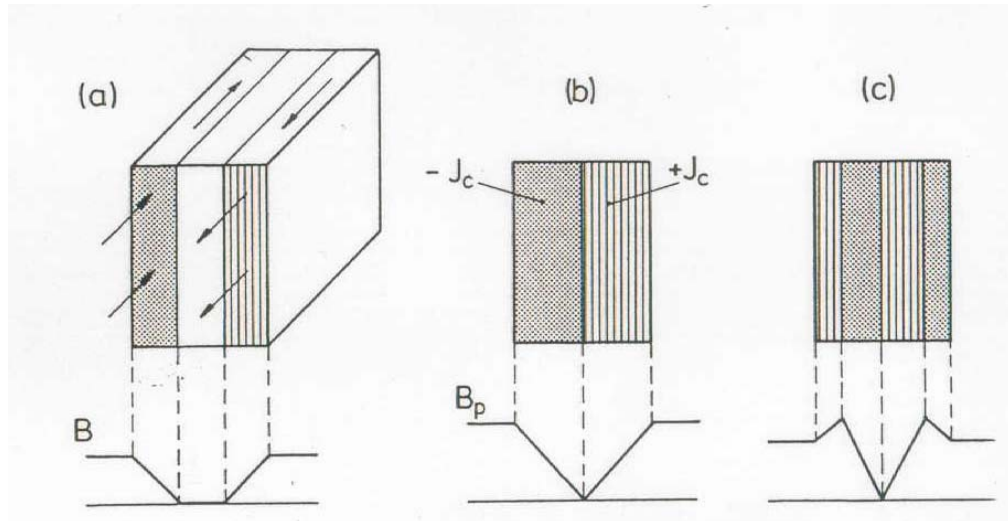


Figure 2.10 Current and field distribution in a slab of a hard superconductor according to the critical state model

As long as the external field is kept constant the current pattern will persist. When the external field is increased, both current and field penetrate deeper into the slab until the center is reached (Figure 2.10b). The associated field is called the *penetrating field* B_p . Raising B_0 beyond B_p leads to a non-vanishing field at the center, but eventually the current density will drop because it depends on magnetic field.

When B_0 is lowered again, a new bipolar current of opposite polarity is induced and the current-field pattern inside the slab assumes the complicated shape sketched in Figure 2.10c). It is straightforward to derive a hysteresis curve from this model (see Figure 2.11).

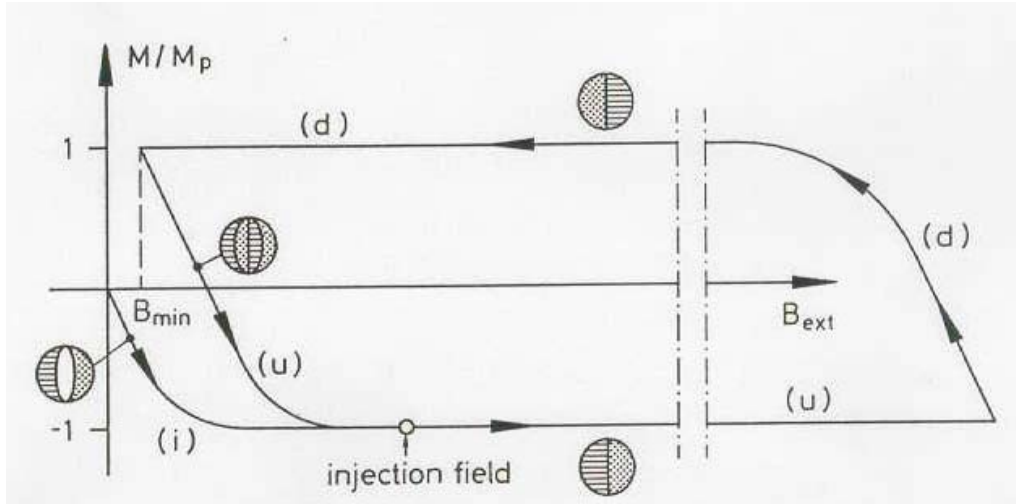


Figure 2.11 The normalized magnetization M/M_p as a function of the external field. (i): initial curve, (u): up-ramp branch, (d):down ramp-branch.

CHAPTER

III

SUPERCONDUCTING MATERIALS

3.1 INTRODUCTION

An important issue for the development of new superconducting materials is to reach higher operating temperatures in order to reduce the cost of the cooling system. However, at present only low temperature superconductors (LTS), operating at boiling helium temperature, are used to design and produce magnets, because the main demand on high current densities limits the choice of the material to be used. The new high temperature superconductors (HTS) still do not reach very high current densities and are difficult to produce in the form of long thin wires [25].

The same request excludes using type I superconductors, where in the Meissner state current can flow only in a small part of the strand cross section (delimited by the λ length) near the boundaries. Furthermore, these materials show a very low critical field, which limits applications. Hard type II superconductors are the only materials usable to manufacture magnets.

Over the last twenty years, niobium titanium alloys have undergone extensive development. Niobium titanium alloys are ductile and can be co-processed with copper into a wide range of composite conductors. NbTi is currently the most commonly used material in magnet industry, but its properties are adequate only up to fields of 8-9 T [26]. MRI solenoids and superconducting accelerators, starting from the Tevatron, HERA, and more recently LHC have relied on NbTi. In addition, the Superconducting Super Collider (SSC), a U.S. project that was first approved and later cancelled, planned to use NbTi. Significant advances in performance as well as conductor cost reduction resulted from the SSC R&D.

For optimum performance, the critical parameters J_c , B_c , and T_c , should be as large as possible. In general, it turns out that critical field and temperature are determined by the chemistry of the material, like the composition, whereas the critical current density is determined by the microstructure [27]. Therefore, the J_c of niobium titanium has increased as the processing techniques have been improved, whereas the critical field and temperature have remained more or less constant.

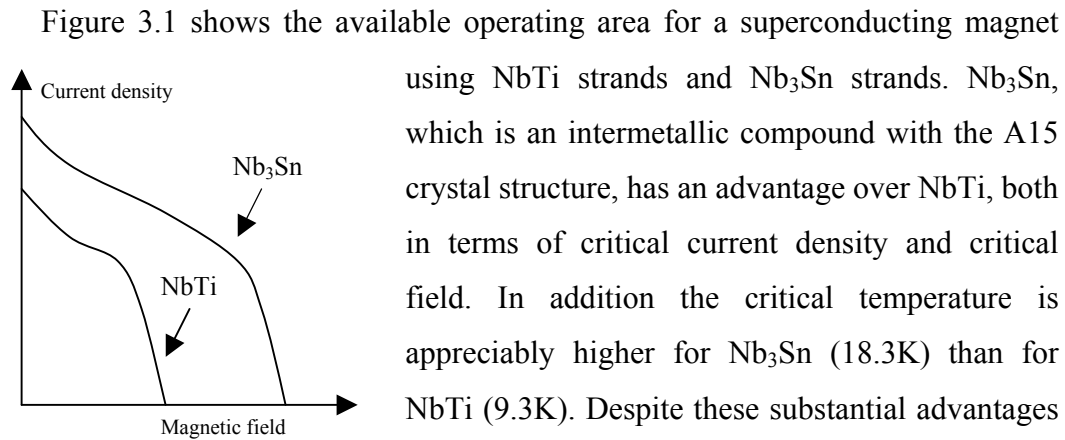


Figure 3.1 Critical current densities of NbTi and Nb₃Sn at a constant temperature (4.2 K).

using NbTi strands and Nb₃Sn strands. Nb₃Sn, which is an intermetallic compound with the A15 crystal structure, has an advantage over NbTi, both in terms of critical current density and critical field. In addition the critical temperature is appreciably higher for Nb₃Sn (18.3K) than for NbTi (9.3K). Despite these substantial advantages Nb₃Sn has been used so far only on a fairly modest scale in comparison with NbTi. The reason for this lies entirely in the mechanical properties of Nb₃Sn.

Unlike NbTi, which is a ductile alloy, Nb₃Sn is a brittle intermetallic compound which critical current is extremely sensitive to tensile strains.

However, only A15 (Nb₃Sn and Nb₃Al) and HTS (Bi-2223, Bi-2212, and YBCO) materials could in principle be used above 10 T. As mentioned, HTS's

are not competitive yet. On short-term magnet production, Nb_3Sn appears to be the right choice, while Nb_3Al is the most promising on the medium term, showing less strain sensitivity.

The need of heat treating the Nb/Sn composite to form brittle and strain sensitive Nb_3Sn imposes a completely different technology in magnet fabrication with respect to NbTi magnets. The magnet has to be first wound, and then reacted at high temperatures. This opens up a whole range of research areas, like the optimization of the heat treatment cycle to provide the best superconducting and mechanical properties, the investigation of an insulation material that would withstand both high temperatures and radiation exposures, the assessment of any size variation during the cycle [28], and more.

3.2 CONDUCTORS FOR USE IN MAGNETS

3.2.1 Degradation and training

To characterize the performance of a superconducting magnet, a diagram like that showed in Figure 3.2 is typically used. The straight line, called load line, represents the peak field experienced by a magnet winding as a function of the current flow. The upper curve is the critical current of the superconductor as a

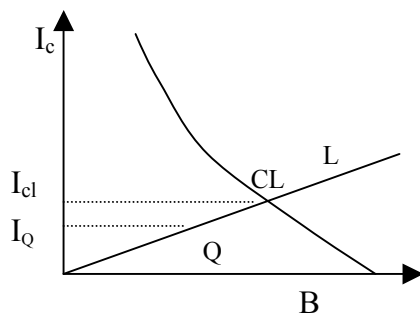


Figure 3.2 Critical current curve of a superconductor together with the magnet load line. The intersection CL is the maximum expected current and field in the magnet.

function of field. The point at which the peak field of the magnet is expected to reach its critical state is given by the intersection CL. However, it happens that a magnet quenches at much lower currents, typically in the region of Q.

Quenching is the term used to describe the transition of any part of the magnet from superconducting to normal state.

Because of the large normal state resistivity of a superconductor and the high current density, the transition causes intense local heating, which spreads to

neighboring part of the winding. The normal zone grows rapidly until all the stored inductive energy $\frac{1}{2}LI^2$ has been dissipated as resistive heating. Quenching at lower currents than expected is known as *degradation*, which is related to thermal disturbances of any kind and cooling conditions. An energy deposition of only 1 mJ/g is needed to heat the conductor beyond critical temperature due to the negligible heat capacity of metals at cryogenic temperatures (liquid He is the only substance with some heat capacity in the 2-4 K range). Therefore at high currents a motion of a few μm will produce enough frictional energy to quench a magnet. If the windings can move under the Lorentz forces, degradation may be accompanied by *training*, which is the progressive increase in quench current after repeated quenching. A good stability is achieved by preventing conductor motion (by impregnating the coil for example with epoxy resin), improving cooling, and, last but not least, optimizing the conductor design.

3.2.2 Copper stabilization

As mentioned in section 3.2.1, superconducting windings are exposed to a variety of disturbances that may heat the coil locally beyond the critical temperature. The stability of a coil is a measure of its ability to recover superconductivity after such disturbances. There are two limiting cases in cooling: the conductor is surrounded by liquid He with direct transfer of heat to the coolant, or the windings are embedded in an insulating medium and cooling occurs only via heat conduction along the wires. In both cases, in parallel with any practical superconductor, a good conductor like high purity copper is needed as an electrical bypass and heat sink.

In the case of poor contact with the He coolant, the maximum length l that a zone turned normal can have not to propagate a quench is [25]:

$$l = \sqrt{2K(T_c - T_0)/J^2\rho}, \quad (3.1)$$

where J is the current density, ρ the normal resistivity, K the thermal conductivity, and T_c and T_0 the critical and operating temperatures.

Whereas for pure NbTi, l is about $1\text{ }\mu\text{m}$, if the superconductor is brought in intimate contact with an excellent conductor like high purity copper l can be increased by a factor of thousand. In this case the thermal conductivity and resistivity in the longitudinal direction is determined almost entirely by copper, which at 6 T and 4.2 K, has $K = 350\text{ W m}^{-1}\text{ K}^{-1}$ and $\rho = 3 \cdot 10^{-10}\text{ }\Omega\text{m}$.

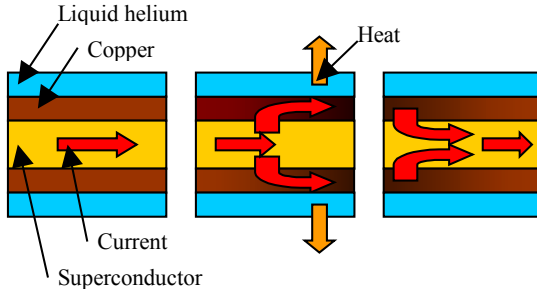


Figure 3.3 Cryogenic stabilization.

In the limiting case of a conductor immersed in a liquid He bath of temperature T_0 , heat transfer to the He plays the dominant role and the so-called *cryogenic stabilization* can be applied. Figure 3.3, which shows a scheme of a superconductor joined along its entire length to copper,

illustrates the general principle. If the superconductor is temporarily heated beyond T_c , the current is taken over by the copper for a short moment. If the copper is sufficiently well cooled for the ohmic heating to be dissipated without excessive temperature rise, the superconductor eventually cools down and recovers superconductivity. Current transfers back to it from the copper and the ohmic heating ceases. To fulfill these tasks, the copper matrix must be in as good electrical and thermal contact with the superconductor and the cooling bath as possible.

3.2.3 Flux jumping

One of the first causes of instability to be studied systematically is a phenomenon known as *flux jumping*, a magnetic instability that can break superconductivity down by releasing the magnetic flux bundles from their pinning centers. It can be explained by considering a thermally isolated superconducting slab of width $2a$ exposed to a vertical external field B_0 larger than the penetrating field B_p . As seen in Section 2.6, a bipolar current of density $\pm J_c(B_0, T_0)$ is induced in the slab, whereas the magnetic field exhibits a linear behavior, with a non-vanishing value at the center. If an amount of heat δQ per unit volume is

introduced in the sample, the temperature will rise from T_0 to $T_0 + \delta T$ and J_c will drop by δJ_c . Magnetic flux will then increase, generating heat, which in turn raises the temperature, and so on. If this feedback is strong enough, the smallest fluctuation of the parameters in the loop will be sufficient to trigger an avalanche change in flux, which may raise the temperature above critical.

Neglecting the cooling by the surrounding helium, the maximum thickness of the slab to prevent flux jumps can be calculated as [28]:

$$2a \leq 2\sqrt{\frac{3\gamma C(T_c - T_0)}{\mu_0 J_c^2}}. \quad (3.2)$$

where γ is the material density, C is the specific heat, and T_c is the critical temperature at B_0 field. Equation 3.2 is called *adiabatic* flux jump stability criterion.

By using equation 3.2, the maximum slab thickness to avoid flux jumping at 1 T and 4.2 K was found to be about 80 μm for NbTi and about 130 μm for Nb₃Sn [32].

3.2.4 Filamentary composites

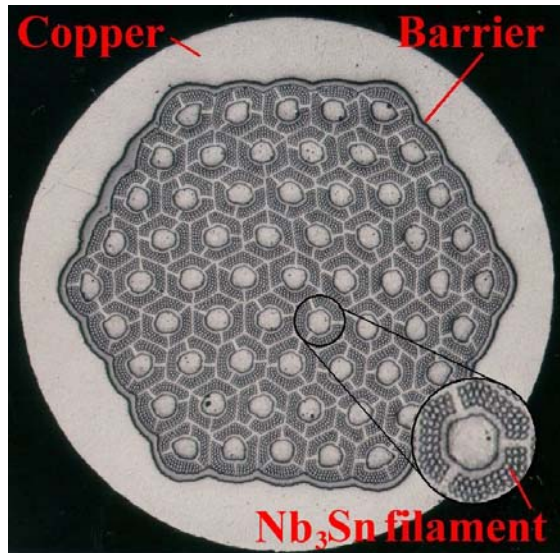


Figure 3.4 Nb₃Sn multifilamentary strand.

The conductor used in magnet industry is not pure superconducting material. Thin filaments of NbTi or Nb₃Sn are embedded in a copper matrix to form a multifilamentary strand. The need of implementing copper in the strand design was described in section 3.2.2. The filaments have to be limited in size for two reasons, one of which is flux jumping, as

explained in section 3.2.3.

The second reason to require small filaments is to limit persistent magnetization currents in the superconductor [30], which are the sources of severe field distortions at low excitation of an accelerator magnet. These bipolar currents generate all the multipoles allowed by the coil symmetry. A distinct hysteresis behavior is also observed. Actually the restriction on filament diameter is more constraining for magnetization than for flux jumping. For NbTi, filament diameters of 5-6 μm are needed for relative deviations from ideal dipoles or quadrupoles on the order of 10^{-4} [30].

The filaments in a strand are also twisted with a pitch of 15-25 mm (more tightly than needed for stability against flux jumping) to suppress inter filament eddy currents induced during a field sweep across the matrix. Figure 3.4 shows a typical cross section for an Intermagnetics General Corp. (IGC) intermediate tin Nb₃Sn strand with 61 split-subelements before thermal reaction. The non-copper region containing the split-subelements is separated from the outer copper matrix by means of a tantalum barrier. Each subelement contains 106 Nb filaments.

3.3 NIOBIUM TITANIUM

Niobium and titanium are mutually soluble to form ductile alloys over a wide range of compositions. The critical properties vary with composition. Since optimum critical field and highest critical temperature do not occur at the same composition, commercial alloys are usually formulated for optimum critical field, in the range of Nb 46.5 to 50 wt% Ti. Otherwise a compromise must be found depending on the technological application of the strand. A ternary element, most commonly tantalum, may also be added to produce a modest increase in B_{c2} of 0.3 T at 4.2 K and 1.3 T at 1.8 K.

Originally it was thought that the principal source of flux pinning in the material came from the dislocation cell structure in the wire. It has now become clear that most of the pinning is provided by finely divided deposits of Ti α -

phase. This is a hexagonal close packed titanium rich phase, which is precipitated on the dislocation cell boundaries as a result of the heat treatments applied during the manufacturing process. The α phase remains normally resistive at low temperature and has been shown to be a significant source of flux pinning sites.

Artificial pinning center (APC) techniques have been attempted in order to increase the field operating range and critical current. These techniques are based on the fine dispersion of second phase particles by mechanical processing. So far they have only allowed achieving higher critical currents at low fields.

The request for higher field magnets has led to NbTi being used at temperatures lower than 4.2 K. This is the case of the Large Hadron Collider (LHC) at CERN. The magnets for this accelerator will work in superfluid helium (1.9K), where B_{c2} is increased from its 4.2 K value of 11 T to 14 T. The use of superfluid helium brings many other benefits in terms of better cooling and stability.

The manufacturing technology has been developed by different firms. Currently, the production of high J_c wires with filaments below 10 μm embedded in a high purity OFHC (Oxygen Free High Conductivity) copper matrix is normal practice. A scheme is shown in Figure 3.5. The first step of the process is to build a billet of high homogeneity NbTi alloy by arc vacuum melting. The NbTi is then fitted inside a copper extrusion can with a thin diffusion barrier of pure Nb interposed between the NbTi and the copper. The purpose of this barrier is to prevent the formation of CuTi_2 intermetallics during intermediate heat treatments, since they are hard and brittle, and break the filaments at the last stages of drawing. The billet is evacuated, electron-beam welded, and extruded. After cold drawing to size, the rod is drawn through a hexagonal die and then cut into many lengths. These lengths are stacked into another copper can, which is again sealed, extruded and drawn down to final size. For accelerator magnets, which may have up to 10^4 filaments, a double stack process is often used in which the rods are again drawn into hexagonal sections and stacked in another can. Multiple heat treatments are applied throughout the process in a defined sequence of alternating cold work and heat treatment, which has been found to produce the best

configuration of α Ti precipitates and hence the best flux pinning. After reaching final size, the wire is twisted.

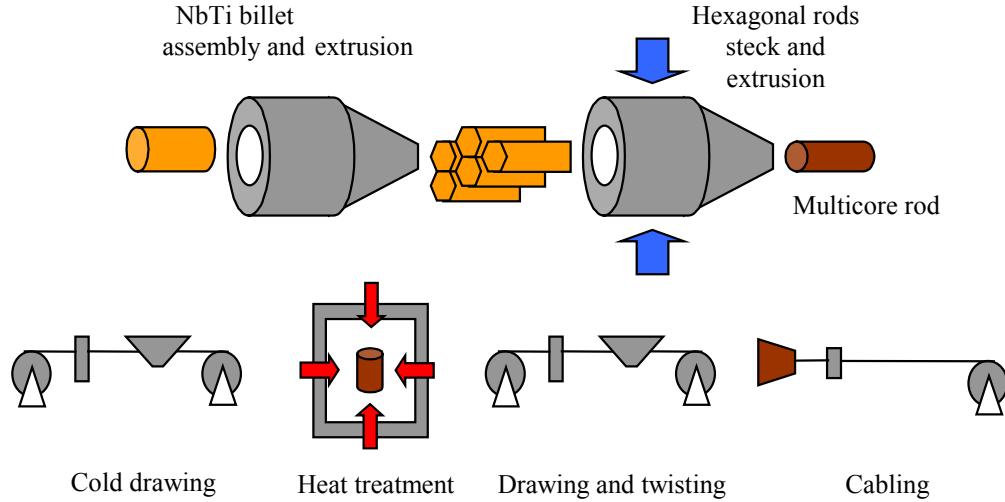


Figure 3.5 Production process of NbTi strands and cables.

Typical properties of NbTi strand produced for LHC dipoles are listed in Table 3.1.

	IGC NbTi
Wire diameter [mm]	1.29
Filament diameter [μm]	5
Cu to non-Cu ratio	1.8
I_c at 8 T and 4.2K [A/mm^2]	1114

Table 3.1 NbTi properties for LHC.

3.4 NIOBIUM TIN

Nb_3Sn is an intermetallic compound having a well-defined stoichiometry and the A15 crystal structure [27]. It shows higher critical temperature and field than NbTi, but is highly brittle, as previously mentioned, and its critical current is extremely strain sensitive. Originally, Nb_3Sn was produced in the form of tape by

heating Nb tapes in a liquid Tin bath at temperatures above 930°C. However, as will be shown in section 3.5, tapes are not a useful shape for magnet design, and new processing techniques had to be developed. The basic elements Nb, Sn, and Cu are manufactured in the form of a round composite strand. At this stage, the strand is still ductile and can be used to produce cables.

The A15 compound is formed at the interface of Nb and the Cu-Sn matrix by heat treating such composites at temperatures of about 700°C. The Cu matrix is necessary to shorten the heat treatment time, since Cu works as a catalytic agent for the preferential growth of Nb₃Sn phase at the expense of other non superconducting Nb-Sn phases. Prior to heat treating the strand at high temperature to form the Nb₃Sn compound, heat treatments at lower temperature are necessary to homogenize the Cu-Sn matrix. Further details about the heat treatment process are presented in Chapters 4, 8 and 9.

The dominant source of flux pinning in Nb₃Sn appears to be the grain boundaries [31]. In order to obtain high critical current densities it is therefore necessary to produce a fine grained structure. This is in conflict with the long time necessary to obtain a consistent volume of superconductor. The optimum process is obtained by balancing these two issues and taking into account the material specific application. Further details on this subject will be given in Chapter 9.

The critical current density, J_c , needs to be carefully defined. In NbTi one normally quotes the critical current density in the superconductor, J_{cNbTi} , and the critical current density on the whole strand cross section, J_{cav} . These two current densities are related to each other as follows:

$$J_{cav} = \lambda J_{cNbTi}, \quad (3.3)$$

where λ is the copper to superconductor ratio. For Nb₃Sn the distinction is complicated by the presence of the bronze between the filaments, generated from the diffusion of tin into the copper. Usually the critical current density is calculated in the non-copper part of the strand, which is comprehensive of both superconductor and bronze, while the overall average value, J_{cav} , is still calculated on the whole strand cross section.

Different manufacturing processes have been tested and developed in the last years by different companies. The most important ones are:

- Bronze process;
- Internal tin process (IT);
- Modified jelly roll process (MJR);
- Powder in tube process (PIT).

Heat treatments are determined and suggested by the manufacturing companies for each type of strand. In principle, this is done by trying various heat treatment schedules, testing the resulting properties of the strand, and choosing the thermal cycle that achieves the best strand performance.

3.4.1 The bronze process

The bronze process, although almost twenty years old, is still that used most frequently for large production of Nb_3Sn where reproducibility and reliability are essential and cost of little significance [23].

The bronze process is very similar to the fabrication of NbTi wires. A rod of pure ductile Nb or Nb containing a small amount of Ta or Ti is assembled in a bronze matrix, extruded, and drawn to the final size. The tin content in the bronze matrix being limited to less than 13.5wt% (limit for a ductile bronze alloy), a large bronze matrix is required to provide sufficient tin to the niobium rods. The initial billet is made of hundreds of Nb rods and it is drawn into a hexagonal shaped element of intermediate size. The hexagonal rods are cut and reassembled in a second billet, which is extruded, annealed and drawn to the final wire size. Nb_3Sn wires are stabilized against flux jumping using OFHC copper. The copper has to be protected from the diffusion of the bronze-tin by a tantalum or niobium barrier. The niobium barrier is cheaper, but at low fields it is superconducting [23]. This can cause field distortions, which can become intolerable in applications like particle accelerator magnets. In these cases a Tantalum barrier is preferred. The stabilizing copper can be incorporated internally with up to 27% of the wire cross section or externally with a copper part of 30-60%.

The bronze process requires frequent annealing steps because bronze work hardens rapidly. If precautions are not taken, these multiple anneals result in prereaction between the Sn in the bronze and the Nb, with formation of Nb_3Sn during fabrication [32].

3.4.2 The internal tin process

The Internal Tin (IT) process was introduced to overcome the main limit of the bronze method, which is a limited tin content of 13.5wt% in the matrix. A higher concentration of tin produces higher critical current densities in the Nb_3Sn layer [23].

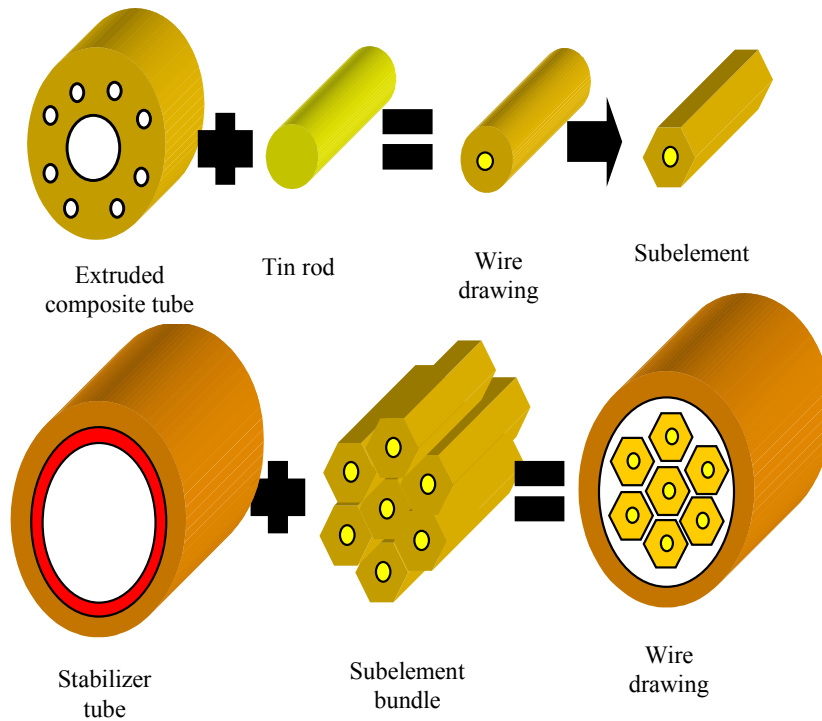


Figure 3.6 Internal Tin Process.

The idea was to distribute local tin sources surrounded by Nb rods and located in a copper tube. The composite Cu tube containing several Nb rods around a central hole is first hot extruded, then filled with Sn and drawn into hexagonal subelements, which are shortened and reassembled into a new billet characterized by a stabilizing copper outer ring protected by a tantalum barrier. The billet is

then drawn to the final wire size without intermediate annealing. Since this process does not involve intermediate anneals during wire fabrication, the billets are free from prereaction problems.

Factors like the amount of Nb, the amount of Sn, the filament size and the subelement number characterize the conductor properties [33].

This method suffers from “bridging” problems [32]. Since the Nb filaments around the Sn rod within a subelement are close together, they join or “bridge”

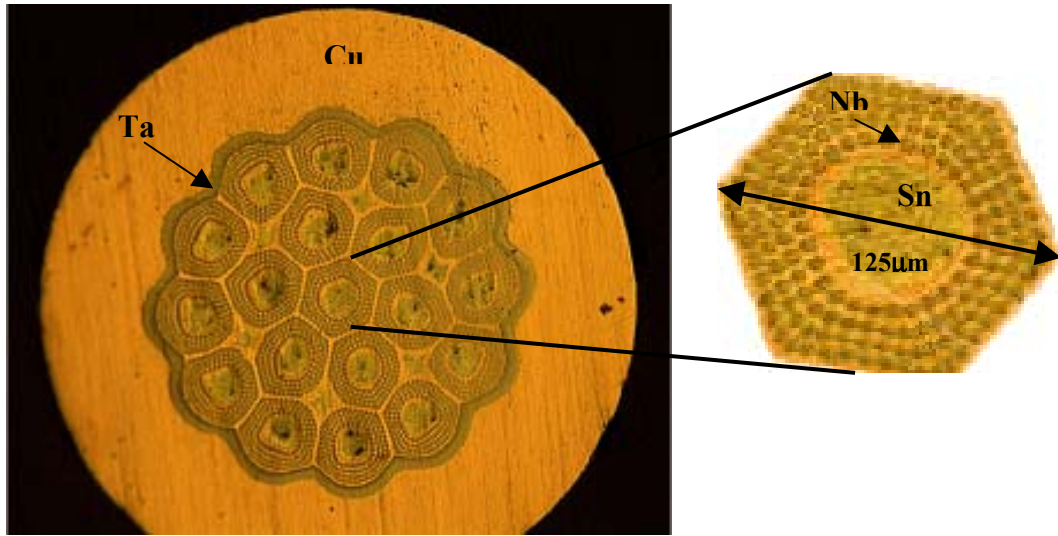


Figure 3.7 Internal Tin (IT) by Intermagnetic General Corporation (IGC).

during reaction when their volume increases after the conversion of Nb into the more voluminous Nb_3Sn . This leads to a so-called *effective filament diameter* much larger than the filament itself with flux jumps and large magnetization. This problem could be solved by spacing the filaments more widely apart. However, this would lower the overall J_c , thus invalidating one of the chief advantages of the process.

Figure 3.7 shows an unreacted IT wire of 1 mm diameter by Intermagnetics General Corporation (IGC). This IT strand of ITER design [34] was one of those used to perform the diffusion studies presented in this work. Its properties are presented in Table 3.2. Typical heat treatments suggested by IGC for IT designs are detailed in Table 3.3.

Property	IGC ITER
Wire diameter [mm]	1.000 ± 0.001
Filament diameter [μm]	5
Number of subelements	19
Sn pool diameter [μm]	50
Cu stabilizer [%]	$58.7 \pm .03$
Sn at.% in the non-Cu	10.1
Nb at.% in the non-Cu	20.4
I_c at 12 T and 4.2K [A]	> 200
J_c at 12 T and 4.2K [A/mm^2]	> 700
RRR ($\rho_{\text{Cu}@300\text{K}}/\rho_{\text{Cu}@4.2\text{K}}$)	> 300

Table 3.2 IGC ITER strand parameters.

Heat Treatment		Step 1	Step 2	Step 3	Step 4
IGC A	Ramp rate [$^{\circ}\text{C}/\text{h}$]	6	6	25	25
	Temperature [$^{\circ}\text{C}$]	185	460	570	650
	Duration [h]	48	100	200	175
IGC B	Ramp rate [$^{\circ}\text{C}/\text{h}$]	25	25	25	
	Temperature [$^{\circ}\text{C}$]	185	575	680	
	Duration [h]	100	200	250	
IGC C	Ramp rate [$^{\circ}\text{C}/\text{h}$]	25	25	25	
	Temperature [$^{\circ}\text{C}$]	575	650	680	
	Duration [h]	200	175	75	

Table 3.3 IGC typical heat treatments for IT strand.

3.4.1 The modified jelly roll

The Modified Jelly Roll (MJR) is a variant of the internal tin method pursued by Teledyne Wah Chang company in the US. It consists of two parallel sheets of niobium and copper rolled around a solid tin rod. In this way the niobium part in the non-copper area is increased to 35%. The roll is inserted in a copper tube to

form a billet. During drawing the niobium cross section is reduced by ~ 750 times and shaped as a hexagonal rod. A second billet is then assembled using the hexagonal rods, and drawn to the final wire size. No annealing is required during the process. Protecting barriers have to be inserted between the tin core and the niobium sheet, between the niobium and copper sheets, and before the external stabilizing copper. For this purpose tantalum, vanadium, and niobium are used. Figure 3.8 illustrates the main steps of this process.

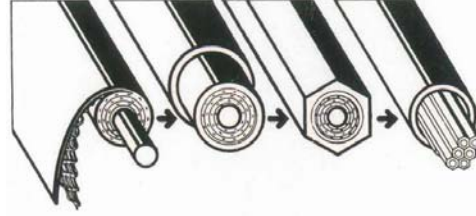


Figure 3.8 Modified jelly roll.

The same factors as in the IT method characterize the conductor properties [32]. Like the IT process, this technology also suffers from filament “bridging” [33].

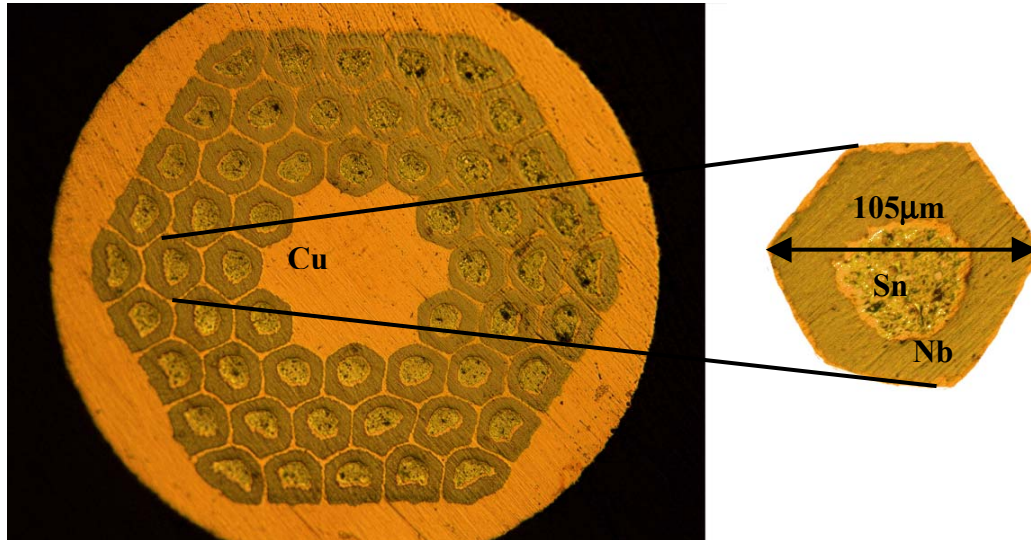


Figure 3.9 Modified Jelly Roll (MJR) by Oxford Superconducting Technology.

Figure 3.9 shows an unreacted MJR wire of 1 mm diameter by Oxford Superconducting Technology (OST). This MJR strand was one of those used to perform the diffusion studies presented in this work. Its properties are presented in Table 3.4. Typical heat treatments suggested by OST for MJR designs are detailed in Table 3.5.

Property	OST MJR
Wire diameter [mm]	1.000 ± 0.001
Filament diameter [μm]	< 110
Number of subelements	54
Sn pool diameter [μm]	45
Cu stabilizer [%]	48 ± 0.03
Sn at.% in the non-Cu	16
Nb at.% in the non-Cu	50
I_c at 12 T and 4.2K [A]	> 800
J_c at 12 T and 4.2K [A/mm^2]	> 1900
RRR ($\rho_{\text{Cu}@300\text{K}}/\rho_{\text{Cu}@4.2\text{K}}$)	< 20

Table 3.4 OST MJR strand parameters.

Heat Treatment		Step 1	Step 2	Step 3
OST A	Ramp rate [$^{\circ}\text{C}/\text{h}$]	25	50	75
	Temperature [$^{\circ}\text{C}$]	210	340	650
	Duration [h]	100	48	180
OST B	Ramp rate [$^{\circ}\text{C}/\text{h}$]	25	50	75
	Temperature [$^{\circ}\text{C}$]	210	340	675
	Duration [h]	100	48	180

Table 3.5 OST typical heat treatments for MJR strand.

3.4.4 The powder in tube process

The Powder in Tube (PIT) process was first developed by the Netherlands Research Foundation and is presently adopted by the Shape Metal Innovation Company (SMI) [35]. The basic idea is to fill hollow Nb tubes with fine granulated Nb_2Sn powder and then place them into a Cu matrix. Compared to other methods, a large portion of the non-active bronze content can be replaced by

superconductor elements or stabilizing Cu. The non-reacted part of the outer Nb

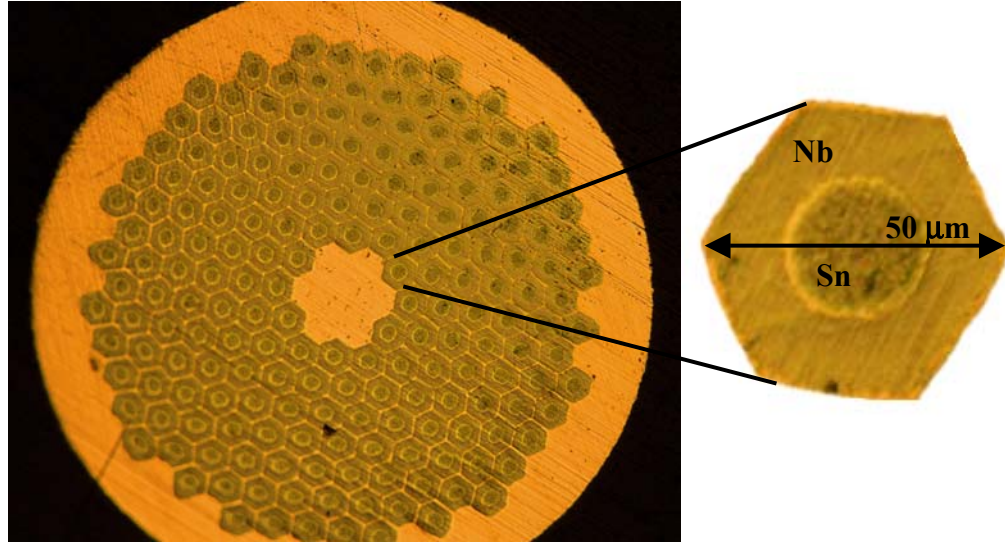


Figure 3.10 Powder in Tube (PIT) by Shape Metal Innovation Company (SMI).

tube acts as barrier between Cu and Nb₃Sn. The development of this technique has allowed producing long 36 and 192 filament strands. In laboratory, samples of 1332 filament strands were also obtained [36]. The next step for large scale PIT strand will be the realization of a 492 filaments strand with an effective filament diameter of about only 20 μm.

Property	SMI PIT
Wire diameter [mm]	1.005 ± 0.003
Filament diameter [μm]	< 50
Number of filaments	192
Sn pool diameter [μm]	25
Cu stabilizer [%]	45.3 ± .03
Sn% in the non-Cu	Not available
Nb% in the non-Cu	Not available
I_c at 12 T and 4.2K [A]	> 900
J_c at 12 T and 4.2K [A/mm ²]	> 2100
RRR ($\rho_{Cu@300K}/\rho_{Cu@4.2K}$)	> 100

Table 3.6 SMI PIT strand parameters.

Heat Treatment		Step 1	Step 2	Step 3
SMI A	Ramp rate [$^{\circ}\text{C}/\text{h}$]	150	120	
	Temperature [$^{\circ}\text{C}$]	590	675	
	Duration [h]	1/3	62	
SMI B	Ramp rate [$^{\circ}\text{C}/\text{h}$]	25		
	Temperature [$^{\circ}\text{C}$]	675		
	Duration [h]	110		
SMI C	Ramp rate [$^{\circ}\text{C}/\text{h}$]	25	25	25
	Temperature [$^{\circ}\text{C}$]	210	340	675
	Duration [h]	100	48	62

Table 3.7 SMI typical heat treatments for PIT strand.

Factors like the number of subelements, the quality of the powders and the presence of a ternary element characterize the conductor properties [33].

Figure 3.10 shows an unreacted PIT wire of 1 mm diameter SMI. This PIT strand was one of those used to perform the diffusion studies presented in this work. Its properties are presented in Table 3.6. Typical heat treatments suggested by SMI for PIT designs are detailed in Table 3.7.

3.5 MAGNET WINDING AND HEAT TREATMENT APPROACH

In order to wind the coil of a magnet the multifilamentary strands are bound



Figure 3.11 Superconducting Rutherford cable and extracted.

together in a cable. The multi-strand cable is preferred to a single wire for the following reasons:

- It limits the length requirement for wire manufacturing. A coil wound with a cable having n strands

requires piece lengths $1/n$ shorter with respect to a similar coil wound with a single wire;

- It allows strand to strand current redistribution in the case of localized defects or when a quench originates in one strand;
- It limits the number of turns and facilitates coil winding;
- It limits coil inductance.

The most commonly adopted cable is the so-called Rutherford type, in which the wires are twisted and compressed in two flat layers with trapezoidal shape, as

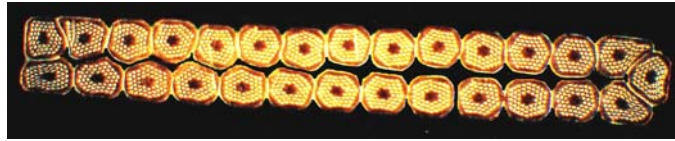


Figure 3.12 Cross section of Rutherford cable.

shown in Figures 3.11 and 3.12. For the High Field Magnet Project (HFM), Nb_3Sn cable samples of various packing factors

have been produced at Lawrence Berkeley National Laboratory (LBNL), at New England Electric Wire, and at Fermilab. The packing factor is the ratio of the sum of the undeformed strand cross section areas with respect to the area of the enclosing trapezoid. Figure 3.12 shows the cross section of a Rutherford cable made at Fermilab out of 28 MJR strands.

In the case of Nb_3Sn , the deformation and stress impressed on the strand during cabling does not allow heat treating the material before the cabling process, due to its strain sensitivity. However, once the cable is made, two approaches are possible: first wind the magnet, and then react it as a whole, or first react the cable, and then carefully wind the magnet. Within the HFM project at Fermilab both approaches are studied.

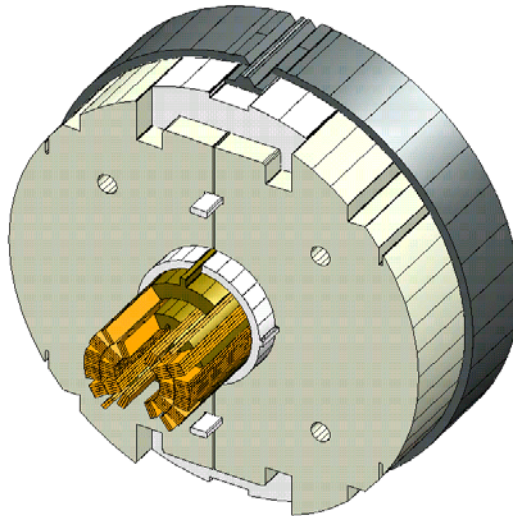


Figure 3.13 Cosine Theta Dipole Magnet cross section.

The Nb_3Sn dipole magnets

designed, manufactured and tested at Fermilab are the Cosine Theta and the Common Coil [39].

The single bore Cosine Theta, shown in Figure 3.13, is built by winding the cable over a shell surface. The bending radius at the end parts of the winding is very small, about 25 mm, and does not allow heat treating the cable before winding the dipole. The manufacturing technique used for the Cosine Theta Dipole is therefore of the *Wind and React* kind.

However, heat treating the whole magnet requires an insulation that withstands high temperature. In addition, vacuum operation of a large oven would be needed for long amounts of time due to the duration of the thermal cycles suggested by the companies, as seen in the previous section. Thanks to empirical optimization studies performed at Fermilab on a variety of Nb₃Sn strand designs strand reaction times have been reduced by a factor of 2 to 4, as can be seen in Figure 3.14, by increasing the maximum temperature to 700°C and replacing the low temperature steps by a slow ramp rate. However, since state-of-the-art high Sn strands have found to give rise to Sn leaks under small curvature radiuses, it is not clear whether such shorter heat treatments can be applied to the coil windings. To verify this, systematic studies are needed using cable. Whatever the outcome of such studies, reacting just the cable would make the reaction process less expensive, since it would require much smaller ovens.

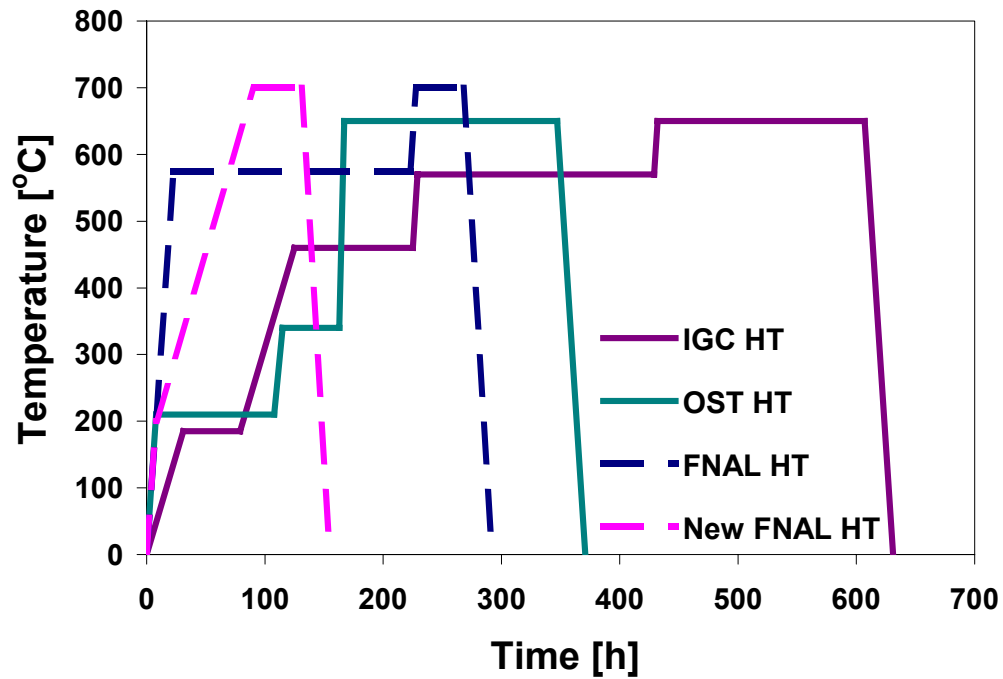


Figure 3.14 Typical heat treatments.

- IGC, Intermagnetics General Corporation (now Outokumpu).
- OST, Oxford Superconducting Technology.
- FNAL, Fermi National Accelerator Laboratory.

The *React and Wind* technique is explored with the Common Coil design, shown in Figure 3.15. In this case, the cables are wound on a flat surface. The 90

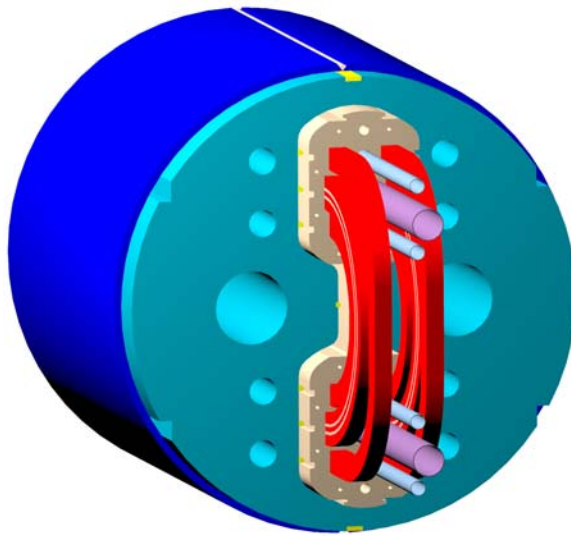


Figure 3.15 Common Coil Dipole Magnet cross section.

mm bending radius at the ends part should induce a minor stress in the cable, allowing to wind the cable after heat treatment.

A third technique could be contemplated in the case that the React and Wind approach failed. Such approach, that can be called Pre-react, Wind and React, involves pre-reacting the cable before winding the magnet, to subsequently achieve magnet

reaction in a large oven. This technique was studied in this work and results are presented in Chapter 8.

3.6 SUMMARY

The design and manufacturing processes of superconducting composite strands have been briefly explained in this chapter. Heat treatments cycles for the different Nb₃Sn strand technologies and the various reaction approaches for the magnet have been described. The heat treatment process is not yet optimized for providing the best superconducting properties of Nb₃Sn. Little is known on the kinetics of growth of this intermetallic compound and on the effects of the heat treatment parameters on its superconducting properties.

The intermetallic phase diffusion process taking place in the strands during the heat treatment is investigated in this work, and the superconducting properties of the strands are related to the heat treatment parameters in order to optimize the steps for the formation of the Nb₃Sn compound. Attention is also paid to reducing the heat treatment cost and the risk on the magnet fabrication process.

CHAPTER

IV

GROWTH KINETICS OF INTERMETALLIC COMPOUNDS BY DIFFUSION PROCESS

4.1 INTRODUCTION

Usually intermetallics can be obtained by crystallization from the liquid state or as a result of reactions in a solid phase [38]. Intermetallics are obtained by the formation and growth of at least one new phase due to diffusive interaction between two initial phases.

This latter process will be discussed in this chapter, since this is the mechanism presently used to form the Nb_3Sn intermetallic compound for the development of Nb_3Sn superconducting magnets, due to the extreme brittleness of this compound.

As mentioned in chapter 3, the formation of Nb_3Sn is obtained at temperature of about 700 °C by diffusion process at the interface between Nb and a Cu-Sn matrix or, in the same range of temperature, at the interface between Nb and a Cu- NbSn_2 matrix. In the first case the Cu-Sn matrix is obtained by the formation of intermetallic Cu-Sn phases via diffusion mechanism during low temperature HT.

Intermetallics can be formed by the interaction of two metals or also formed due to the diffusion interaction between alloys, both homogeneous solid solution or heterogeneous ones. In general they form by the interaction of two metals, depending upon the phase diagram [38]. Nevertheless not all the intermetallics to be expected from the equilibrium phase diagram are always realized simultaneously. Metastable intermetallics can also be formed [38]. Which intermetallic is realized due to the interdiffusion depends on the nucleation and growth kinetics [39].

4.2 FORMATION OF INTERMETALLICS BY DIFFUSION PROCESS

The nucleation and the growth kinetic of intermetallic phases will be examined in this paragraph.

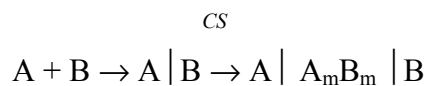
In the simplest case of interaction between metal A and metal B, only the intermetallic A_mB_m is formed at the interface. Two different viewpoints are usually discussed with regard to the mechanism of this process.

According to the first viewpoint, the intermetallic phase can appear only when the solubility limit of the solid solution is attained in the boundary layer of the solvent metal at a given temperature:



i.e. the phase A_mB_m appears diffusively (D) as a result of a phase formation (FT) in a supersaturated solid solution.

According to the second viewpoint, intermetallics are formed as a result of a chemical reaction at the interface of reacting metals, irrespective of their mutual solubility. The preparatory state in forming a new metallic phase at the contact surface of two metals in chemisorption (CS) [38], i.e. an adsorption in which chemical forces of interaction are developed:



The second scheme really is justified only when there is a total mutual insolubility of the components.

The evolution of a supersaturated solid solution formed at the metal interface will be now considered.

Dehlinger (1939) was the first to indicate that for the case of regular (fully disordered) solid solutions the sign of the second derivative of the thermodynamic potential with respect to concentration determines the sign of the diffusion equation:

$$I_A = -D \left(\frac{X_A X_B}{RT} \frac{\partial^2 \Phi}{\partial X^2} \right) \frac{\partial X_A}{\partial y}, \quad (4.1)$$

where X_A and X_B are the concentrations of the two components A and B, expressed in atomic fractions, Φ is the thermodynamic potential, I_A is the flux of atoms of A type, and D is the diffusion coefficient [38].

When $\partial^2 \Phi / \partial X^2 < 0$, the concentration difference intensifies spontaneously. In the case of a lower supersaturation, $\partial^2 \Phi / \partial X^2 > 0$, however, there exists a definite thermodynamic probability of a localized fluctuation in the composition of n atoms of the dissolved components in 1 mol of the solid solution.

The initial rate of precipitation is described by means of the activation energy nW that is essential for such a fluctuation [39], and the activation energy E of atoms of a precipitating type, needed for the diffusion of the dissolved atoms (Borelius 1938):

$$\dot{N} = K' \exp[-(E + nW)/RT], \quad (4.2)$$

where K' is a constant.

The necessary time for the formation of segregation is given by [41]:

$$t_1 = K_1 \exp[(E + nW)/RT], \quad (4.3)$$

where K_I is a constant.

Still another restructuring of the crystal lattice is necessary for the formation of the intermetallic phase, i.e. the work to be done to produce a critical nucleus:

$$A_{CR} = \alpha \sigma^3 V^2 / 2 \Delta G^2, \quad (4.4)$$

where α is the interface shape factor, V the atomic volume, σ the specific free surface energy of the nucleus, and ΔG the difference in free energy of atoms in the original lattice and in the nucleus. The rate of formation of the new intermetallic-phase nuclei, according to Becker (1938) [38], is:

$$\dot{N} = K^n \exp[-(E + A_{CR}) / RT], \quad (4.5)$$

and the necessary time for the formation of the new intermetallic-phase nuclei is [38]:

$$t_2 = K_2 \exp[(E + A_{CR}) / RT]. \quad (4.6)$$

The most probable structure of a precipitate is the one for which both the composition and size corresponds to a lowest activation energy.

One should also take into account the fact that the specific volume of the nucleus differs from that of the matrix. Then the deformation energy ε of the matrix surrounding the nucleus could be considered as a part of the change in thermodynamic potential due to the nucleation.

In such a case, the effective activation energy of the process is:

$$A_{eff} = A_{CR} + nW + n\varepsilon, \quad (4.7)$$

and the corresponding latent period is [38]:

$$t_0 = k_3 \exp[(E + A_{eff}) / RT]. \quad (4.8)$$

This form for latent period is confirmed also by some experimental results [38].

The growth kinetics of intermetallics that are of substantially different composition from the matrix can be now considered. It will be considered the diffusion of one single element at the interface between two pure metals. Assuming only one element diffuse inside the other, the flux of atoms I_i of the diffusing element i at the interface, in presence of the concentration gradient $\partial C_i / \partial y$ in the direction of growth, can be expressed by Fick's first law:

$$I_i = -D_i \frac{\partial C_i}{\partial y}, \quad (4.9)$$

where D_i is the diffusion coefficient of the i element. For solid and liquid metals the diffusion coefficient is a function of temperature and of concentration [39]. Only for a solution composed by two gases the diffusion coefficient has been experimentally verified to be constant with composition. Further details about the diffusion coefficient will be given in the next section.

Integrating equation (4.9) under the conditions of a constant diffusion coefficient, a constant concentration of the diffusing component at both the boundaries of the interlayer and a constant concentration gradient ($\partial C / \partial y = \Delta C / y$) across the interlayer, a parabolic growth law is obtained [39]:

$$y^2 = \frac{2}{a} \Delta C D t = k t, \quad (4.10)$$

where ΔC is the concentration difference at the boundaries of the layer, a is a constant that has the dimensions of a concentration (more details will be given

following), y is the layer thickness, t is the time and k is the rate of growth of the interlayer .

The parabolic growth law has a limited applicability also because the diffusion coefficient depends on the real structure of the metals and on the concentration. Consequently the diffusion flux will depend on nature and extent of boundaries between grains, in temperature, composition and concentration gradient [39].

The rate of growth of the interlayer can also be determined by considering the force acting on a diffusing atom. For a binary solution this force may be represented by the gradient of the free energy of the diffusing element i across the interlayer.

The free energy for a mole of the i element, at a constant pressure and temperature T , is defined as:

$$\bar{G}_i = G_i^0 + \beta T \ln a_i, \quad (4.11)$$

where G_i^0 is the free energy per unit mole of pure i at the temperature T , β is the Boltzman constant, and a_i is a coefficient that as the dimension of a concentration $a_i = \gamma_i C_i$, where γ_i is the coefficient of activity defined as the ratio of the partial vapor pressure of the component i and the vapor pressure of the pure component i , at temperature T .

The gradient of the free energy G_i along the growth direction of the interlayer is given by:

$$\frac{\partial G_i}{\partial y} = \beta T \frac{\partial \ln(\gamma_i C_i)}{\partial y} \quad (4.12)$$

The rate of growth of the interlayer can be expressed by the equation [41]:

$$\frac{\partial y}{\partial t} = -\alpha B_i \frac{\partial G_i}{\partial y}, \quad (4.13)$$

where α is a geometric factor correlated to the shape of the domain and to the growth conditions, B_i is the mobility of substitutional atoms i in the matrix, which is a function of the composition at a constant pressure and temperature [39]. Using the following thermodynamic dependence (when pressure and temperature are constant):

$$B_i = (D_i / \beta T) (\partial \ln C_i / \partial \ln a_i). \quad (4.14)$$

Then we obtain:

$$\frac{\partial y}{\partial t} \approx \alpha D_i \frac{\partial \ln C_i}{\partial y} = \alpha D_i \frac{\partial C_i}{C_i \partial y}. \quad (4.15)$$

After certain simplifications ($\alpha = 1$ for stationary interfaces; $\partial C_i / \partial y \approx \Delta C_i / y$; D_i and ΔC_i are constant) it follows that [42]:

$$\int_{t_0}^t y dy = \int_{t_0}^t D_i \frac{\Delta C_i}{C_i} dt. \quad (4.16)$$

When $t=t_0$, the thickness of the intermetallic compound (y) is equal to zero, and therefore:

$$y^2 = 2D_i \frac{\Delta C_i}{C_i} (t - t_0) = k(t - t_0), \quad (4.17)$$

where k is the rate of growth of the interlayer.

When $t \gg t_0$ equation (4.17) reduces to Tammann and Rocha's (1931) expression for growth rate [38]:

$$y = k\sqrt{t} . \quad (4.18)$$

When the conditions that allow simplifications are not justified, in particular, if D_i and $\Delta C_i \neq \text{const}$, then the time dependence of y deviates from the parabolic law. In the general case [38]:

$$y^n = k(t - t_0) . \quad (4.19)$$

4.3 DIFFUSION COEFFICIENT AND ACTIVATION ENERGY

Till now only one element diffusing inside the other has been considered. Generally the diffusion process at the interface between two pure metals is due to the diffusion of both the metals. Each element moves with a different velocity resulting in a different value of the diffusion coefficients. This phenomenon was first observed by Kirkendall who measured a displacement of some markers disposed at the interface between the two pure metals [39].

The different diffusion rate of two atoms A and B can be explained by a vacancy mechanism; the rate at which the two different atoms jump into the vacancies needs only to be different. Experimental measurements showed that elements with lower melting point diffuse faster [40].

The unequal mass flow causes the formation of voids in the region of the diffusion zone, from which the flow mass is greater. This can be explained considering that when an atom makes a jump, a vacancy moves in the opposite direction and an unequal flow of the two types of atoms must result in an equivalent vacancies flow in the reverse direction to the net flow of atoms.

In the case of two diffusing metals A and B, a relation can be established between the diffusion coefficients of A and B, (they will be indicated as D_A and D_B) and the global diffusion coefficient D that regulates the rate of growth of the

interlayer. The global diffusion coefficient resulting from the diffusion of both the two elements A and B can be expressed as [39]:

$$D = N_B D_B + N_A D_A . \quad (4.20)$$

The diffusion coefficient of the same element A can also be distinguished in self diffusion coefficient and heterodiffusion coefficient. This distinction can be understood if considering the phenomena accompanying the migration of atoms in the crystal lattice of a binary alloy AB:

1_ The thermal mobility of type A atoms in a homogeneous alloy AB, causes the process known as self diffusion of atom A. Fick's first law can be applied and the diffusion coefficient determined and identified with the true diffusion self coefficient value. This is also true for type B material. The self diffusion coefficient can be measured by radioactive tracers. The diffusion couple consists of an AB alloy, which has the same composition, but in an half there is a fraction of A element that is radioactive. If such a couple is heated the atoms are allowed to diffuse. The composition through the diffusing direction does not change but there is a redistribution of atoms, resulting in a change of concentration of A element radioactive isotopes. The self diffusion coefficient is determined by measuring the concentration change of the radioactive isotopes called tracers [39].

2_ Interdiffusion of components taking place in the case of a concentration gradient in alloy AB. The diffusion coefficient is called heterodiffusion coefficient. When the two metals diffuse, the global diffusion coefficient is given by a combination of the heterodiffusion coefficients of element A and element B.

3_ If the interaction of atoms A and B leads to the formation of an intermetallic compound $A_m B_m$, then new parameters emerge that have a practical significance: rate of formation k , and growth of an intermetallic layer. These parameters are connected with the one mentioned earlier, as shown in section 4.2.

The coefficient of heterodiffusion can be expressed in function of the mobility of the atoms by equation [39]:

$$D_i = \beta T B_i \left(1 + \frac{\partial \ln \gamma_i}{\partial \ln C_i}\right), \quad (4.21)$$

This relation was used first by Darken to analyze metallic systems [40]. He established a relation, experimentally verified, between self diffusion coefficient D_i^* and heterodiffusion coefficient D_i . Darken believed that the mobility of atoms B_i , determined by the average rate of flux during diffusion in the case of a gradient of free energy which is equal to unity for self and heterodiffusion, is equal for all substances. Thus the difference between D_i^* and D_i , entirely reduces to a different value of free energy in both the cases. In the case of self diffusion is [39]:

$$D_i^* = \beta T B_i. \quad (4.22)$$

Thus the relation between hetero diffusion and self diffusion coefficient is:

$$D_i = D_i^* \left(1 + \frac{\partial \ln \gamma_i}{\partial \ln C_i}\right). \quad (4.23)$$

Since the self diffusion coefficient is independent from concentration, its value can experimentally be determined with an high accuracy, using radioactive tracers, in pure metals. Furthermore since the diffusion process occurs in a relatively simple system, a theoretical interpretation can be given to the measured diffusivity. If considering an ideal solid solution of A and B, where the A concentration varies continuously in one direction, assuming the atoms jump randomly with the same probability of jumping into any surrounding vacancy, then the diffusion coefficient is independent from concentration and correspond to the self diffusion coefficient. For a body centered cubic crystal structure, the A atoms flux, perpendicular to the growth direction, from X plane to Y plane can be expressed as:

$$J_{X \rightarrow Y} = \frac{1}{6\tau} n_A a, \quad (4.24)$$

where τ is the average time of stay of an atom in a lattice site (thus $1/6\tau$ is the average frequency with which an A atom jumps from X to Y), n_A is the number of A atoms per volume and a the distance between the two planes. The flux of A atoms from plane Y to plane X is:

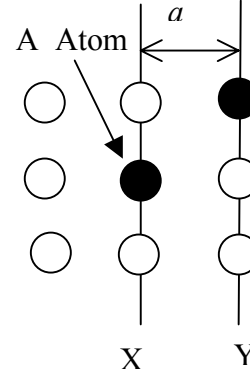


Figure 5.1 Atomistic view of a section of an hypothetical crystal.

$$J_{X \rightarrow Y} = \frac{1}{6\tau} a \left(n_A + a \frac{dn_A}{dy} \right), \quad (4.25)$$

The net flux J is then:

$$J = J_{X \rightarrow Y} - J_{Y \rightarrow X} = \frac{1}{6\tau} (n_A a - a(n_A + a \frac{dn_A}{dy})) = \frac{a^2}{6\tau} \frac{dn_A}{dy}. \quad (4.26)$$

If comparing this equation to Fick's first law (4.9), it can be deduced that, for a body centered cubic crystal, the self diffusion coefficient is related to the average frequency the atoms jump and to the geometrical characteristics of the crystal structure by the equation:

$$D_A^* = \frac{a^2}{6\tau}, \quad (4.26)$$

For a general crystal structure the self diffusion coefficient can be expressed as [39]:

$$D^* = \frac{\alpha a^2}{\tau}, \quad (4.27)$$

where α is a dimensionless constant depending on the structure.

The self diffusion coefficient depends on the temperature since the number of jumps into a vacancy made per second by an atom (l/t) is temperature dependent. The temperature dependence may be derived by considering the probability that an atom jumps into a vacancy and the numbers of vacancy that can form inside a crystal, n_v .

A vacancy inside a crystal increases its free energy by a quantity:

$$G_v = H_v - TS_m, \quad (4.28)$$

where H_v is the enthalpy increase due to the vacancies and S_m is the entropy of mixing a number of vacancies to the atoms of the crystal.

The numbers of vacancies that can form at the equilibrium is the one that minimize the free energy increment of the crystal (G_v) thus it can be calculated by deriving G_v in function of n_v ; this leads to the equation [39]:

$$n_v = n_0 \exp(-(\Delta H_f - T\Delta S_f) / RT), \quad (4.29)$$

where n_0 is the number of atoms in the crystal, R is the gas constant, T is the temperature, ΔH_f is the heat of activation, or the work to be done to form a mole of vacancies, ΔS_f is the entropy increase of the lattice due to introducing a mole of vacancies.

The jumping probability (r_v) for a mole of atoms is related to the energy barrier that has to be overcome to move into the vacancy and is related to the increase in entropy (ΔS_m) resulting from the strain of the lattice during a jump of a mole of atoms by the expression [39]:

$$r_v = A \exp(-(\Delta H_m - \Delta S_m) / RT), \quad (4.30)$$

where ΔH_m is the enthalpy change or energy barrier that must be overcome to move a mole of atoms into a vacancy and A is a constant depending on the number of atoms surrounding the vacancy and on the vibration frequency of the atom.

The number of jumps (r_a) made per second by an average atom in a crystal containing an equilibrium number of vacancies is given by the fractional ratio of vacancies to atoms n_v/n_0 times the numbers of jumps per second into the vacancy (r_v):

$$r_a = \frac{n_v}{n_0} r_v = A \exp(-(\Delta H_m + \Delta H_f) + (\Delta S_m + \Delta S_f)) / RT, \quad (4.31)$$

Substituting expression (4.31) to the equal quantity I/t in formula (4.27) it can be obtained the following temperature dependence for the self diffusion coefficient:

$$D^* = \alpha a^2 A \exp((\Delta S_m + \Delta S_f) / R) \times \exp(-(\Delta H_m + \Delta H_f) / RT), \quad (4.32)$$

where, summarizing, α is a dimensionless constant depending on the crystal structure; a is the lattice constant; A is a constant depending on the numbers of atoms surrounding the vacancy and on the vibration frequency of the atom; ΔS_f is the increase in entropy of the lattice due to the introduction of a mole of vacancies; ΔS_m is the increase in entropy resulting from the strain of the lattice during the jump of a mole of atoms; ΔH_m is the enthalpy to move a mole of atoms into the vacancies, and ΔH_f is the work to form a mole of vacancies.

The terms non depending on the temperature in expression (4.32) are usually indicated as:

$$D^*_0 = \alpha a^2 A \exp((\Delta S_m + \Delta S_f) / R), \quad (4.33)$$

and

$$E = \Delta H_m + \Delta H_f, \quad (4.34)$$

where E is called *activation energy* of diffusion and D_0^* is called *frequency factor*. The temperature dependence of the self diffusion coefficient can thus be expressed as:

$$D^* = D_0^* \exp(-E / RT), \quad (4.35)$$

It has been verified experimentally [43] that an exponential dependence on temperature fits also the values of the interdiffusion coefficient and the heterodiffusion coefficients; therefore it is commonly used the same expression for evaluating the diffusion coefficient in the general case of a substitutional solid solution:

$$D = D_0 \exp(-E / RT), \quad (4.36)$$

In these cases, however, the meanings of the activation energy and the frequency factor are not clearly understood yet, therefore they should only be considered as empirical constants.

Till now substitutional solid solution have been treated; the same considerations can be applied also to interstitial diffusion by the consideration that in this case presence of vacancies is not required for the solute atoms to move. Thus the temperature dependence of the diffusion coefficient can be described by a similar expression considering that the free energy change is only related to the free energy per mole needed for solute atoms to jump between interstitial sites ΔG_m . Equation (4.35) can be applied also to interstitial solid solution by using the values:

$$D_0^* = \alpha a^2 A \exp(\Delta S_m / R), \quad (4.37)$$

and

$$E = \Delta H_m, \quad (4.38)$$

where D_0^* presents the same expression as for the diffusion coefficient for substitutional solid solution except for the meaning of the constant A that here depends on the number of nearest interstitial sites and on the vibration frequency of a solute atom in an interstitial site. E is the activation energy needed to move a mole of atoms into interstitial sites.

For intermetallic compounds vacancies and interstitials present special features and much more complex behavior, as compared to pure metal [41].

For example in a pure metal all the bulk lattice sites are equivalent for the formation of a vacancy; in intermetallic compounds the various sublattices are not equivalent. The vacancy formation energy depends on the extent of off-stoichiometry, and the thermal vacancy concentration may be much larger than in pure metal. Also the migration of vacancies is not equivalent because sites are not equivalent and in a long range order alloy the jump of a vacancy between two neighboring sites, belonging to different sublattices, changes the long range order parameters and this increases the migration energy.

The structure of interstitials is not yet well known and in some cases several types of complex defects occur simultaneously.

In an intermetallic compound the movement of a vacancy is not random as in pure metals, but every successive jumps are correlated.

At present it does not exist a satisfactory theory of the equilibrium number and distribution of points of defects in intermetallic compounds as a function of ordered state. Therefore it is not possible to model kinetic properties thus to give a theoretical model for the frequency factor and activation energy. However it is experimentally verified [40] that also the rate of growth of an intermetallic layer, defined in section 4.2, has an exponential dependence on temperature similar to the one for substitutional and interstitial solid solution diffusion coefficient:

$$k = k_0 \exp(-E / \beta T), \quad (4.39)$$

where the meanings of the activation energy and the frequency factor should only be considered as empirical constants.

4.4 MECHANISM OF DIFFUSION IN INTERMETALLICS

Diffusion in pure metals and disordered solid solutions is realized by random jumps of defects such as vacancies and interstitial, as seen in section 4.3.

This interpretation is too simplified for intermetallics, since a random migration of the different atomic species leads to disorder. This process is thermodynamically disadvantageous, being restricted by the equilibrium conditions that are responsible for the existence of intermetallic compounds.

Thus, only those mechanisms of diffusion for which disordering does not occur, or is localized and transient, are considered.

One mechanism of diffusion in intermetallics is due to the migration of atoms along interstitial sites. When the diffusing atoms are significantly smaller ($r_A < 0.59 (r_A + r_B) / 2$) [38] with respect to the basic component, neither long range nor short range order in the compounds is broken. Several sublattices and several types of interstices with different surroundings of atoms types A and B exist in intermetallics. In this case the temperature dependence of D is more complex than the exponential one, and also the dependence with concentration is complex for intermetallics that exist over a large composition range [39].

A deficit of interstitial element usually exists in interstitial alloys, *i.e.* not all interstices of a given type are filled. Thus, the vacancy mechanism is valid also for interstitial phases with nearly complete filling of the interstices. Smirnov (1979) [39] assumed that the vacant interstices are structural ones, with number independent from temperature as compared with the equilibrium vacancies in the sublattice sites of a metal. Therefore the ratio D_A/D_B differs significantly from unity and changes both when the temperature rises and when the composition changes.

The relation between an interstitial and a vacancy was interpreted by Frenkel (1926) [39] as a dissociation of the lattice site into a pair of defects: a vacancy and an interstitial. After this, both the vacancy and the interstitial flux diffuses separately. The fast migration of the interstitial atoms can be realized both by jump to a neighboring interstice (simple mechanism) and by displacement of an atom from its lattice site (interstitialcy mechanism). Some parts of the interstitial recombine with vacancies, but other pair dissociate. This mechanism is valid when atoms of a smaller size ($r_A/r_B = 0.75-0.91$), for example Cu diffuses in the lattice of Sn.

When this mechanism acts in intermetallics it causes a transient destruction of local short range order near the site at which is dissociated before the recombination. Long range order is maintained. The interstitialcy mechanism in this case is limited to the sublattice possessing the smaller size, since disordering of the compound would be observed otherwise. The dissociative mechanism of diffusion in intermetallics compounds can lead to significant differences between the diffusion coefficients, i.e. $D_A \gg D_B$, where A is the component with the smallest atomic size.

In 1955, Slifkin and Tomizuka [39] suggested that in binary intermetallics diffusion occurs by a vacancy mechanism: since in most equiatomic compounds each atom of one type is surrounded by atoms of the other type, and a vacancy jumps only into the nearest neighbor position, then the two coefficients would be equal. In their opinion vacancies move alternately to sites occupied by the atoms A and B, and consequently an equal number of atoms of each type is involved. Lidiard (1957) pointed out inaccuracies in Slifkin's calculations [39]. He came to the conclusion that the equality of the two diffusion coefficients in a fully disordered lattice is an oversimplification, since vacancies that are moving due to jumps to the nearest lattice sites would leave behind a trail of atoms on foreign lattice sites. This would be an energetically unfavorable situation. To maintain the ordered state it would be necessary to have vacancies that would move along such a disordered trail in the opposite direction. Practically it means that diffusion is absent.

Pines in (1959) [39] concluded that in crystals both of compounds and of fully ordered solid solutions the position corresponding to atoms of different types are not equivalent. They form distinct sublattices. The equilibrium vacancy concentration can vary from one sublattice to another. The vacancies migrate only along their own sublattice sites. Such a mechanism provides an opportunity to avoid disordering at all stages of diffusion.

The mechanism that was proposed by Pines requires special discussion for the cases where empty sites (structural vacancies) exist in the crystal lattice of an intermetallic. If an intermetallic occurs over a concentration interval (berthollide), then structural vacancies could be formed due to the deviation of composition from stoichiometry. Consequently, the diffusion coefficients of the components would be increased at a rate that increases with the deviation from the stoichiometric composition. The activation energy would be decreased since the concentration of structural vacancies depends upon both composition and temperature.

Structural vacancies are not associated with only one component when the intermetallic is strictly stoichiometric (for example Cu in the compound Cu_3Sn), and no concentration dependence upon the composition and temperature is observed [39]. However, sufficient differences in the values of both diffusion coefficients ($D_A < D_B$) and activation energies ($E_A < E_B$) exist.

4.5 Nb_3Sn FORMATION

4.5.1 Thermodynamic Considerations

The interfacial structures at a diffusion couple between two elements it is composed exclusively of single phases appearing in the compositional sequence in which the corresponding phases appear according to the appropriate phase diagram [41]. In multicomponent systems, the only phases which will form in these diffusion couples are those phases which lies on the most direct route, following the two phase tie lines between two initial components of the couple

[23]. The phases, which most readily form, are those with the most rapid kinetics of formation.

Commercial tapes of Nb_3Sn have been produced for many years by heating Nb tapes in a liquid Sn bath. When these tapes are heated above 930°C single phase Nb_3Sn layers are formed, as shown from the Nb-Sn phase diagram illustrated in

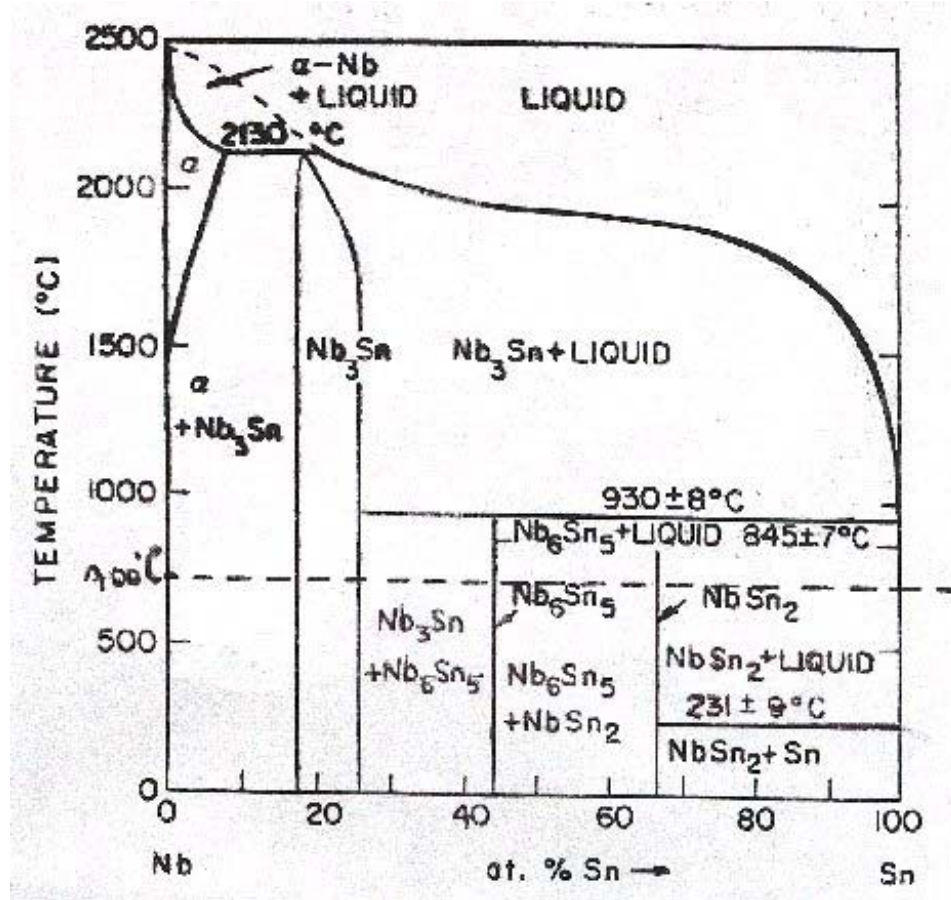


Figure 4.2 Nb-Sn phase diagram.

Figure 4.2. However when they are heated at lower temperatures the dominant compound which forms at the interface is not conductive. The difference in types of compound formation can be understood from the phase diagram of the Nb-Sn system. The only phase stable above 930°C is Nb_3Sn .

However at temperatures below 845°C , two other phases Nb_6Sn_5 and NbSn_2 are stable, and all the three phases will grow at the interface under proper conditions.

The relative thickness of these compound layers is primarily determined by the kinetic of growth. In this particular system NbSn₂ phase is the most easily formed, while the Nb₃Sn is the slowest growth layer.

However if the composition is at 75%at Nb and 25%at Sn the composite should eventually became totally Nb₃Sn since Nb₃Sn is the most stable phase in this system (although the time scale for this to happen will not be practical for most cases). As mentioned above the terminating phase is determined by the relative thermodynamic stability. The stability index, S.I., was introduced by Raynor [42] as a convenient measure of the thermodynamic stability of phase. The stability index for a compound A_xB_(1-x) is defined as:

$$S.I. = T_m [T_B + (T_A - T_B)(1 - X_B)]^{-1}, \quad (4.40)$$

where T_m , T_A and T_B , are the melting temperatures for the compound, the elements A and B respectively, and X_B is the atomic fraction of B in the compound.

This equation indicates that those compounds for which the melting point is above the line drawn between the temperature melting point for the elements A and B are more stable than those with the temperature below it.

There exist other indices such as the modified S.I. for the bronze process [43] that can provide some indications about the effect of using the bronze matrix on the relative phase stability in a binary system. For a better understanding of the compound formation process in filamentary composite strands a Nb-Cu-Sn ternary phase diagram is required; a section at 700°C of this phase diagram, is shown in Figure 4.3.

The A15 Nb₃Sn phase is the only relevant stable phase, other than the terminal Nb and Cu-base solid solutions Cu-Sn. The diffusion path from the Cu-Sn solid solution to the Nb-Sn solid solution passes only trough the A15 phase field.

. Thus this is the only phase formed at the interface between Nb and a Cu-Sn solid solution. However this diagram seems not to reflect some of the

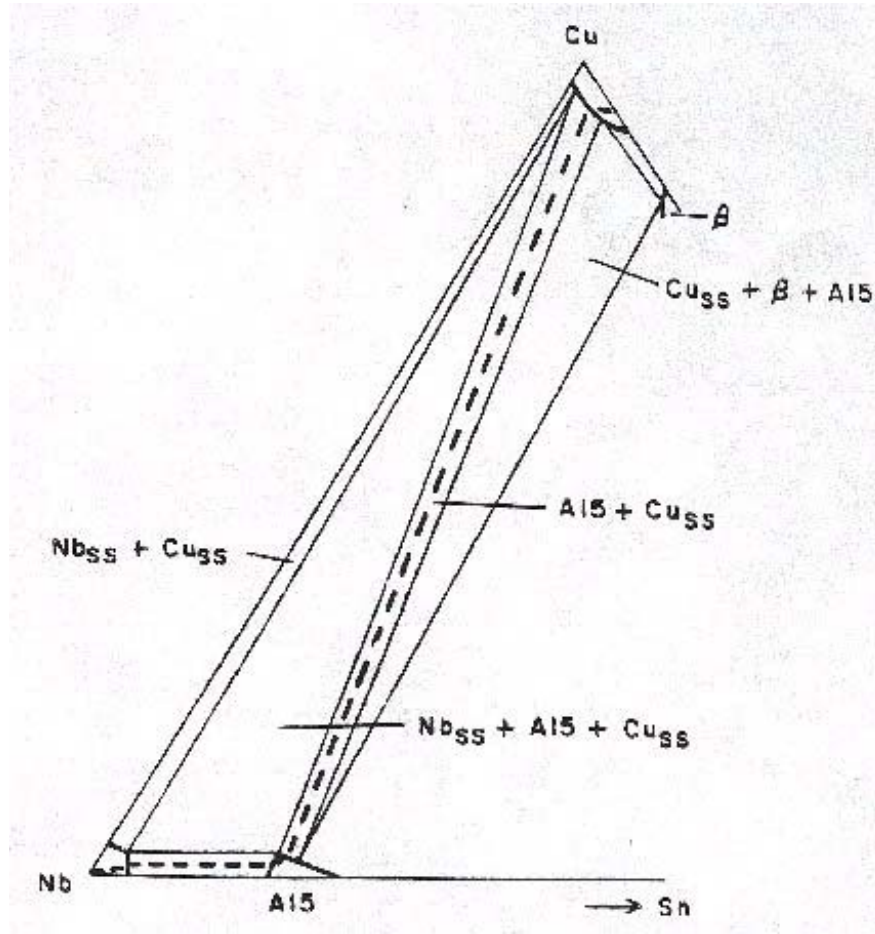


Figure 4.3 Nb-Sn-Cu phase diagram section at 700 °C.

experimental observations for example that the T_c of Nb_3Sn is always about 18K regardless of the composition of the bronze matrix, indicating the composition of Nb_3Sn at the bronze interface is nearly 25% at.Sn and that the amount of Cu in Nb_3Sn varies with the Sn concentration in the matrix [26].

4.5.2 Nb_3Sn Layer Growth

Early experimental results on Nb_3Sn formation revealed that the growth of the layer could be either faster [44], slower [45] than, or equal [23] to a parabolic dependence with time, i.e. $y \approx t^{1/n}$. The large deviations from the parabolic growth rate are primarily due to cracks in the layers for $n < 2$ [23], and to

depletion of Sn in the matrix for $n > 2$ [23]. When the experimental conditions are chosen to avoid these problems, the growth rate was found to be in most cases parabolic. Thus it appears that the mechanism for the growth is bulk diffusion and that a parabolic time dependence can be applied for the rate of growth.

However, some experimental works [23] suggested that the mechanism of growth of a Nb_3Sn layer is diffusion of Sn through grain boundaries as originally proposed by Farrell, Gilmar and Suenaga [45] rather than a bulk diffusion mechanism treated above.

Diffusion along grain boundaries in absence of compound formation was largely investigated. The diffusion in a system containing a single high diffusivity slab of width $2a$ in a semi infinite medium is described by the equation [23,45]:

$$D\nabla^2 C = \partial C / \partial t, \quad (4.41)$$

in the bulk of the medium, and:

$$D' \frac{\partial^2 C}{\partial^2 y} + \frac{D}{a} \frac{\partial C}{\partial x} = \frac{\partial C}{\partial t} \quad \text{at } y = 0, \quad (4.42)$$

at the slab, where D' is the diffusivity of the thin slab representing the grain boundary. Calculations [45] using this model indicate that the equiconcentration contours advance with a time dependence appreciably less than the $y \approx t^{1/2}$ law under certain conditions. This is primarily due to the leakage of flux into the bulk. However, when compound formation takes place at the interface, almost the entire flux will be carried to the growth interface and very little is lost to the grain. In fact, under most circumstances, the concentration in the grain boundary approaches steady-state conditions because the motion of the growth front is considerably slower than that of diffusion of atoms at the grain boundaries. Thus it is expected that a growth interface fed grain boundary diffusion will lead to a parabolic time dependence of the layer thickness, as in the case of a bulk transition.

The possibility of a non parabolic growth due to the boundaries conditions at the interface in a simplified model was investigated by Farrel et al [45]. Although it is possible to find conditions in which the time dependence is less than a parabolic one, it requires the Sn concentration at the growth front to be much less than 76% the concentration at the interface between Nb_3Sn and the Cu-Sn matrix. This is not possible because the atomic concentration of Sn in Nb_3Sn is in the range of 18%-25%, and, if the leakage of material from the grain boundary into the grains were responsible for the observed deviation from the parabolic growth, it would be necessary for Nb_3Sn to form at much less than 18% at Sn concentration.

Thus it is concluded that, when compound formation is governed by a simple grain boundary diffusion through a fixed array of grain boundaries, the growth of the layer will follow a parabolic time dependent formation of compounds with relatively small compositional limits, such as for Nb_3Sn .

4.6 Cu-Sn INTERMETALLIC COMPOUNDS

Figure 4.5 shows the Cu-Sn phase diagram. The only phases that can form by diffusion process at the interface between Cu and Sn below 580 °C are η , ϵ , δ , γ , α . Attention on this work is focused on three Cu-Sn phases that form at relatively low temperature and are Sn rich phases: Cu_6Sn_5 (η phase), Cu_3Sn (ϵ phase), and $\text{Cu}_{41}\text{Sn}_{11}$ (δ phase), whose density and composition range are listed in table 4.1.

Limits on the temperature are due to the “Wind and React” approach, as discussed in chapter 3.

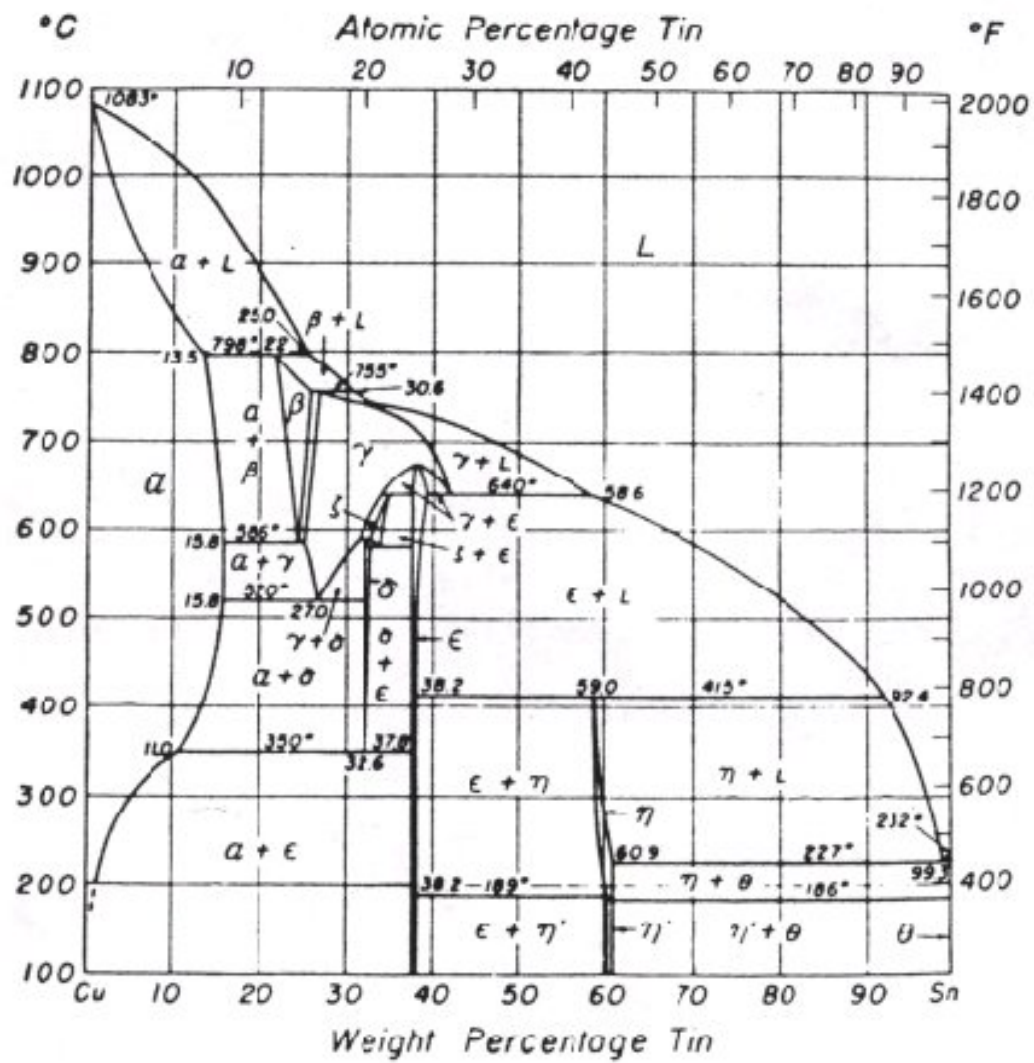


Figure 4.5 Cu-Sn phase diagram

	ρ [g/cm ³]	Range of Composition %Sn weight
Sn	7.29	
η (Cu₆Sn₅)	8.45	57.95-60.93
ϵ (Cu₃Sn)	9.14	38.2-38.37
δ (Cu₄₁Sn₁₁)	8.96	32.2-32.8
Cu	8.94	

Table 4.1 Cu-Sn phases density (ρ) and composition range.

As it is shown in Table 4.1 the composition range of ϵ , η and δ phase is very narrow; this allows to assume a constant concentration of Sn along the intermetallic layer during the layer growth by diffusion process.

A schematic illustration of the concentration trend at the boundary between pure Sn and pure Cu is shown in Figure 4.6, where only one intermetallic phase is considered to form.

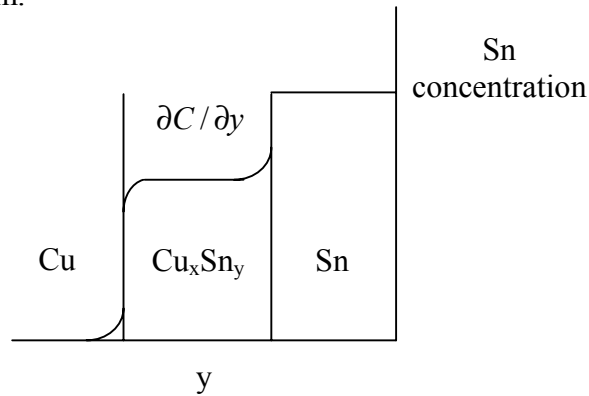


Figure 4.6 Schematic illustration of the concentration trend at the boundary between pure Sn and pure Cu, where only one intermetallic phase is considered to form.

Moreover it has to be noticed that if also the composition at the boundaries of the interlayer does not change, the concentration gradient along the interlayer during the growth can be assumed as constant.

4.7 SUMMARY

A brief introduction to the diffusion theory has been given in this chapter focusing the attention on the diffusion model for the growth kinetics of intermetallic layers. The rate of growth of the layer has been related to the temperature, to the activation energy and diffusion frequency. Although it has been shown that only in a few cases it is possible to find a physical meaning for these two latter parameters it has been observed experimentally that they can describe the growth of intermetallic compounds in function of time and temperature, accordingly to the experimental conditions and diffusion model applied.

As for the diffusion process taking place in the strands to homogenize the Cu-Sn matrix and to form the Nb_3Sn intermetallic compound, it is of great interest to evaluate the E and k_0 in order to predict the intermetallic volume versus HT parameters. In chapter 5, 8 and 9 it is presented a description of the evaluation method, experimental set up and result on the estimate of these parameters.

CHAPTER

V

INTERMETALLIC LAYERS MEASUREMENTS

5.1 INTRODUCTION

In order to investigate the growth kinetics of Cu-Sn phases and of the Nb₃Sn compound, intermetallic layer thickness measurements versus heat treatment (HT) time and temperature, are performed over different strand technologies samples and over Cu and Sn samples. These latter will be indicated as model to distinguish them from the strand samples.

This chapter describes the design of the Cu-Sn models and of the strands, the procedures and the instrumentations set up to obtain the layer thickness measurements.

Some procedures, techniques and instrumentation used to obtain the thickness measurement for the Cu-Sn system do not differ from the ones used to investigate

the Nb₃Sn formation. The procedures that differ substantially will be described separately.

A scheme of the samples and of the procedures is illustrated in section 5.6.

5.2 Cu-Sn SAMPLES

The following three paragraphs describe the design and the procedures needed to realize and heat treat the samples to investigate the Cu-Sn intermetallic phase growth kinetics.

Cu-Sn models are realized to perform thickness measurements versus HT time and temperature in order to calculate the diffusion frequency and activation energy of Cu-Sn intermetallic phases.

Thickness measurements versus time and temperature are also performed in ITER and MJR strands, which characteristics are given in section 3.4, to investigate the Cu-Sn diffusion process taking place in the strands. The intermetallic layer growths in the Cu-Sn models and in the strands are then compared.

5.2.1 Cu-Sn models design

In order to calculate the diffusion frequency and activation energy of the Cu-Sn intermetallic phases the Cu-Sn samples has to provide an “infinite” source of tin and copper to the layer growth. This is necessary to acquire enough thickness data versus HT time and temperature.

The limited Sn content in superconducting strands does not allow acquiring enough thickness measurements since the Sn exhaustion hinders the growth of the intermetallic layer. Moreover the Cu-Sn interface in the strand has a non planar geometry due the small curvature radius of the Sn pool (see section 3.4). This may complicate the evaluation of the diffusion frequency and activation energy.

To overcome the problems related to the strands, in order to estimate the activation energy and diffusion frequency of the Cu-Sn intermetallic compounds Cu-Sn models are designed.

Cu-Sn models are realized by casting liquid Sn in a previously drilled Cu bar. The Copper and Tin has been supplied by Intermagnetic General Corporation (IGC) and are of the same quality than those used for superconductor strands manufacturing.

The models have been designed with two different geometries corresponding to the range of temperature they have been heat treated.

In the first model, shown in Figure 5.1a), a hole of 10 mm in diameter has been axially machined in a 20 mm in diameter Copper bar and filled with Tin. After each heat treatment sequence, a transverse slice is removed using a slow rotary diamond saw. Then the sample surface is polished and observed at the optical microscope. This type of sample, that will be indicated as A model, has been heat

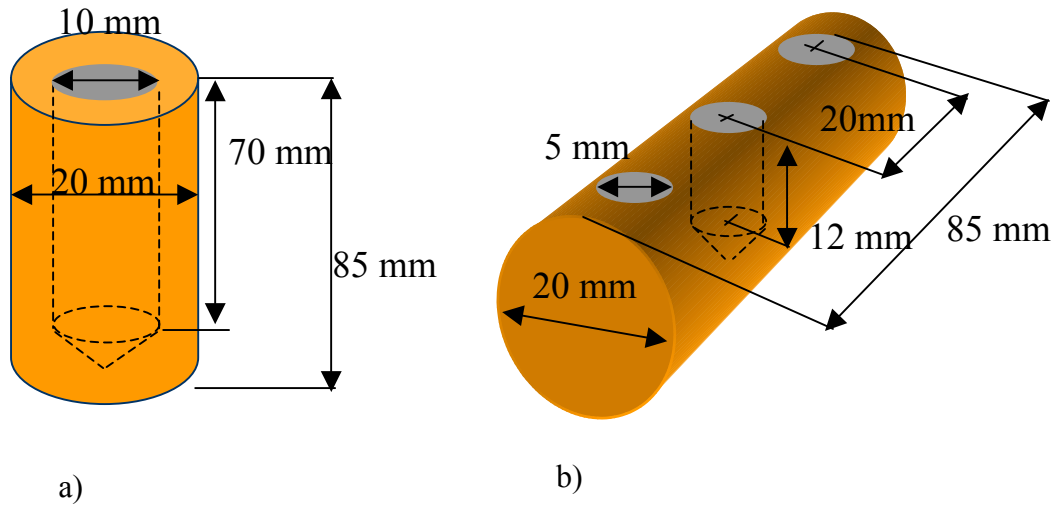


Figure 5.1 Cu-Sn models.

- a) Cu-Sn model used for heat treatments @ $150^{\circ}\text{C} \leq T \leq 210^{\circ}\text{C}$.
- b) Cu-Sn model used for heat treatments @ $240^{\circ}\text{C} \leq T \leq 550^{\circ}\text{C}$.

treated at $150^{\circ}\text{C} \leq T \leq 210^{\circ}\text{C}$; in this range of temperature η phase, ϵ phase and Sn are solid phases.

The second type of model, shown in Figure 5.1b), is realized by drilling several 5mm in diameter transversal holes (one for each heat treatment time at a fixed temperature) into the Cu bar. The holes are then filled with Sn. After each heat treatment sequence at a fixed temperature, a transverse slice including a Sn filled hole, is removed and cut into two halves in the middle of the Sn pool; then is polished and observed at the optical microscope.

This model, that will be indicated as type B model, has been used for heat treatments at $240\text{ }^{\circ}\text{C} \leq T \leq 550\text{ }^{\circ}\text{C}$; in this range of temperature the Sn is liquid, η phase grows inside the liquid, while ϵ phase grows inside the liquid at $T \geq 415\text{ }^{\circ}\text{C}$. When a solid phase grows inside a liquid, it can separate from the interface and either fall, by gravity, inside the liquid or float into it.

The feature of the second model is to monitor eventual dispersion of solid phases into liquid phases. No drops of η , ϵ or δ phase, inside pure Sn have been observed in any sample.

5.2.2 Sn Casting Technique

The casting of the Sn in the previously drilled Cu bar is realized by heating the Cu bar above the melting point of Sn while filling the holes with Sn strips.

The Sn strips are obtained from a 30 mm in diameter Sn bar. The Sn bar is cut into slices with a steel handsaw. After cleaning with Acetone ($\text{C}_3\text{H}_6\text{O}$), the Sn slices are melted inside a copper container by heating the container with a Prest-O-Lite Air-Acetylene Torch. Once melted, the Tin is poured over an Aluminum sheet, cleaned with Acetone, to obtain a Sn sheet about 1-2 mm thick. The Sn sheet is then cut with shears cleaned with Acetone. All the tools used to handle the Sn strips from this stage are cleaned with Acetone. Every precaution is taken to avoid contamination of Copper and Tin during all the stages of samples preparation.

The Cu bar is machined to obtain the holes. After drilling the holes, the Cu bar is washed with of Micro 90 (a solution of 2.5 fluid ounces per gallon of H_2O) in order to clean the copper from some machining oil residue. Micro 90 is a cleaning solution commonly used to remove blood and biological materials from metals.

SP44, a soldering flux, has been used before and during the casting of Sn, to remove the Copper Oxides from the surface of the Cu bar holes. SP44 is a paste version of the liquid n^o1544 flux by Kester Solder. 1544 flux is an activated Rosin (Abiatic Acid) mixed with Petroleum Jelly; it is not corrosive and non conductive.

The energy needed for the reaction between the copper oxides and the SP44 is provided by heating the Cu bar into a preheated furnace at 210°C for 10 minutes. The Cu bar is removed from furnace and its hot holes are filled with SP44, then the Sn strips are inserted while heating the Cu bar. The copper bar is heated for a few minutes to favor the flux excess, (which has a smaller density than the one of the Sn), to come to the upper surface of the holes.

Initially the casting was performed by heating the Cu bar with an Oxy-Acetylene torch. This procedure has been then modified because the Oxy-Acetylene torch does not allow controlling both temperature staidness in time and its uniformity along the Cu bar axis. This leads to a complete inability in reproducing the same heating temperature and time along the axis of the Cu bar or between different samples.

For these reasons the Oxy-Acetylene torch has been replaced by a hot plate, shown in Figure 5.2.



Figure 5.2 Hot plate Sn casting procedure.

With the hot plate it is possible to control the temperature and to heat more uniformly the Cu bar along its axis. The new casting procedure is the following. The preheated Cu bar is placed into an aluminum groove and is put over the surface of a Termolyne compact hotplate at 270 °C. After filling the holes with SP44,

the Sn strips are inserted. The copper bar filled with Tin is then covered with an aluminum can in order to reduce the heat dispersion to the atmosphere. After a few minutes the aluminum can is removed and more tin strips are inserted into the holes full of liquid Sn. This procedure helps to remove the SP44 since the liquid

mixture of Tin and flux is pushed to overflow from the bottom to the upper surface of the hole.

All the samples heat treated above 400 °C have been realized by casting the Sn with the hot plate.

The improvement of the Cu-Sn interface uniformity achieved with the new casting technique is shown in Figure 5.3.

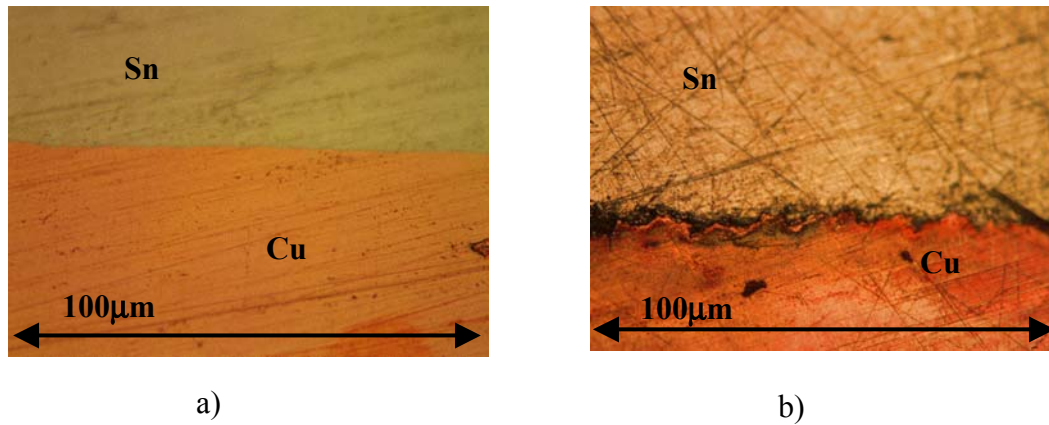


Figure 5.3 Cu-Sn interface after casting.

a) Hot Plate Casting.

b) Oxy-Acetylene Torch Casting.

Initially some efforts were spent in avoiding using the SP44, in order to be sure not to have some residual paste contamination between the Cu-Sn interface. Some experiments were carried on trying to remove the Copper Oxides with a solution of 15% in volume of HCl saturated with NH_4Cl before casting the Sn. This technique did not work because the Copper oxides too fast in atmosphere and it was not possible to work under inert atmosphere.

A microchemical quantitative X-Ray analysis has been performed in order to measure eventual contaminations. The concentration of impurities found in the intermetallic compound layer was comparable with the one found in two slices of pure Cu and Sn, prepared for microscopic analysis with the same procedure used for the Cu-Sn models.

5.2.3 Cu-Sn Samples Heat Treatment Procedure

After casting the Sn, the Cu bar is axially machined to remove some Sn and SP44 residues from the outer surface; then is cleaned with Micro 90 and placed into a Pyrex tube.

The Pyrex tube works as a container for inert atmosphere and allows to heat treat the samples using a furnace that is not provided with a vacuum system pump or a gas purge system.

The diameter of the Pyrex tube is reduced at its upper extremity by working it while heating with an Oxygen-Propane torch. The temperature of the flame produced by the Oxygen-Propane torch can reach, in the hottest region, 2700 °C; this allows to easily work the Pyrex, that has a softening point of 820 °C and a working point of 1245 °C.

A flow of Nitrogen is purged into the Pyrex tube for 20 minutes. The Pyrex tube is then sealed by working it while heating with the Oxygen-Propane torch and slowly removing the Nitrogen tube.

The Cu bar sealed in the Pyrex tube is then introduced into a preheated furnace.

The furnace provided by Thermolyne has a maximum operating temperature for continuous use of 1010 °C and 1093 °C for intermittent use. The furnace chamber is heated by four electric resistance heaters embedded in a refractory material. The chamber is insulated with ceramic fiber insulation, and the temperature is controlled by using a Chromel/Alumel thermocouple. The control is located under the furnace, insulated from the chamber. The precision specified in the catalog of the furnace is ± 5 °C.

At the end of the heat treatment the Cu bar is removed from the furnace and let cool down at room temperature. Since the Sn is liquid in most of the samples, it has not been feasible quenching the sample in cold water.

After cooling, the Pyrex tube is cut with a Pistorian saw. Then a slice of the Cu bar is cut and prepared for microscopy. The remaining bar is heat treated back again to complete the following HT duration. This procedure is repeated till the last duration of the HT is achieved.

The procedure used for heat treating the ITER and MJR strands is the same used for the Cu-Sn models. They are sealed into Pirex tubes with the same procedure used for the models, and heat treated into the same furnace. The only step that distinguish the heat treatment procedures of the strands from the one of the models is the cooling. After removing the strands from the furnace they are quenched in water at room temperature.

5.3 NB-SN-CU SAMPLES

The following two paragraphs describe the design and the procedures needed to realize and heat treat the samples for investigating the Nb₃Sn intermetallic compounds growth kinetics. The Nb₃Sn formation is investigated at the interface both between Cu-Sn intermetallic compounds and Nb, in the IT technology, and between NbSn₂ sintered powders, Cu layer and Nb, in the PIT technology.

5.3.1 Nb-Sn-Cu Samples Design

In order to estimate the diffusion frequency and activation energy of the Nb₃Sn compound growing at the interface between Nb and Cu-Sn ϵ phase (CuSn₃) (as it will be shown in chapter 8 the ϵ phase seems to be the most interesting Cu-Sn phase, as for the reaction cycle of Nb₃Sn) many efforts were spent in realizing a sample that could provide an “infinite” source of Nb and ϵ phase. The initial idea was to obtain a rod of ϵ phase to realize a model similar to the Cu-Sn one. However the attempts were not successful. Two different procedures were followed: by diffusion process and by melting Cu and Sn powders. The diffusion process to form a consistent thickness of ϵ phase is very long even at high temperature (630 °C was also investigated). The problem encountered with the powders was the presence of Cu oxides and the non possibility to heat treat the powders at high temperature to melt the Cu and separate by gravity the oxides.

The phase growth kinetics of Nb₃Sn is investigated over the strands to estimate the Nb₃Sn volume formed versus HT time and temperature.

PIT strands and IT strands with a large filament design are chosen in order to perform the Nb_3Sn layer thickness measurements at the optical microscope, since the magnification of the microscope does not allow measuring the Nb_3Sn thickness formed in a fine filament design strand.

The characteristic of the PIT strand are given in section 3.4.

The IT Nb large filament strand, shown in Figure 5.4, has been provided by Oxford Superconducting Technology (OST).

The characteristics of this strand are shown in Table 5.1.

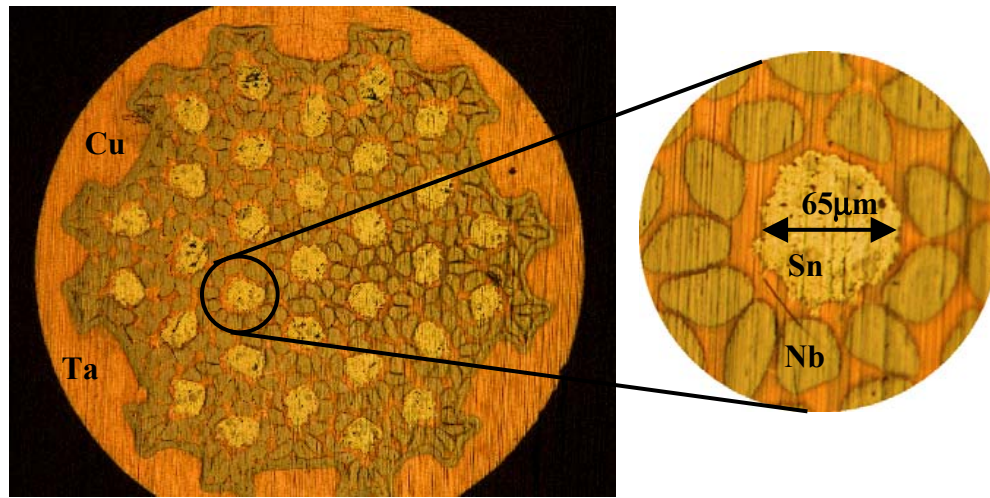


Figure 5.4 Internal Tin (IT) Nb large filaments strand by Oxford Superconducting Technology (OST).

	IT by OST
Wire diameter* [mm]	1.00
Filament diameter**[μm]	35
Sn pool diameter** [μm]	65
Cu fr. %***	41.0
Sn wt. %*	20.0
Nb wt. %*	36.6
Number of subelements*	310
Number of filaments*	31

Table 5.1 IT, Nb large filaments by OST.

* Design parameters.

** Measured.

*** Copper ratio.

5.3.2 Nb-Sn-Cu Samples Heat Treatment procedure

Short lengths of the IT and PIT strands are heat treated at high temperature, (750, 700 and 650 °C), in a tube Argon purged furnace that can provide a maximum temperature of 1100°C over a cylindrical volume of 140 mm of diameter and 380 mm of length.

The temperature of the furnace is measured with a thermocouple for each HT. The statistical error has been measured to be less than 1%.

The HT procedure is the following: the samples are inserted in the furnace; the temperature is raised to the set point value with the possibility to chose the ramp rate. After the programmed time HT at the set point temperature the furnace chamber starts cooling to room temperature.

The strands are extracted from the furnace and a short length is cut for microscopy analysis. The remaining strand is put back in the furnace for the following HT at the same set point temperature. The HT cycle of the strand ends when the duration of the last HT (given by the sum of the previous HT duration plus the last one) is achieved.

5.4 SAMPLE PREPARATION FOR MICROSCOPIC ANALYSIS

After the heat treatment, both the Cu-Sn samples and the Nb-Sn-Cu samples are prepared to be observed both at optical microscope and at the electronic microscope. Besides measuring the intermetallic layer thickness at the optical microscope, the composition of the intermetallic has been checked by X-Ray microchemical analysis for each sample.

The preparation procedures used for the strands to investigate the Cu-Sn system are different from the one used for the Cu-Sn models.

Both the strands used to investigate the Cu-Sn system and to investigate the Nb₃Sn growth kinetic, require to be assembled in a mold and then polished, while the Cu-Sn models only require a surface polishing.

The molds for the observation at the electronic microscope are also different from the one for the observation at the optical microscope.

Both the strands molds and the Cu-Sn models require to be cut and polished before microscopy. The cut and polishing procedures used for the Cu-Sn models, and for the strands molds are the same.

5.4.1 Strand Mold for Optical microscopy

Epoxy molds, shown in Figure 5.5, are realized in order to observe the cross section of the strands at the optical microscope.

The ends of the wires are fixed to the bottom of a cylindrical plastic container by Plastilina; the container is then filled with degassed liquid epoxy. The internal surfaces of the plastic container are previously sprayed with mold release 300 to avoid epoxy stick to it.

Epoxy, provided by BUHELER, is a mixture of Isopropyl Denediphenol Epichlorohydrin resin, Alkil Glycidyl Ether, Polyacrylate Ether. At room temperature has a viscosity of 100cps but when mixed with a hardener it can cure rapidly. The composition used is 15g of Epoxy and 3g of curing agent (a mixture of Diethylenetriamine and Hydroxyethyldiethylenetriamine); this composition

allows a curing time of about 1 hour.

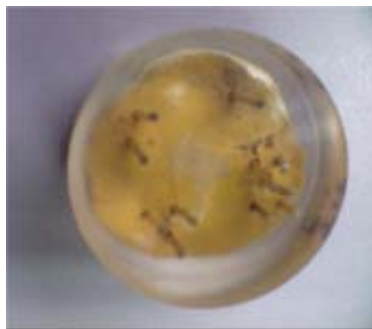


Figure 5.5 Strands mold for optical microscopy.

The epoxy and hardener are steered to obtain an homogeneous mixture. The mixture is then put under a degasser cup to allow the gases, dissolved inside the mixture, to evaporate. The scope of degassing the mixture is to avoid the formation of macroscopic voids once this is cured. The volume inside the degasser is pumped by a ChemStar mechanical vacuum pump till the pressure of

0.05mmHg. The mixture is kept under vacuum for 40 minutes.

Voids has to be prevented from the mold surface in order to avoid some material from the polishing grid to be trapped into them and contaminate the grid at smaller mesh, see next paragraph.

After degassing, the epoxy is poured into the plastic container and cured for 8 hours. Once the epoxy is cured, the plastic container is removed.

5.4.2 Strand Mold for Scanning Electron Microscopy

The mold for Scanning Electron Microscopy has to provide an electrical continuity that allows the sample to have the same electronic potential of the sample holder. The sample needs an electrical continuity to properly interact with the X-Ray, secondary electrons and backscattered electrons generated inside the electronic microscope [46].

The electrical continuity is realized by using electrical conducting epoxy and a copper container.

The strands are placed into several holes drilled at the bottom of a Cu container, and some electrical conductive epoxy, in a viscous form, is poured into the container; the remaining volume of the container is then filled with non electrical conductive epoxy (see previous paragraph for the composition and for the procedures used to degas and cure the non conducting epoxy). Figure 5.6 shows the mold ready for microscopy.



Figure 5.6 Strands mold for scanning electron microscopy.

The electrical continuity of each strand has been then checked with a tester.

5.4.3 Samples cut



Figure 5.7 Slow rotary saw equipped with wafering blade.

Both the two types of strands molds, for electronic and optical microscopy, and the Cu-Sn models, are cut with a low speed diamond saw, shown in Figure 5.7, at the speed of 100 rpm.

The blade is a diamond wafering blade used to provide precise and accurate sectioning of metallographic

samples. This blade has diamonds bonded in a metal matrix along the outer surface. The blade has a thickness of 0.5 mm and is lubricated with a Petroleum distillate oil base.

The samples are glowed to the sample holder, paying attention to avoid excess of glow that could result in non parallelism of the two surfaces of the sample; then the samples are placed in correspondence of the blade. The cutting time ranges between 2 and 3 hours, depending on the mold type.

After cutting the samples are cleaned with a solution of Micro 90 and water to remove oil residues, then they are finally washed with water.

5.4.4 Samples polishing

Polishing is a necessary step to obtain a smooth and clear surface before observing the samples at the microscope.

The polishing step can be repeated several times during the life of the sample because it can oxide or be easily damaged even if carefully handled.

Before polishing the samples are rinse with a solution of Micro 90 and water, then finally rinsed with water. This is done to prevent a contamination of the polishing grid with residues of larger size than the one of the abrasive particles of the grid.

Polishing is done with a sequence of polishing grid with different abrasive particles dimensions, starting with the biggest one.

The first two grids consist of abrasive roll paper with 400 and 600 mesh (the dimensions of the abrasive particles are smaller than 37 and 20 μm). Polishing is done by slowly rubbing the sample against the surface of the grid previously sprayed with a mixture of liquid soap and water.

The second step, that gives a better superficial finish, is done by using a diamond suspension. The diamond suspension is sprayed into a polishing clothe glowed to a slow rotary wheel. The samples are gently pushed against the surface of the polishing clothe till the surface reaches the right finish.

The diamond suspension is oil base and has polycrystalline spherical abrasive diamond that provides more cutting facets than monocrystalline diamond. It is

recommended to polish samples composed of different materials or different hardnesses; provides minimal surface deformation and is easy to remove with water and soap.

The samples are first polished with a diamond suspension of 6 μm abrasive diamond size, then washed with soap and water and then polished again with a diamond suspension of 0.5 μm abrasive diamond size. The polishing cloth used for the 6 μm polishing is a Nylon fiber, the one used for the 0.5 μm is a Mastertex fiber.

Between each different step of the polishing the samples are washed with soap and water in order to avoid a contamination of the polishing grid with residual particles from the previous one.

5.5 LAYER THICKNESS MEASUREMENTS

EXPERIMENTAL METHOD

The thickness measurement of the intermetallic compound layers is performed using a Nikon optical microscope equipped with a CCD camera and Spot software.

For the Cu-Sn models the rectangular surface area of the intermetallic layers is measured and divided by the length of the interface to determine the mean thickness of the layer.

The measurement is repeated in four different locations for each sample.

For the Type A model the four locations were placed at an angular distance of 90 deg.; for the type B model they are located at the top and at the bottom of each interface, as shown in Figure 5.8.

For both the strands used to investigate the Nb_3Sn formation and the Cu-Sn system, the intermetallic compound layer thickness is obtained by measuring the circular surface area delimited by the outer and inner boundary of the layer and measuring the surface area delimited by the inner boundary of the layer. The

intermetallic compound mean layer thickness is then calculated by assimilating the geometry of the layer to a circular annular.

The measurement is repeated for four different Nb filaments (for the samples used to investigate the Nb_3Sn formation) and for four different Sn pools (for the

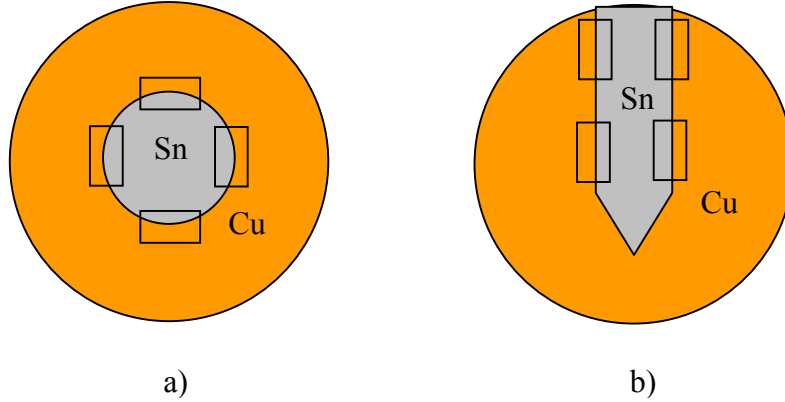


Figure 5.8 Schematic cross section of the two Cu-Sn models: Cu-Sn phases area and length measurement at the interface between Cu and Sn to compute average thickness. The measurement is repeated in 4 locations of the interface. a) Type A model b) Type B model.

samples used to investigate the Cu-Sn phase growth). In this way it is possible to obtain a mean thickness value of the layer, one for each of the four measurements, over a Nb filament or Sn pool.

The measurements have been performed at different magnification of the optical microscope depending on the thickness dimension of the layer. The magnification used for the samples heat treated at temperature $T \leq 210^\circ\text{C}$ is 500X. For the Cu-Sn models, this allows an estimation of the mean thickness of the layer over a length of $230\text{ }\mu\text{m}$ for each of the four measurements. The magnification used for samples heat treated at temperature $T > 210^\circ\text{C}$ is 200X. For the Cu-Sn models this allows an estimation of the mean thickness of the layer over a length of $575\text{ }\mu\text{m}$, for each measurement.

5.6 SUMMARY

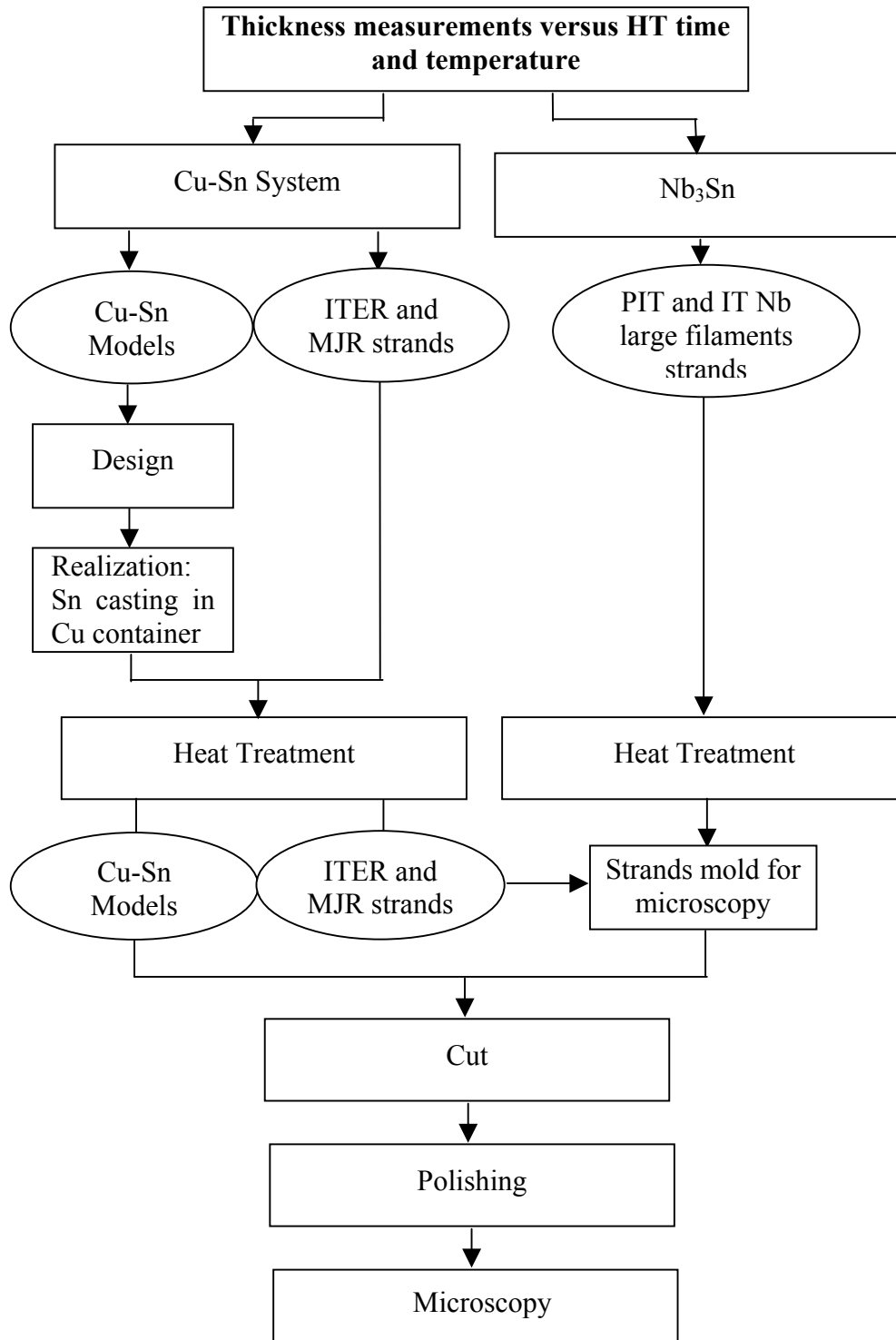


Figure 5.9 Scheme of the samples and of the procedures to acquire thickness measurements

The design of the samples and the procedures followed to obtain the intermetallic thickness measurement versus HT time and temperature to investigate both the Nb_3Sn and the Cu-Sn intermetallic compounds growth kinetics have been described in this chapter. A schematic description is given in Figure 5.9.

The data acquired on the Nb_3Sn and on the Cu-Sn intermetallic phases growth kinetics will be shown respectively in chapter 9 and 8.

CHAPTER

VI

CRITICAL CURRENT MEASUREMENTS

6.1 INTRODUCTION

The critical current (I_c) measurement techniques and the experimental setup are described in this chapter.

I_c is defined for a fixed temperature and magnetic field as the maximum current that can be carried by a superconductor at the transition to the resistive state. Since this phenomenon is not instantaneous, some criteria are here introduced in order to compute the I_c value from the experimental data.

6.1 CRITICAL CURRENT MEASUREMENTS

EXPERIMENTAL SETUP

Measurements of critical current presented in chapter 8 and 9 were acquired at the Short Sample Test Facility (SSTF). This facility was developed starting in 1998

at the Technical Division, within the High Field Magnet Project (HFM), in order to perform critical current measurements of binary and ternary NbTi, and Nb₃Sn samples from commercial and R&D strands. Measurements at different temperatures and different fields can be obtained in a Variable Temperature Insert (VTI) within a 15/17 T magneto cryostat (Teslatron), supplied by Oxford.

6.2.1 The magneto-cryostat

The magneto-cryostat (Teslatron) supplied by Oxford Instruments is shown in Figure 6.1 [47]. It consists primarily of a vacuum insulated helium dewar (Main Bath) containing a superconducting solenoid at the bottom. To allow measuring at different temperatures, the main cryostat feeds a second smaller helium cryostat, called Variable Temperature Insert (VTI), which is inserted inside the main dewar, down into the solenoid bore. According to Oxford specifications, the VTI allows experiments in a temperature range between 1.5 K and 200 K at atmospheric pressure.



Figure 6.1 Teslatron and piping.

A three days cooling procedure is necessary to fill the dewar with liquid helium to reach 4.2 K. This is the equilibrium temperature of the system thanks to natural evaporation of helium. To operate at temperatures higher or lower than 4.2 K, a PID control is used. An Oxford software written in LabView automatically controls a heater placed at the bottom of the VTI that can be operated to increase the temperature. Alternatively, the aperture of a needle valve located between the Main Bath and the VTI can be regulated to increase coolant flow and force the temperature to drop. This temperature control system is made more effective by

connecting the VTI to a vacuum system. A Cernox monitors the temperature in the VTI and in the magnet. The helium level in the Main Bath is measured by a sensor consisting of a superconducting wire that extends from the top to the bottom of the dewar. The portion of wire below the liquid surface at 4.2 K shows a superconducting behavior, whereas a small heater on the wire ensures that the upper part be kept above its critical temperature. A current is made to flow in the wire at some fixed intervals, and the value of its total resistivity allows deriving the percentage of helium in the bath. The usable helium volume in the Main bath is 42 liters. The helium level in the Main Bath is measured every few minutes. The VTI helium level is measured every few seconds by a similar superconducting sensor placed on the probe used for the measurements.

6.2.2 Electronics and data acquisition software

To control all the measurement parameters the following instruments shown in Figure 6.2 are required:

- Power supply to operate the magnet;
- Power supply to drive current in the sample;
- Helium level meter;
- Temperature controller;
- Nanovoltmeter to measure the voltage drops between taps;
- Scanner to switch the signal between the taps.

The magnet is controlled by an Oxford Intelligent Magnet Power Supply (IPS 120-10) with a GPIB output. It provides a bipolar current and allows the magnetic field to be swept



Figure 6.2: Hardware and electronics.

National Instruments' software LabView is used for the data acquisition and hardware control. The experiment and stand-alone instruments are controlled remotely through a GPIB board. All data coming from Teslatron's sensors and instrument control parameters are processed on a PC through a GPIB bus.

Specifically for the SSTF, a LabView application was written to monitor the process of the measurement and store data.

6.3 SAMPLE PREPARATION

As described in chapter 3, the composite strand needs to be heat treated at high temperature in order to form the superconducting phase.

The same sample holder is used for both the heat treatment and measurement. This approach is the result of extensive investigations performed within the International Thermonuclear Experimental Reactor (ITER) project [34] leading to reduce to the minimum the possibility to overstress the sample during the preparation steps. The holder is a Ti-6Al-4V alloy grooved cylindrical barrel with an outer diameter of 32 mm. The Ti-alloy is chosen because it is inexpensive, nonmagnetic, has a low thermal expansion, a high electrical resistivity ($147 \mu\Omega\cdot\text{cm}$ at 4 K) and a low resistivity ratio. The sample is wound on the barrel and held in place by two removable end rings. The end rings are held to the barrel by stainless steel spring clips, which fit through mating holes. Stainless steel wire is used to tie the strand to each end ring. Extra strand is left to account for tin leakage during heat treatment. A coil sample ready for reaction is shown in Fig. 6.4.

Several samples can be heat treated together by mounting them on the stainless steel supports shown in Fig. 6.5. The supports, shown in Fig. 6.6, are inserted in a 1-meter long tube furnace purged with argon inert atmosphere, described in section 5.3.2. After the heat treatment the Ti-alloy end rings are disassembled and replaced by Cu rings. The sample is then ready to be mounted on a probe to perform the critical current measurements.

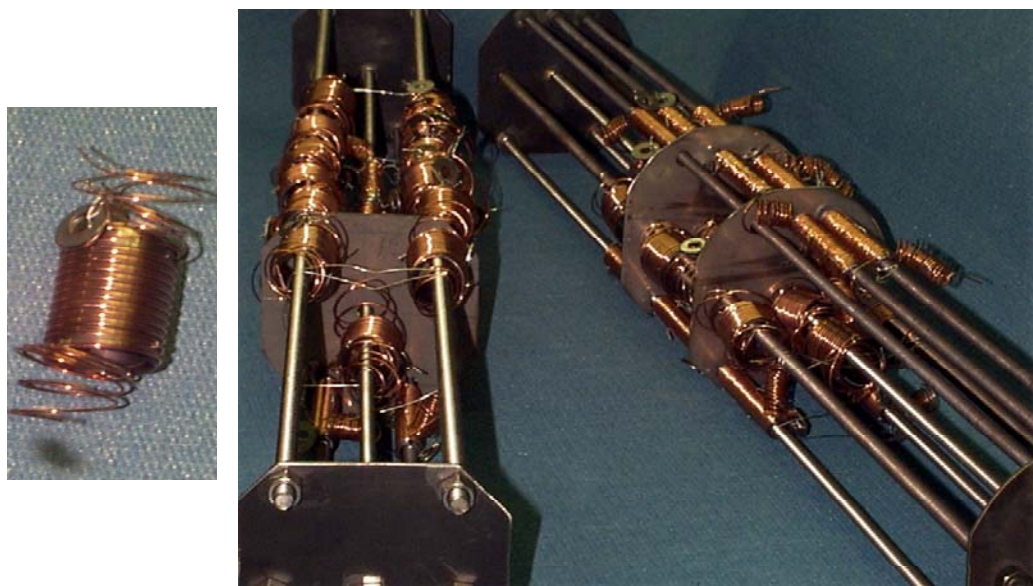


Figure 6.4: Coil sample ready for reaction. **Figure 6.5:** Stainless steel supports for sample heat treatment.



Figure 6.6: Tube furnaces connected with an argon pressure vessel to provide an inert atmosphere during heat treatment.

6.4 PROBE FOR CRITICAL CURRENT MEASUREMENTS

In order to perform the critical current measurements the sample with the two Cu rings is fixed at the bottom of a probe. The probe is designed to let the sample reach the measurement position in the middle of the solenoid magnet of the Teslatron and to provide the necessary current in order to perform the measurement. Figure 6.7 shows the current path from the leads to the sample. The current is supplied to the sample by pressure contact between the copper rings and two copper lugs welded on the probe (2 and 3 shown in Figure 6.7). A thin layer of Indium is used to improve the electrical contact between them. The sample mounted in the probe is shown on Figure 6.8. Four voltage taps, shown in Figure 6.9, are soldered to the sample and two to the leads in order to acquire voltage during measurement.

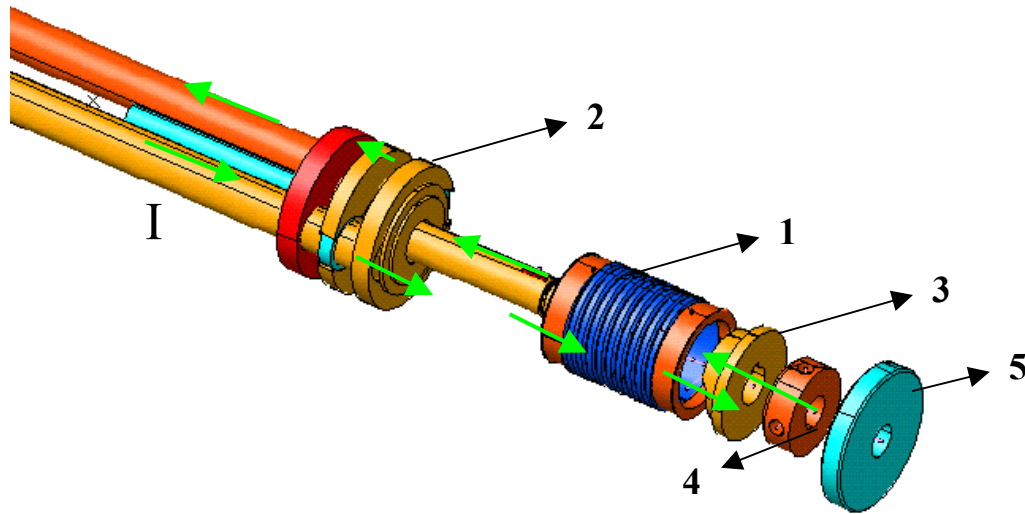


Figure 6.7: Cylindrical fixture. Current is supplied to a sample (not shown in Figure) wound on the barrel (1) by pressure contact of the copper lugs (2 and 3) onto the barrel copper rings. Pressure is applied by means of a brass nut (4). The G-10 disc (5) is used for centering the probe within the magnet bore.

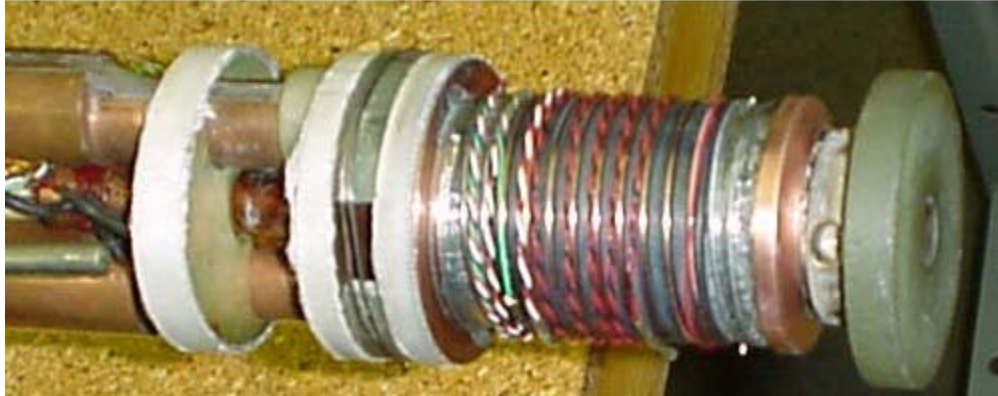


Figure 6.8: Coil configuration.

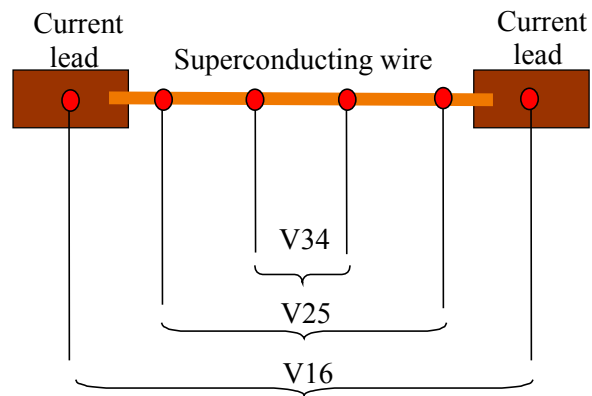


Figure 6.9: Voltage taps.

6.5 EXPERIMENTAL EVALUATION OF I_c AND J_c

The I_c measurements are performed ramping the current in the sample and reading the voltage between the taps until the superconductor reaches the transition to the resistive state. Then the V - I curve, shown in Figure 6.10, is plotted.

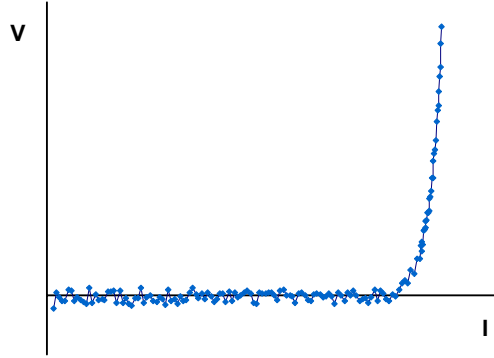


Figure 6.10 V - I curve.

Two different methods are commonly accepted to evaluate I_c from the experimental data:

- the critical field criterion
- the resistivity criterion.

In the first case a conventional electric field value of 10 V/m allows to establish the voltage drop in a superconductor at the transition as:

$$V_c = lE_c, \quad (6.1)$$

where l is the superconductor length, E_c is the reference value of the electric field and V_c is the voltage at the transition. This voltage is then compared to the experimental V - I curve in order to evaluate the critical current value for the superconductor.

In the second case a resistivity of $10^{-14} \, \Omega\text{m}$ in the superconductor is used to define the transition voltage as:

$$V_c = I_s \rho_c \frac{l}{S}, \quad (6.2)$$

where ρ_c is the reference value of resistivity (Ωm) and S is the superconducting strand cross section.

The second method is preferred since given the actual performances of the strands up to 15 T it is more conservative. Nevertheless a problem due to the identification of the area to be used in equation 6.2 is introduced. Cutting every strand and measuring with a microscope the effective Nb_3Sn area is the correct procedure, but it is not applicable. Hence the whole strand cross section is conventionally used.

When calculating the critical current density the same question about the area to be considered is introduced. Conventionally the non-copper (superconductor and bronze) is used to infer J_c from the critical current measurement.

6.6 n-VALUE AND RESIDUAL RESISTIVITY RATIO

Critical current is not the only parameter that can be measured from the experimental V-I curve. The n -value and residual resistance ratio (RRR) can also be calculated with the same setup.

6.6.1 n-Value

The first stages at the transition to the resistive state of a superconductor can be expressed by a power law relationship between current and voltage:

$$V \propto I^n, \quad (6.3)$$

where n is an index of the curve sharpness. A homogeneous strand have a sharper transition since all the filaments reach at the same time the critical limit for the current. Hence the n -value is a good parameter for the strand quality. For fixed temperature and magnetic field, the n -value can be calculated as the slope of the V-I curve during transition in a bilogarithmic chart.

Typical n -values for a high quality superconducting strands vary in a range between 20 and 60.

6.6.2 RRR

The RRR is defined as the ratio of a conductor resistivity between room and critical temperature:

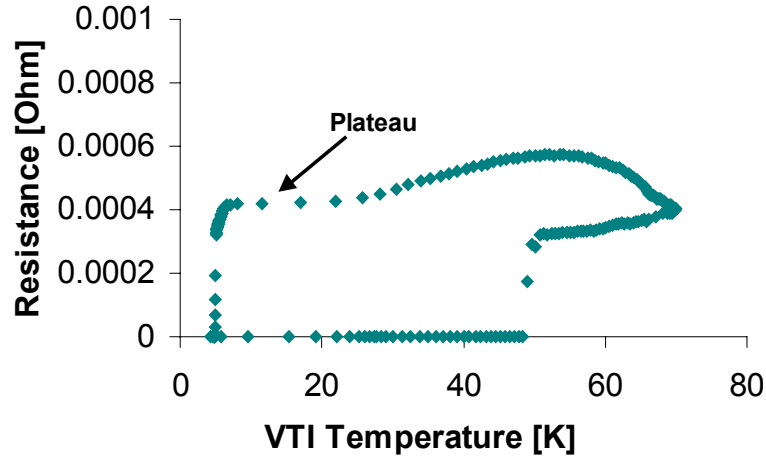


Figure 6.11. RRR Evaluation.

$$RRR = \frac{\rho_{293K}}{\rho_{T_c}} . \quad (6.4)$$

In a superconducting strand this ratio is a parameter for the contamination of the stabilizing copper during the production process and heat treatments. The larger is RRR , the purer is the copper and the more stable is the superconductor.

In superconducting strands OHFC copper with a standard resistivity at room temperature of $1.8 \cdot 10^{-8} \Omega m$ is used.

The resistivity at low temperature is measured heating the sample up to the critical value. During this process the resistance first increases sharply and then reaches a plateau. The low temperature resistivity is inferred from the resistance value at this plateau. Typical values of RRR for superconducting strand are in a range between 50 and 500.

6.7 B_{c20} EVALUATION

In the range of interest, the critical current density J_c for Nb₃Sn can be expressed as a function of: temperature, magnetic field and strain (ϵ) by Summers parameterization [48]:

$$J_c(B, T, \epsilon) = \frac{C(\epsilon)}{\sqrt{B}} \left[1 - \frac{B}{B_{c2}(T, \epsilon)} \right]^2 \left[1 - \left(\frac{T}{T_{c0}(\epsilon)} \right)^2 \right]. \quad (6.5)$$

Where the following simplified expression is used for the upper critical field $B_{c2}(T, \epsilon)$:

$$\frac{B_{c2}(T, \epsilon)}{B_{c20}(\epsilon)} = \left[1 - \left(\frac{T}{T_{c0}(\epsilon)} \right)^2 \right], \quad (6.6)$$

In equations 6.5 and 6.6 $B_{c20}(\epsilon)$ is the upper critical magnetic field at zero temperature and $T_{c0}(\epsilon)$ is the critical temperature at zero field:

$$B_{c20}(\epsilon) = B_{c20m} (1 - a|\epsilon|^{1.7}), \quad (6.7)$$

$$T_{c0}(\epsilon) = T_{c0m} \sqrt[3]{1 - a|\epsilon|^{1.7}}, \quad (6.8)$$

$$C(\epsilon) = C_0 \sqrt{1 - a|\epsilon|^{1.7}}, \quad (6.9)$$

where a is an experimental coefficient dependent on the strain, B_{c20m} is the upper critical field at zero temperature and zero strain, T_{c0m} is the critical temperature at zero field and zero strain, and C_0 is a fitting parameter expressed in $\text{AT}^{1/2} \text{mm}^{-2}$.

B_{c20} is evaluated fitting the I_c data versus magnetic field, using relation 6.5, where the following values have been adopted: $T_{c0m} = 18\text{K}$, and $B_{c20m} = 26 \text{ T}$.

6.8 SUMMARY

A description of the critical current measurement set up and criterion used to evaluate the I_c , RRR and n value has been illustrated in this chapter. The evaluation method for the upper critical field B_{c20} from the I_c data versus magnetic field has also been discussed.

The measurements performed over the superconducting strands are presented in chapter 8 and 9.

CHAPTER

VII

ERROR EVALUATION

7.1 INTRODUCTION

In order to investigate the Nb₃Sn and Cu-Sn intermetallic phases growth kinetics measurements of intermetallic layer thickness versus HT time and temperature are made. Statistical and systematic errors of each measured variable are evaluated in this chapter taking into account the experimental set up, the measurement technique and everything related to the samples manufacturing procedures, described in section 5.

I_c measurements are performed in order to obtain a relation between HT parameters and Nb₃Sn superconducting properties in terms of the layer critical current density (J_{cl}), I_c and B_{c20} . J_{cl} is calculated on the Nb₃Sn measured area; B_{c20} is evaluated fitting the I_c data versus magnetic field. Errors affecting I_c measurements, J_c and B_{c20} values, are evaluated in the last sections of this chapter.

7.2 ERRORS ON THE THICKNESS MEASUREMENT

Since different preparation procedures have been followed, the evaluation of the statistical and systematic errors affecting the layer thickness measurement, is described separately for the Cu-Sn intermetallic phases and for the Nb₃Sn intermetallic compound. A description of the evaluation methods is given and the results obtained are summarized and discussed in the next sections.

7.2.1 Statistical errors on the Cu-Sn phases thickness

Statistical errors affecting the thickness measurement are due to two distinguishable sources: one related to the operator, instrumentation precision and small disturbances and natural fluctuations of the phenomenon, and the other related to the samples manufacturing procedures. Statistical errors due to the first source are evaluated, for each HT, repeating the measurement on four different location of the Cu-Sn models, and on four different Sn pool fore the ITER and MJR strands, as described in section 5.5. The average thickness value (\bar{y}) and its standard deviation (S_s) are calculated. S_s is considered as an estimation of the statistical error due to the first source. The relative error is then calculated. Its

T_s [°C]	ϵ $D_{y_s}\%$	η $D_{y_s}\%$	δ $D_{y_s}\%$
150	(1.8-7.2)	(3.4-11.4)	—
180	(3.4-7.9)	(3.8-9.5)	
210	(1.9-4.8)	(1.5-3.7)	
240	(1.7-5.6)	(9.1-11.4)	—
340	(1.3-8.6)	(8.1-17.3)	
400	(1.1-4.6)	(8.3-12.2)	
440	—	—	(3.4-12.7)
500			(2.2-18.9)
550			(0.6-1.4)

Table 7.1 Range of the relative statistical error estimate ($D_{y_s}\%$), affecting the layer thickness measurement of the three Cu-Sn phases investigated on the Cu-Sn models.

variability range and average value ($D_{y_s}\%$) calculated over all the durations of the heat treatment at each set point temperature, is summarized in Table 7.1 for the

three phases investigated on the Cu-Sn models and on table 7.2 for the ITER and MJR strands.

T_s [°C]	ε $D_{y_s}\%$	η $D_{y_s}\%$
150	—	—
180	—	—
210	(6.1-9.1)	(8.2-13.9)
240	(10.0-29.7)	(13.6-23.6)
340	(4.5-6.3)	(5.1-6.8)
400	(4.5-9.0)	11.5

Table 7.2 Range of the relative statistical error estimate ($D_{y_s}\%$), affecting the thickness measurement of the two Cu-Sn phases investigated on ITER and MJR strands.

Table 7.1 shows that when the η phase develops inside the liquid ($T \geq 240$ °C), $D_{y_s}\%$, is substantially bigger than $D_{y_s}\%$, associated to a solid diffusion.

Comparing Table 7.1 and Table 7.2, it can be observed that the error on ε and η phase thickness measured on the strands is substantially bigger than in the Cu-Sn models.

Errors introduced by the Cu-Sn models manufacturing procedures are evaluated repeating the thickness measurement on four samples independently prepared. The same preparation procedures are followed for all the samples, as described in section 5.

The casting of the Sn in the Cu bar containers is made independently for each of the four Cu bars. Then the Cu bars are heat treated all together in the same furnace, for the same time and at the same temperature. After the heat treatment the samples are cut and polished independently. Then the thickness is measured in four different locations for each sample. This procedure allows to evaluate the statistical errors introduced by: casting, cut and polishing. Because of the large amount of time required to prepare, heat treat, and measure each sample, the evaluation is made at one temperature and one duration of the heat treatment for two different manufacturing procedures used. As described in section 5.2.2 two different casting procedures and two different sample geometry were used during the development of the experiment, leading to the following combinations:

1. Oxy-Acetylene torch casting and cylinder axially drilled geometry (indicated as type A geometry), for the samples heat treated at temperature below 210 °C (investigation of η and ϵ phase in solid-solid diffusion);
2. Oxy-Acetylene torch casting and cylinder transversally drilled geometry (indicated as type B geometry), for the samples heat treated at temperature between 210 °C and 400 °C (investigation of ϵ phase in solid-liquid diffusion);
3. Hot plate casting and cylinder transversally drilled geometry (type B geometry), for the samples heat treated at temperature above 400°C (investigation of δ phase).

Four types A samples prepared with the torch (case 1) are heat treated at 210°C for 48h, and four type B samples prepared with the hot plate (case 3) are heat treated at 340 °C for 24 h. The temperature of 340 °C is chosen, because of the interest in investigating the range of temperature between 240 and 400 °C, as it is discussed in chapter 8. The hot plate is chosen since it will substitute the torch at all temperatures in order to have a better temperature control and heating uniformity, as discussed in section 5.2.2.

The thickness is measured in four different location of each sample. The average value and its standard deviation (\mathbf{s}_r) are calculated over the sixteen measurements. In this case \mathbf{s}_r includes both the effects of the first statistical error sources (\mathbf{s}_s corresponding to: errors of judgment of the operator, instrumentation precision and small disturbances, natural fluctuations of the phenomenon), and the effects of the preparation procedures (\mathbf{s}_p). In order to obtain \mathbf{s}_p , \mathbf{s}_s^2 is subtracted from \mathbf{s}_r^2 , and the square root is calculated. The relative error due to the preparation procedures ($\mathbf{Dy}_p\%$) for the average thickness value is calculated.

To obtain the relative error due to the procedures in case 2 (casting by Oxy-Acetylene torch and type B geometry), the error due to the procedures is considered to be mostly dependent on the sample geometry and casting technique. The sample geometry mostly affects the position of the cutting plane with respect to the plane that contains the axis of the Sn pool container. The cutting plane position does not generate a variability of the sample section in type A geometry,

being the cutting plane perpendicular to the axis of the Sn pool container. For the type B samples, the cutting plane position can lead to a variability of the sample section, being the cutting plane parallel to the axis of the Sn pool container. Due to the small influence of the sample geometry on the cutting surface plane, in type A geometry, it is chosen to attribute the whole error due to the procedures in case 1 ($D_{yp1}\%$), to the casting of the Sn. For case 3 (type B geometry and hot plate casting), it is chosen to distribute the error due to the procedures ($D_{yp3}\%$) in equal parts to the casting and to the sample geometry; this is done also because of the small value of the error, as it will be shown in Table 7.2. Thus the error due to the procedures ($D_{yp2}\%$), in case 2, is calculated summing $D_{yp1}\%$ square to $D_{yp3}\%$ square divided by two. $D_{yp}\%$ is summarized in Table 7.3 for each different procedure.

The overall error affecting y , for each HT, is obtained summing the relative error due to the operator, instrumentation precision, small disturbances and natural fluctuations of the phenomenon to the one due to the preparation procedures.

Case 1: Oxy-Acetylene torch; axially drilled cylinder geometry	Case 2: Oxy-Acetylene torch; transversally drilled cylinder geometry	Case3: Hot plate; transversally drilled cylinder geometry
7.72%	7.82%	1.71%

Table 7.3 Relative error due to the preparation procedures ($D_{yp}\%$), for the different casting procedures and sample geometry used during the development of the experiment

Results show that the casting procedure can strongly affect the thickness measurement, while the sample geometry has a small influence on the error, as deducted if comparing case 1 and case 2. The error due to the casting is smaller if using the hot plate rather than the torch. It has been shown in Figure 5.3 that the Cu-Sn interface after casting is uniform if heating the Cu bar with the hot plate, while may presents voids and is generally not uniform if using the Oxy-Acetylene

torch due to the larger temperature control and heating uniformity allowed by the hot plate in comparison with the Oxy-Acetylene torch. In conclusion the sample production quality can be improved using the hot plate.

7.2.2 Statistical errors on the Nb₃Sn thickness

Statistical errors affecting the thickness measurement (y_i) of the Nb₃Sn compound, are evaluated repeating the measurement in four different Nb filaments. This is done for each sample at each HT, with the measurement technique described in section 5.5. The average value (y), and its standard deviation (s_y) are calculated. Typical values of the relative error $Dy\%$, for PIT strand and IT strand, are shown in Table 7.4.

All the wires used in the experiment belong to the same billet. An evaluation of errors introduced by the manufacturing procedures should be carried on wires belonging to different billets.

T_s [°C]	PIT $Dy\%$	IT $Dy\%$
650	(1.2-1.9)	(2.0-9.3)
700	(0.7-4.7)	(4.3-15.9)
750	(1.2-3.7)	(3.0-11.9)

Table 7.4 Relative statistical error $Dy\%$ range, on the Nb₃Sn layer thickness for PIT and OST strands.

7.2.3 Systematic errors on the Cu-Sn phases thickness

The major sources of systematic errors affecting the thickness measurements are: instruments calibration, operator, and sample preparation procedures.

Since the instruments are periodically calibrated and submitted to maintenance, the accuracy advised by the manufacturing company is considered to be an estimate of the deviation from the operating temperature. Since for each instrument the accuracy is at least three orders of magnitude lower than the operating temperature, no correction is applied to the thickness.

In order to evaluate the systematic error due to the operator in realizing the samples, two samples are prepared by two different people and measured by the same one. The average value of the thickness is calculated for both the samples and compared. The difference between the two average values is smaller by two orders of magnitude than the standard deviation due to the statistical errors. For this reason this error is considered negligible.

To evaluate the systematic error introduced by the operator in measuring the area and the length of the layer the same sample area is measured four times by two different people, (one of them is the same who measures all the thickness values acquired for the experiment) and the difference between the average values are compared. The difference is two orders of magnitude smaller than the standard deviation due to the statistical error. Therefore no correction is considered to be necessary. In conclusion, the sensibility of the measurement to the operator is negligible.

The systematic error on the thickness is considered to be the difference between the value measured after the HT and the one that would form during the HT measured time and temperature, accordingly to the diffusion model adopted. The latter value will be indicated as “true” thickness.

The HT time is measured between the introduction of the sample inside the furnace and the removal from the furnace. The effective time of the diffusion process is different than the measured HT time because of the cooling and heating processes, determined by the heat capacity of the sample.

During the heating and cooling of the sample also the effective temperature is lower than the set value. The HT transients leads thus to a difference between the measured and effective time and temperature of the diffusion process. Hence there is a difference between the measured and true thickness. The systematic error is evaluated in order to correct the thickness measurement. The correction is considered not necessary if the systematic error is at least two orders of magnitude smaller than the statistical error. The relation between the measured and “true” value is evaluated considering the thickness growth versus effective diffusing process time and temperature.

The model adopted to evaluate the thickness growth versus HT time and temperature is the parabolic thickness (y) growth law (the reasons of this choice are given in section 8.2.1):

$$y^2 = kt, \quad (7.1)$$

and

$$k = k_0 \exp(-E / bT). \quad (7.2)$$

where k is the rate of growth, k_0 is the frequency factor, T is the temperature and E the activation energy.

During the transients of the heat treatment, the diffusion process occurs at variable temperature, and k is time dependent:

$$k(T(t)) = k_0 \exp(-E / bT(t)). \quad (7.3)$$

In this case, the layer thickness growth can be expressed by the following relation:

$$y^2 = \left[\int \sqrt{\frac{k(T(t))}{4t}} dt \right]^2. \quad (7.4)$$

The thickness growth versus effective diffusing process time and temperature is illustrated in Figure 7.1. In order to better understand the figure it may help to remember that, as described in section 5.2.3, the samples are cut from a Cu bar that is heat treated at fixed T_s in several steps. After each heat treatment step, the Cu bar is cooled, a sample is cut, then the bar is inserted again inside the furnace and heat treated for the remaining time to complete the second heat treatment duration. This cycle ends when the last duration of the heat treatment (given by the sum of previous steps duration and the last one) is achieved. Each step of the

heat treatment is indicated with a superscript index. This process is shown in Figure 7.1 where a two steps heat treatment is considered.

At $t=0$ the sample at room temperature is inserted in the preheated furnace at the set point temperature (T_s); starting at this moment the layer thickness growth rate is $k_s(T(t))$, (the index s refers to the heating process).

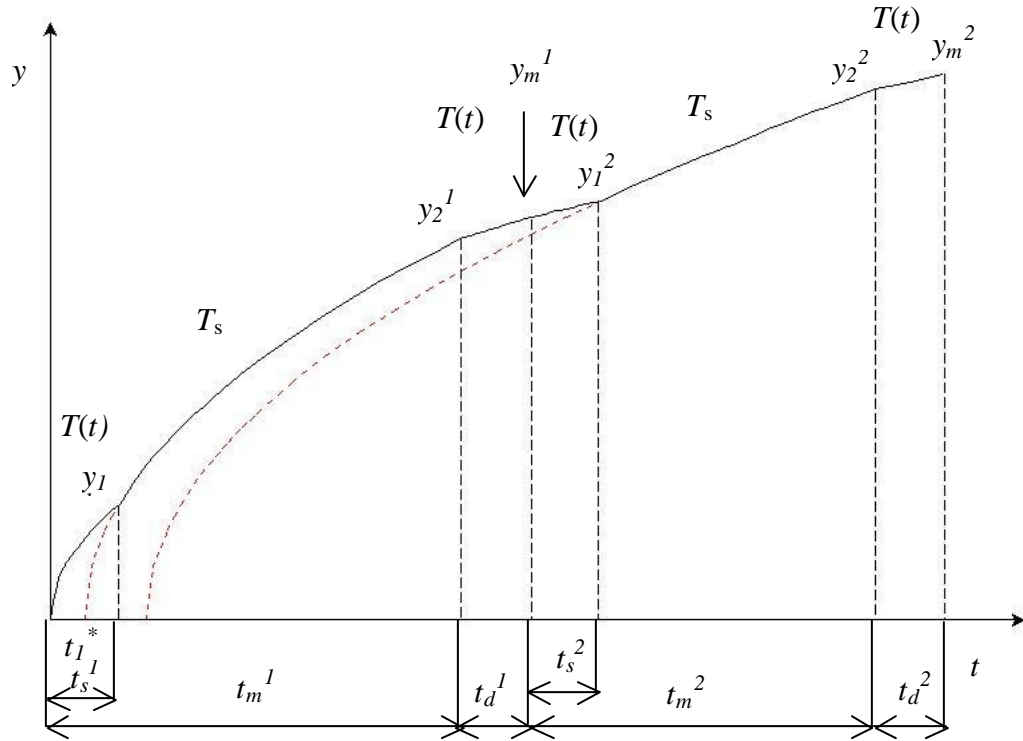


Figure 7.1 Thickness (y) growth versus heat treatment time (t) and temperature (T).

T_s is the set point temperature; $T(t)$ is the temperature during the cooling and heating process; t_m^n is the measured time; t_s^n and t_d^n are respectively the duration of the heating and cooling processes; the index n refers to the step n of the heat treatment.

At t_s^1 the sample reaches T_s . The thickness formed at t_s^1 is indicated as y_l^1 . Starting at t_s^1 , till the time that the sample is removed from the furnace (t_m^1), the sample undergoes a diffusion process at T_s ; the growth rate ($k(T_s)$) is constant, and the thickness formed at t_m^1 is indicated as y_2^1 . At t_m^1 the sample starts cooling from T_s to room temperature. The cooling duration is indicated as t_d^1 . During t_d^1 , the layer thickness growth rate is $k_d(T(t))$, (the index d refers to the cooling process). The thickness at $t_m^1 + t_d^1$ (y_m^1) is the measured value.

The thickness “true” value (y_v^I) corresponds to a diffusion process that occurs at T_s for a duration equal to the measured time t_m^I :

$$(y_v^I)^2 = k(T_s)t_m^I, \quad (7.5)$$

In order to find a relation between the true and the measured thickness value the following scheme is considered: each time that the growth rate changes from a constant to a temperature dependent value, or the contrary, it can be assumed that the layer thickness, at that time, formed with the following growth rate starting from a different time. For example y_I^I forms during the heating at variable temperature with a growth rate equal to $k_s(T(t))$ from $t = 0$ till t_s^I and is given by the following expression:

$$(y_I^I)^2 = \left[\int_0^{t_s^I} \sqrt{\frac{k_s^I(T(t))}{4t}} dt \right]^2. \quad (7.6)$$

It can be assumed that y_I^I forms at the set point temperature with a growth rate equal to $k(T_s)$ from a time indicated in figure as t_I^{*I} till t_s^I :

$$(y_I^I)^2 = k(T_s)(t_s^I - t_I^{*I}). \quad (7.7)$$

t_I^{*I} can be calculated by equations 7.6 and 7.7.

The thickness y_I^I at t_m^I can be expressed by substituting t_m^I to t_s^I in expression 7.7.

Applying the same considerations and calculations for the time $t_m^I + t_d^I$, and considering the expression 7.5 it can be obtained the relation between the measured layer thickness y_m^I and the true value layer thickness y_v^I . The same considerations are applied to the following heat treatment steps in order to obtain the relation between the measured and true thickness value after a sequence of n heat treatments, which will be indicated as y_m^n and y_v^n . The relation obtained is:

$$(y_m^n)^2 = (y_v^n)^2 + \sum_{i=1}^n \left[\int_0^{t_d^i} \sqrt{\frac{k_d^i(T(t))}{4t}} dt \right]^2 - \sum_{i=1}^n \left[t_s^i k(T_s) - \left[\int_0^{t_s^i} \sqrt{\frac{k_s^i(T(t))}{4t}} dt \right]^2 \right] \quad (7.8)$$

where the true thickness value is expressed by the following equation:

$$(y_v^n)^2 = k(T_s) \sum_{i=1}^n t_m^i, \quad (7.9)$$

and where: t_m^i is the measured duration of the i HT step, t_s^i and t_d^i are the duration of the heating time and the cooling time for the i heat treatment step and $k_d^i(t)$ and $k_s^i(t)$ are the growth rate during t_d^i and t_s^i .

Thus it is possible to correct the expression of the measured value by evaluating the two sums that compare in expression 7.8. For this purpose the temperature evolution, during the cooling process, is evaluated. To simulate the worst condition (that leads to the biggest difference between the true and measured thickness), the Cu bar used to evaluate the cooling curve is the one corresponding to the first step of the heat treatment (that has a bigger volume and mass hence a bigger heat capacity). Hence, the heat capacity of the Cu bar decreases after each HT step, since a slice is cut between each step, thus the temperature versus time drops with a faster rate during the following cooling process step. This leads to a shorter cooling time and to a faster decrease of the layer thickness growth rate, resulting in a decrease of the thickness that forms during the following cooling processes. For our evaluations all the cooling curves are considered equal to the one corresponding to the first heat treatment step, for which more growth is expected. This leads to overestimate the difference between the measured and true value of the thickness. The same consideration can be applied to the heating process.

To evaluate the temperature evolution during the cooling process, the Cu bar is heat treated at the maximum T_s investigated (550 °C). After the Cu bar is removed

from the furnace, its temperature is measured by placing a thermocouple between the interface of a graphite groove and the sample. The temperature readings are made with a frequency of one minute. Fitting the temperature data versus time, the following exponential dependence is obtained:

$$T - T_r = (T_s - T_r) \exp(-0.0007t), \quad (7.10)$$

where T_r is the room temperature.

Thus the time dependence of the thickness growth rate during the first cooling process of the sample is obtained:

$$k_d^{-1}(T(t)) = k_0 \exp(-E / b(T_s - T_r) \exp(-0.0007t)) . \quad (7.11)$$

The heating curve is assumed equal to the cooling curve, thus the duration and the rate of growth of the heating process are considered to be equal to the one of the cooling process.

Considering all the hypothesis made above, the relation between the true and measured value of the thickness (equation 7.8) can be expressed, for each step n of the HT, as:

$$(y_m^n)^2 = (y_v^n)^2 + n \left[\int_0^{t_d^1} \sqrt{\frac{k_d(T(t))}{4t}} dt \right]^2 - n t_s^{-1} k(T_s) + n \left[\int_0^{t_s^1} \sqrt{\frac{k_s(T(t))}{4t}} dt \right]^2 . \quad (7.12)$$

In evaluating the layer growth during the transients of the heat treatment, it has to be considered that the diffusion process becomes negligible for temperatures lower than the minimum value between the inferior temperature limit of existence of the phase or 373 K. The value of this temperature is indicated as T_l . The time at which the sample reaches T_l is indicated as t_l^I . During the heating process $k_s(T(t))$ is zero for times inferior to t_l^I , while during the cooling $k_d(T(t))$ is zero for times superior than t_l^I . The value of t_l^I is evaluated using the following dependence:

$$t_l^{-1} = \frac{\ln(T_0) - \ln(T_l)}{0.0007} , \quad (7.13)$$

where $T_r = 20\text{ }^{\circ}\text{C}$, $T_l = T_d - T_r$ and $T_0 = T_s - T_r$,

The values of the diffusion frequency k_0 and of the activation energy E used to evaluate the integrals of expression 7.12, are the ones obtained by fitting the layer thickness, time and temperature data, as shown in section 8.2.4.

An estimate of the systematic relative error ($Dy_m^n\%$), calculated as the difference between the true and measured value divided by the measured values, is shown in Table 7.5 for the first heat treatment step ($n = 1$). For the first HT step the difference between the true and measured thickness resulted to be the biggest one. Table 7.5 shows also the values of T_s , T_d , for the three Cu-Sn phases investigated.

	$T_s\text{ [}^{\circ}\text{C]}$	$T_d\text{ [}^{\circ}\text{C]}$	$Dy_m^n\%$
h	150	100	$3.3 \cdot 10^{-13}$
	180		$1.5 \cdot 10^{-13}$
	210		$3.0 \cdot 10^{-11}$
e	150	100	$2.7 \cdot 10^{-11}$
	180		$6.5 \cdot 10^{-9}$
	210		$4.7 \cdot 10^{-7}$
	240		$2.3 \cdot 10^{-8}$
	340		$3.3 \cdot 10^{-4}$
	400		$4.0 \cdot 10^{-3}$
d	440	350	$5.0 \cdot 10^{-5}$
	500		$1.7 \cdot 10^{-5}$
	550		$6.5 \cdot 10^{-2}$

Table 7.5 Systematic relative error $Dy_m^n\%$ for the first HT step ($n = 1$), (for which $Dy_m^n\%$ resulted to be the biggest) at the set temperature T_s , for the three Cu-Sn phases investigated (η , ε , δ). T_d is the minimum value between the inferior existence limit of the phase and 100°C .

$D_{ym}^n\%$ is compared with the overall statistical error (obtained combining $D_{ys}^n\%$ and $D_{yp}^n\%$, which values are given in Tables 7.1 and 7.3. The bigger ratio between the two values, obtained for first step of the heat treatment at 550 °C, is about 0.03.

All the other systematic-statistic error ratios vary between 10^{-3} and 10^{-13} . Thus the heat treatment transients do not introduce a consistent error over the measured thickness, and no correction is applied.

7.2.4 Systematic errors on the Nb₃Sn thickness

The sources of systematic errors affecting the Nb₃Sn layer thickness measurements, are similar to the ones affecting the Cu-Sn layer thickness, described in the previous section. As for the Cu-Sn system the operator and instrument errors are negligible since the same set up is used .

The evaluation of the error introduced by the heating and cooling transients of the heat treatment procedure, is based on the same considerations made for the Cu-Sn samples. The same definition of systematic error, the same diffusion model and the same criterion to correct the thickness measurement are used.

Some adjustments have however to be made, because of the different mechanism of the transients processes, and because of the smaller heat capacity of the samples (wires in this case, see chapter 5). The sample is inserted inside the furnace chamber when this is at room temperature; the heating process of the furnace is controlled with a ramp rate of 2.5 °C/min; the same ramp rate controls the cooling process. Since the wires have a low heat capacity, their heating and cooling processes are considered to follow, with no delay, the one of the furnace chamber. Since the cooling and heating processes have the same duration and ramp rate, the rate of growth at variable temperature, during the heating and cooling process, is assumed to be the same.

The HT duration for each step (t_{ms}^n), is measured between the moment at which the furnace chamber reaches T_s and the moment at which it starts cooling down. Referring to Figure 7.1, the measured time, in this case, is equal to:

$$t_{ms}^n = t_m^n - t_s^n, \quad (7.14)$$

The Nb₃Sn layer growth versus HT time is described by the following equation (the reasons will be given in chapter 9):

$$y^n = kt. \quad (7.15)$$

The true value of the layer thickness, after the n steps of the heat treatment is:

$$(y_{vs}^h)^n = k(T_s) \sum_{i=1}^h t_{ms}^i, \quad (7.16)$$

where h is the HT step at a fixed temperature T_s .

In this case, the Nb₃Sn thickness formed after a single ramp up-ramp down heat treatment has been measured for all the T_s investigated. The thickness formed after each cycle, resulted to be negligible for the IT strand, while a consistent layer formed in PIT strands. Therefore, while no correction is applied for the IT strand, a correction is made for the PIT strands.

The Nb₃Sn thickness, formed in PIT strand after the single ramp up-ramp down heat treatment, is measured on four different Nb filaments; the average value is indicated as y_e . The relation between the true and measured thickness is calculated with the same method used for the Cu-Sn system considering the two equations 7.16 and 7.14 and using the growth law expressed by equation 7.15. The result is:

$$y_{vs}^h = \sqrt[n]{(y_{ms}^h)^2 - ny_e^2}, \quad (7.17)$$

As a first approximation to evaluate y_{vs}^h the exponent n has been considered equal to 2; then the y_{vs}^h data have been fitted using relation 7.15 by plotting $\ln(y_{vs}^h)$ as a function of $\ln(t)$ (that gives a straight line which slope is n) to evaluate n . Then

y_{vs}^h has been evaluated a second time using the value obtained for n . The y_{vs}^h data have been then fitted a second time using relation 7.15 to find a second estimate for the exponent n . This iterating calculation lasts till the value obtained for n differs by less than 0.1 from the previous.

The values of y_{ms} (corresponding to the last estimate) and y_e are shown in Table 7.6 for the different HT durations, *i.e* for each HT step n , at a fixed temperature T_s . The correction is applied to the PIT strands thickness in order to calculate the Nb₃Sn growth rate.

T_s [°C]	y_{ms}^n [μm]	y_{ms}^n [μm]	y_e [μm]
650	4.2; 7.6; 9.4; 10.4	3.8; 7.2; 9; 10	2
700	5.7; 7.7; 9.1; 10.4; 12.5	5.5; 7.6; 9; 10.3; 12.4	3.4
750	6.4; 7.6; 9.9; 12.4; 12.5	5.9; 6.8; 9.4; 11.9; 12	4.5

Table 7.6 Measured (y_{ms}^n) and “true” (y_{vs}^n) thickness value at the set temperature T_s for all the HT steps n and measured thickness (y_e) after a ramp up- ramp down heat treatment to T_s .

7.3 ERRORS ON TEMPERATURE

Since the furnace sensors are periodically calibrated, the error on the temperature during the heat treatment is considered to be equal to the value indicated on the vendor manual (precision: 5 °C). Since the accuracy (0.5 °C) is smaller by one order of magnitude with respect to the precision a systematic correction is not applied to the temperature.

7.4 ERRORS ON TIME

Time is measured, between when introducing the sample into the furnace and when removing it from the furnace. The instrument used to measure the HT time

has a sensibility of one second. Since the duration scale of each heat treatment is in the range of hours, the uncertainty of one second is considered negligible.

7.5 ERRORS ON I_c AND J_c

Errors on I_c are evaluated by using the parameterization described in section 6.7, where $B_{c2m} = 26$ T, $T_{c2m} = 18$ K, $C_0 = 26616 \text{ AT}^{1/2}\text{mm}^{-2}$ and $a = 900$. Here a brief description of the parameters that mostly affect the measurement and a summary of the results is given, while a full description is discussed in other documents [49].

The error on I_c is evaluated taking into account its sensitivity to: temperature, magnetic field and strain. The effects of the voltage noise and the readback accuracy of the power supply are also evaluated. The variation of T and B during the measurement are respectively 16 mK and 0.27% the nominal B value. The sensitivity of I_c to these variations depends on the magnetic field and on the strain. Since the influence of the strain is small [49], the error due to the T and B variation is evaluated assuming a zero strain.

B [T]	$DI_{c,BT}\%$
4	0.24
6	0.32
8	0.40
10	0.51
12	0.73
13	0.77
14	0.88
15	1.00

Table 7.7 Relative error on I_c ($DI_{c,BT}\%$) due to the temperature and magnetic field variation at various magnetic fields (B).

The overall statistical relative error ($DI_{c,BT}\%$) due to the variation of B and T is summarized in Table 7.7, for different magnetic fields.

The noise on the voltage is strongly dependent on the n value and on the current.

Since the n value measured on PIT strands is greater than the one measured on IT strands, independent investigations have been performed. Moreover the readback accuracy of the power supply is dependent on the current. The relative error due to the noise and the power supply, indicated respectively as $DI_{c,N}\%$ and $DI_{c,PS}\%$, are shown for different range of current, in Table 7.8.

I [A] Range	$DI_{c,PS}\%$	$DI_{c,N}\%$	
		IT	PIT
0-100	1.14	3.24	1.41
100-200	0.71	1.92	0.89
200-300	0.55	1.52	0.71
300-400	0.55	1.30	0.55
400-500	0.45	1.14	0.55
500-600	0.45	1.05	0.45
600-700	0.45	0.95	0.45
700-800	0.45	0.89	0.32
800-900	0.45	0.85	0.32
900-1000	0.45	0.77	0.32

Table 7.8 Relative error on I_c due to the to the noise ($DI_{c,N}\%$) for PIT and IT strands and due to the power supply ($DI_{c,PS}\%$) for different current ranges.

The overall statistic error is the result of the composition of the relative contributes at each magnetic field and for each range of current for PIT and IT strands.

I_c measurements are also affected by a systematic error due to the sample self field and strain. The self field generated by the sample coil, induces a shift

between the external field (measured) and the real field seen by the sample. Since the self field is always opposite to the external one the value of I_c is always overestimated. For a current of 1000 A the self field is about 0.3 T; this would modify I_c of about +6% at 12 T.

During the measurement the Lorentz force (the relative direction of the external magnetic field and of the transport current are chosen such to have an inward Lorentz force) and the differential thermal contraction of the Nb₃Sn strand with respect to the Ti-alloy barrel, generate compressive stress on the sample. This condition allows the strand to reach higher I_c values. At 12 T, I_c is increased by 3%, assuming an intrinsic compressive strain of 0.25%, and by 5% assuming an intrinsic compressive strain of about 0.4%.

The error on J_c is calculated by combining the relative statistical errors on I_c and on the Nb₃Sn area.

The error on the Nb₃Sn area is evaluated with the same procedure used for the Nb₃Sn thickness, described in section 7.2.2.

7.6 ERRORS ON B_{c20}

As described in section 6.7 B_{c20} is evaluated fitting the I_c data versus magnetic field using the Summers parameterization [48] assuming: zero strain, $T_{c2m} = 18$ K, $T_c = 4.2$ K and $a = 900$.

Referring to reference [49] an estimate of the effects of the strain (ϵ) and of the self field (see previous section) on B_{c20} is evaluated for a PIT strand. The B_{c20} has been evaluated taking into account a zero, +0.2% and -0.2% strain to obtain an estimate of the strain effect. Then the magnetic field has been corrected for the self field effect and the B_{c20} has been evaluated for zero, +0.2% and -0.2% strain.

Results are shown in Table 7.9, where B_{c20SF} is the value obtained with the self field correction.

PIT	$e = 0$	$e = -0.2\%$	$e = +0.2\%$
B_{c20} [T]	25	25.7	26.0
B_{c20SF} [T]	25.1	25.8	26.1

Figure 7.9 B_{c20} values calculated for different strain (e) and calculated taking into account the self field effect corrections on the magnetic field (B_{c20SF}).

The estimate of the maximum error considering both the self field and the strain effects is $+1.1\text{T} - 0\text{T}$.

An evaluation of the statistical error has been made considering the effect of the I_c error [49]

The results of the evaluation are shown in Table 7.10.

$DB_{c20}\%$ IT	$DB_{c20}\%$ PIT
+(1.7-10.0)	+(1.7-1.4)
-(0-9.0)	-(0.7-0.9)

Figure 7.10 Typical variability range of the statistical error on B_{c20} .

The larger error on B_{c20} for IT strands than for the PIT strand reflects the larger error on I_c for OST strand than for PIT, mostly due to the voltage noise.

7.7 SUMMARY

An evaluation process and the estimate of the statistical and systematic errors affecting each measured variable has been discussed and presented in this chapter.

It has been observed that the most relevant source of error affecting the layer thickness measurement of the Cu-Sn phases is due to the natural fluctuations of the phenomenon, the operator and the instrumentation precision. This error ranges between 2% - 10%, besides a few exceptions.

This is true when limiting the contribution of the samples preparation procedures. It has been observed that a significant improvement on the experimental set up leaded to lower the error due to the samples preparation procedures from 7.8% to 1.7%. This result has been achieved modifying the casting technique. This step results to be one of the major sources of error on the Cu-Sn phases thickness if such condition as the temperature control and heating uniformity are not allowed. It has also been observed that the error on the Cu-Sn phases thickness for the strands is bigger than for the Cu-Sn models.

As for the systematic error introduced by the transients of the HT procedure, this is resulted to be absolutely negligible for the Cu-Sn models if compared with the statistical error.

Similar results are obtained for the systematic and statistical error (due to the natural fluctuations of the phenomenon, the operator and the instrumentation precision) affecting the Nb₃Sn layer thickness measurement in the IT strand.

A different result has been obtained for the Nb₃Sn thickness formed in the PIT strand. In this case the systematic error results to be the biggest source of error since a consistent layer forms during the HT transients.

As for the statistical error affecting the I_c measurement this is less than 1% for the PIT strand. The contribution of the different sources (temperature, magnetic field, readback accuracy of the power supply and the noise of the V curve) is similar for the PIT at each magnetic field and current range.

While for the IT strand the contribution of the voltage noise is the most relevant source for low current values. In this latter case error of 3% can be reached.

The bigger statistical error affecting the I_c for the IT strand leads also to a bigger error on the B_{c20} .

VIII

RESULTS ON THE Cu-Sn SYSTEM

8.1 INTRODUCTION

Nb_3Sn is currently the material most commonly foreseen for the development of high field superconducting magnets. As described in section 3.5, this is realized by either the “Wind and React” technique, usually used for compact magnets like accelerator magnets, or by the “React and Wind” technique, more common on large scale magnets. In both cases, a thorough understanding of the Cu-Sn system diffusion process and phase growth is necessary to optimize the Nb_3Sn reaction cycle [50]. As discussed in section 3.4, the reaction cycle of the composites wires is performed at low temperature to diffuse the Sn in the Cu matrix and at high temperature to form the Nb_3Sn compound. Attention during these stages has to be paid to both the superconducting performance and to the prevention of thermally induced damage on the final produced conductor.

The growth kinetics of the η , ϵ and δ phases of the Cu-Sn phase diagram is investigated as a function of HT time and temperature both over Cu-Sn models

and over ITER and MJR strands. Activation energies and rate of growth are evaluated.

The feasibility of winding partly reacted cables to reduce the magnet manufacturing time and cost is also explored [51]. Nb₃Sn strands have been partially reacted to convert the Sn into the η and ϵ phases of the Cu-Sn phase diagram, and then plastically strained to figure out a cabling and/or a winding degradation. Hence the J_c of Nb₃Sn superconducting strands can be reduced after the cabling and winding processes [52, 53, 54] due to the extreme strain sensitivity of Nb₃Sn. After completion of the reaction cycle, the critical current is measured and compared with that obtained with an uninterrupted HT cycle.

8.2 Cu-Sn PHASE GROWTH KINETICS INVESTIGATION OVER THE Cu-Sn MODELS

Intermetallic diffusion has been widely studied, especially in relation with welding operations [40]. From a theoretical point of view, however, a clear understanding of all the parameters involved in intermetallic diffusion process is still not clear, and parameters like the diffusion frequency (k_0) and activation energy (E) assume the meaning of empirical parameters, as discussed in chapter 4. Their value is nevertheless useful, from a technical point of view, to find a relation between HT time and temperature and the amount of intermetallic compound. The k_0 and E evaluation process and the discussion of the phenomenon observed are presented in the next sections.

8.2.1 Diffusion model

The diffusion model adopted to describe the layer thickness growth versus time is the parabolic growth law, discussed in section 4.2:

$$y^2 = k(T)t , \quad (8.1)$$

The assumption is realistic if the concentration of the diffusing component at the interlayer boundaries and the concentration gradient along the interlayer are constant, as discussed in section 4.2. In this experiment, the two conditions are satisfied because of the narrow composition range of the η , ϵ and δ phase, see section 4.6, and because the design of the Cu-Sn models allows a constant composition of the matrix (pure Sn and pure Cu) at the interfaces of Cu-Sn intermetallics in solid diffusion, as discussed in section 5.2.1.

The latent period t_0 (see section 4.2) is not included in the model because its value, of the order of some second fractions for similar systems [40], is negligible if compared to the time scale of the experiment (order of hours).

The exponential dependence for the rate of growth with the temperature, discussed in section 4.2, is adopted:

$$k = k_0 \exp(-E / kT), \quad (8.2)$$

where k_0 is the diffusion frequency, T is the temperature, β the Boltzman constant and E the activation energy.

Substituting expression 8.2 in equation 8.1, the layer thickness is expressed in function of the HT time and temperature:

$$y^2 = k_0 (\exp(-E / \beta T)) t, \quad (8.3)$$

By measuring the thickness of each intermetallic phase in function of the HT time and temperature the k_0 and E values are evaluated using relation 8.3 for each phase when the hypotheses for the applicability of the diffusion model are verified.

8.2.2 Heat Treatments

Attention on this work is focused on three Cu-Sn phases that forms at relatively low temperature: Cu_6Sn_5 (η phase), Cu_3Sn (ϵ phase), and $\text{Cu}_{41}\text{Sn}_{11}$ (δ

phase), see section 4.6. Limits on the temperature are due to the “Wind and React” approach, as discussed in section 3.5.

Heat treatments of different duration (t) are performed over the Cu-Sn models, described in section 5.2.1, for different set point temperature (T_s), as showed in table 8.1.

Cu-Sn phase	T_s [°C]	t [h]
η and ϵ	400	3, 6, 12, 24, 48
	340	3, 6, 15 24, 48
	240	3, 6, 12, 24, 78
	210	24, 48, 72, 168
	180	24.5, 48.7, 88, 106.6, 154.8
	150	24, 48, 96, 144, 216
δ	550	5, 24, 48.8, 96.3, 136.5
	500	3, 6.3, 12, 24, 49, 88.5, 129, 179, 217, 273
	440	3, 6, 12, 24, 49.2, 91.2, 136
	400	3, 6, 12, 24, 48

Table 8.1: HT performed over the Cu-Sn models.

8.2.3 Diffusion samples observation

After the HT the Cu-Sn models cross section is observed at the optical microscope. Some examples of the observation are presented and discussed.

Figure 8.1 shows the intermetallic phase growth on two samples. Figure 8.1 a) shows a case of Cu-Sn diffusion at a solid/solid interface after 168 h at 210 °C, while Figure 8.1 b) shows a solid/liquid interface, after 48 h at 400 °C. In both pictures the two intermetallic compounds η and ϵ are present.

Except when the η phase develops inside the liquid tin, the thickness of the intermetallic layers is almost uniform along the interface. When the η intermetallic develops inside the liquid, it forms large crystals as showed from

figure 8.1 b). The η crystals presents inside the Sn form during the cool down of the sample.

It should be noticed that while no amount of voids is observed after 1 week at 210 °C, voids created inside ϵ phase with increasing the ϵ and η phase thickness, as shown form Figure 8.1 b). As discussed in section 4.3, the formation of voids is due to atomic density differences between the Cu-Sn phases (see Table 4.1) and to the diffusion coefficient differences between Cu and Sn.

It should be noticed that at 400 °C after 24 h δ phase did not form even if predicted from the phase diagram (see Figure 4.5).

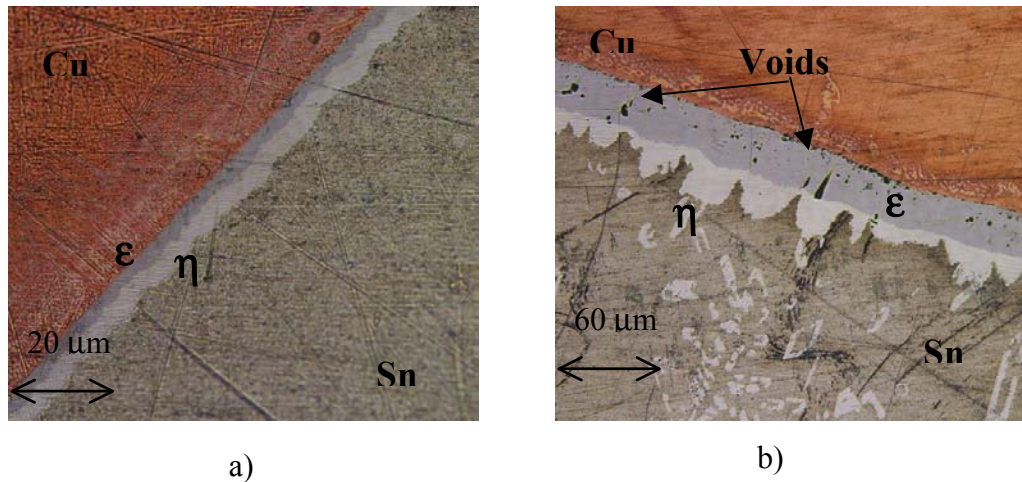


Figure 8.1 Intermetallic growth at the Cu-Sn interface: a) after 7 days at 210°C; b) after 2 days at 400°C.

Figure 8.2 shows the δ and ϵ phase growth at a solid/liquid interface at 500 °C after different HT times. The crystals of η phase present inside the pure Sn and at the ϵ -Sn interface form during the cooling of the sample.

For small HT times the δ phase thickness is uniform along the interfaces and no substantial amount of voids is present.

ϵ phase developing inside the liquid forms large crystals and its thickness is not uniform along the interface.

When increasing the heat treatment duration, voids form and begin migrating to the Cu-rich end of δ phase [55]. At 179 h a crack is present at the δ -Cu interface as illustrated from figure 8.2.b).

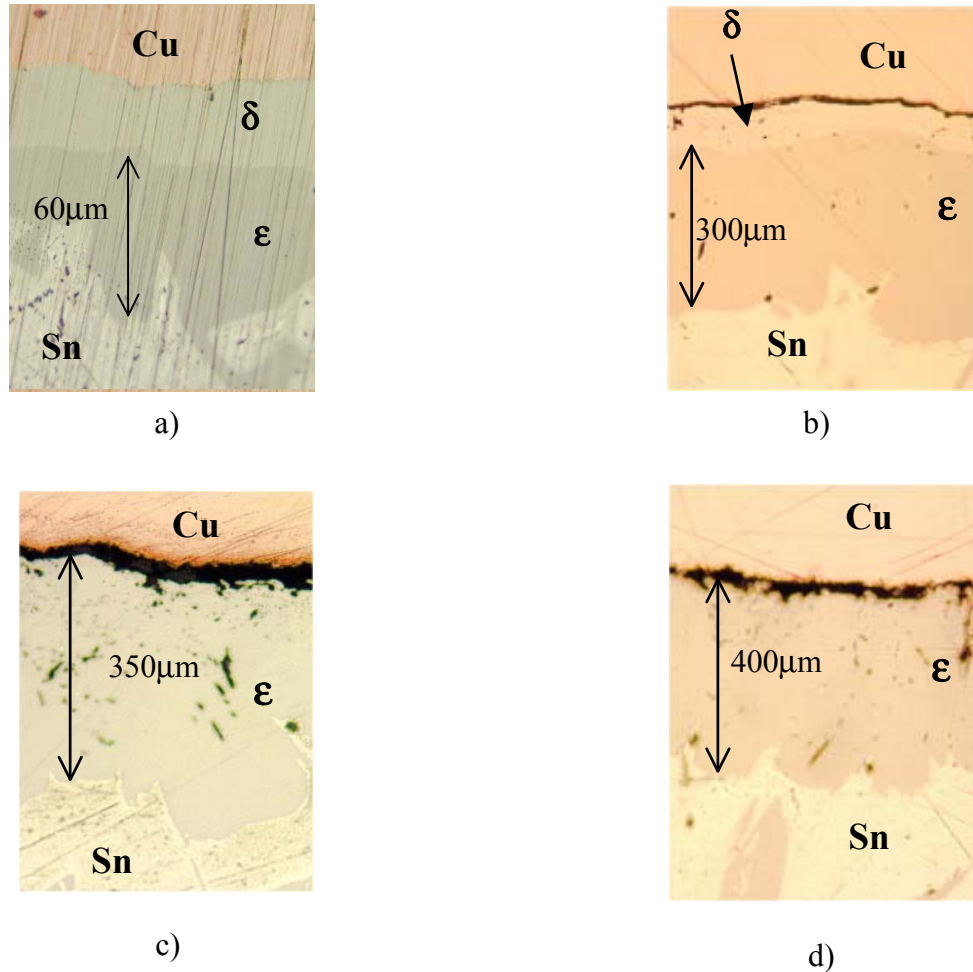


Figure 8.2 Intermetallic growth at the Cu-Sn interface at 500 °C a) after 12 h; b) after 179 h; c) after 217 h; d) after 273 h.

The formation of the crack can be favored by the thermal contraction of the phases during the sample cooling. However the presence of a discontinuity at the Cu- δ interface during the HT is suggest by the experimental evidence that at 179 h the δ phase thickness is smaller than after shorter HT times, as it is shown in Figure 8.3, while the ϵ phase thickness keeps increasing. After 217 h some spots of δ phase, not shown in figure, are still present along the interface, while after

273 h no δ phase is left along the entire interface. The decrease of the δ phase thickness after a certain HT time is observed at all the HT temperatures, as shown in Figure 8.3. This phenomenon is related to the interruption of the diffusion process at the δ -Cu interface. In the system δ - ϵ -Sn the diffusion process, accordingly to Fick's law, proceeds to level out the concentration differences therefore ϵ phase (being the most Sn rich phase) grows at both the two interfaces, while δ phase decreases because it supplies the Cu to the ϵ phase growth.

A comparison between the ϵ and the δ phase growth, shown in Figure 8.3, is performed for all the HT temperatures and times investigated.

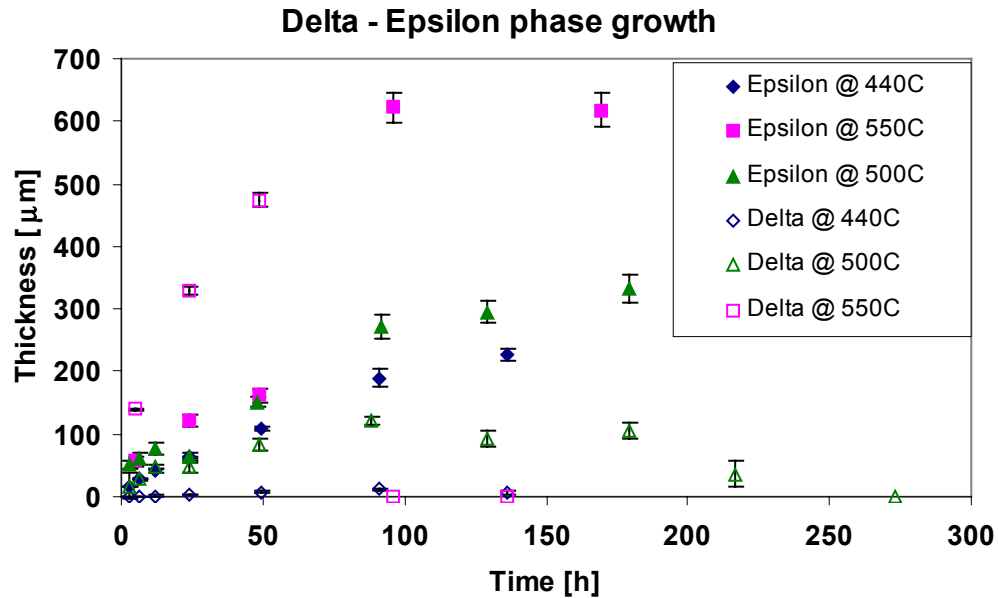


Figure 8.3 Delta and Epsilon phase growth comparison at $T \geq 440$ °C.

The comparison shows that when the δ phase thickness begin decreasing the ϵ phase thickness present a step increase at all the temperatures. This phenomenon occurs for a HT duration that decreases with the temperature, however for all the T_s it happens in the range of 50 - 100 h.

In order to estimate the E and k_0 values of the δ phase, the criterion to use the thickness data before 50 h has been adopted.

8.2.4 Phase growth kinetics and E and k_0 evaluation

The ϵ , η , and δ phase thickness has been measured after each HT with the technique described in section 5.5 and then plotted in function of the HT time and temperature.

Figure 8.4 and figure 8.5 shows respectively the plots of the thickness evolution of η and of ϵ phase as a function of time at 150, 180 and 210°C.

In this range of temperature all the Cu-Sn phases and the pure Sn are solid.

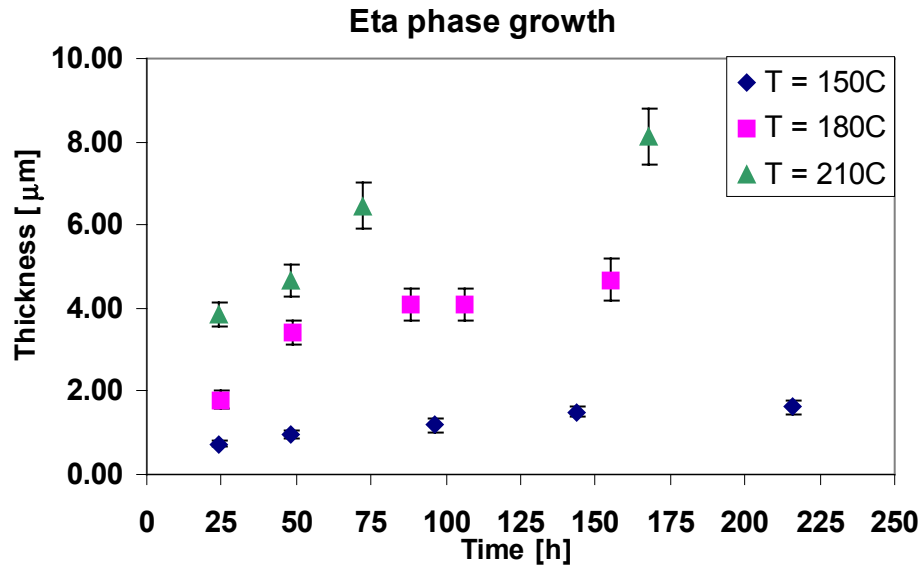
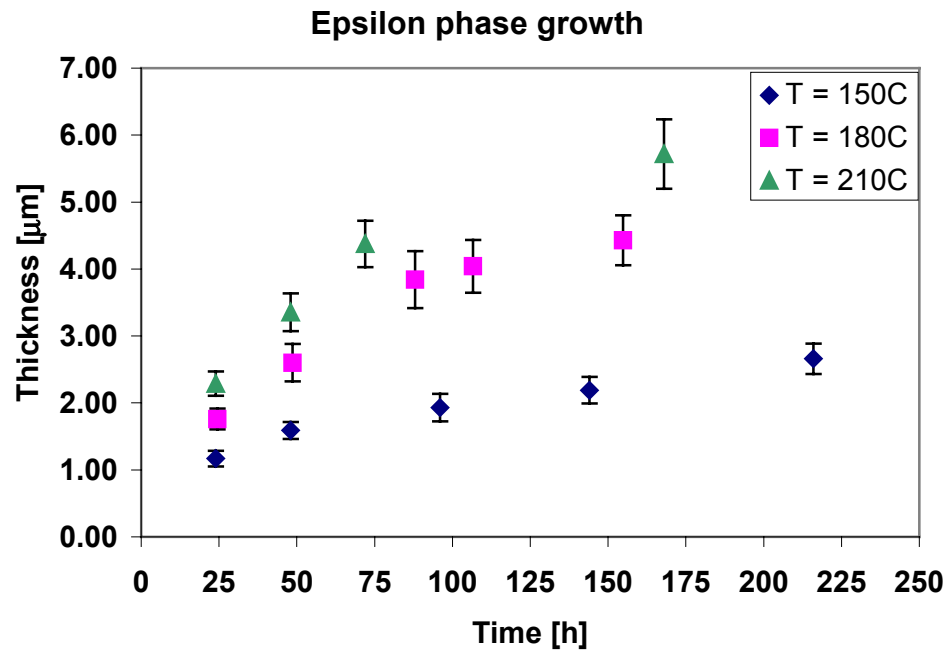
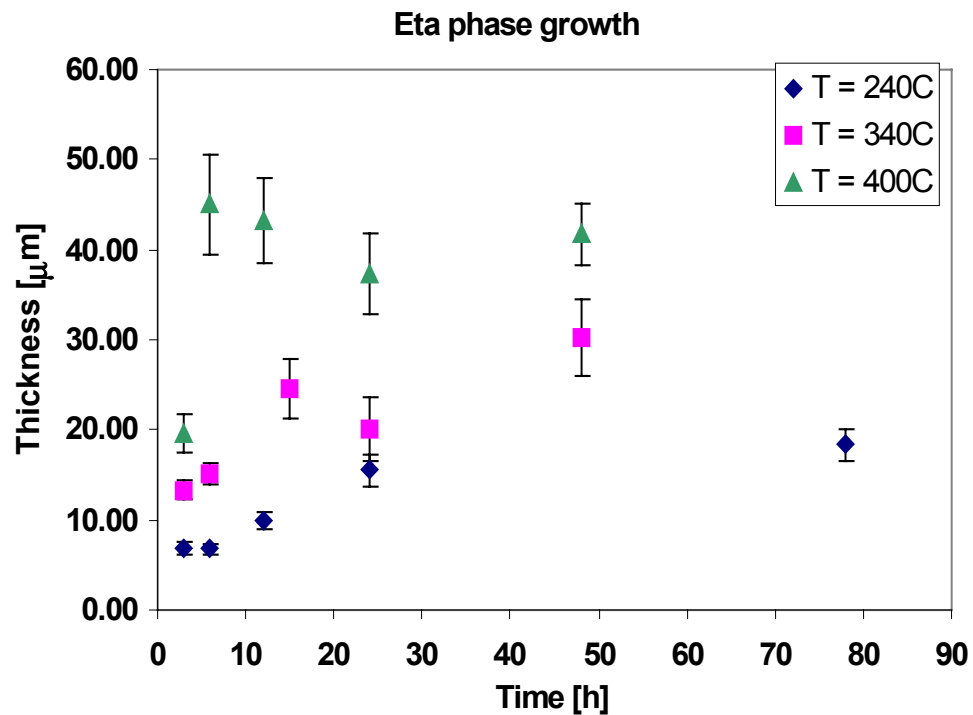


Figure 8.4 Eta phase growth at $T \leq 210$ °C.

At 150 °C the η phase thickness is smaller than the ϵ one, while at 180 and 210 °C the η phase growth is bigger than the ϵ one. Less than 9 μm and than 6 μm thickness forms respectively for η and ϵ phase at 210°C after 168h.

The rates of growth of the ϵ and η phase are both of similar orders of magnitude and are low at 150°C, 180°C and 210°C, if compared with the ones at $T \geq 240$ °C.

Figure 8.5 Epsilon phase growth at $T \leq 210^{\circ}\text{C}$ Figure 8.6 Eta phase growth at $T \geq 240^{\circ}\text{C}$.

Fi

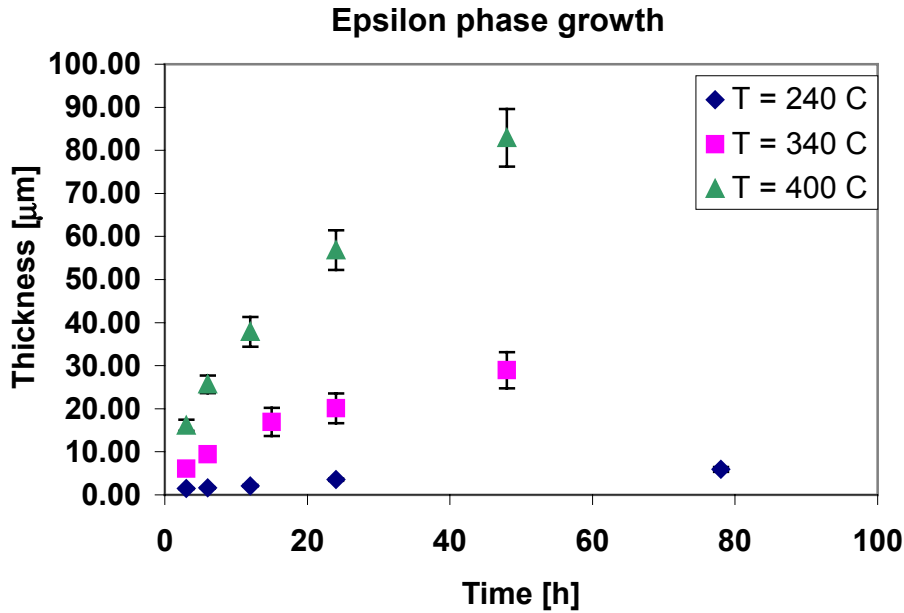


Figure 8.7 Epsilon phase growth at $T \geq 240$ °C.

Figure 8.6 and Figure 8.7 shows respectively the growth of η and ϵ phase at 240, 340 and 400 °C.

The growth of the η phase presents a significant increase above 210 °C. This phenomenon occurs after the melting of the Sn (232 °C) and the development of the η phase inside the liquid. Once the η develops inside the liquid its average thickness cannot be described by the parabolic growth model since the concentration at the interface between η and Cu-Sn solid solution is not constant. The large error bars reflect the scatter in size of the grains growing in the liquid Sn.

In the same temperature range the diffusion of the ϵ phase increases and is strongly temperature dependent between 240 °C and 400 °C. The data shows that the diffusion of Sn in Cu is more effective when the Tin becomes liquid.

It has to be noticed that already after 24 h at 400 °C almost 60 μm thickness of ϵ phase forms. This is about the dimension of most of the strands subelements radius.

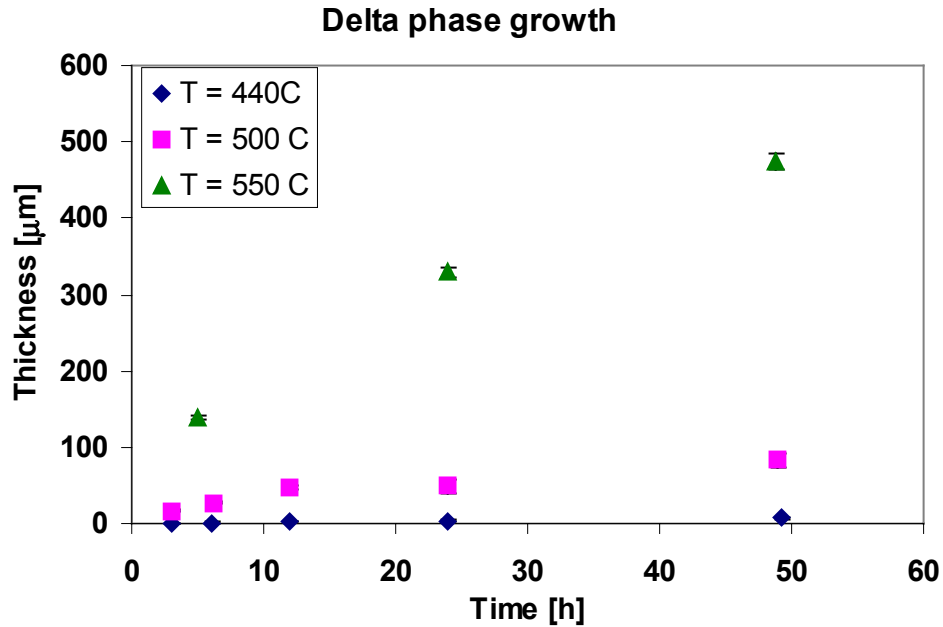


Figure 8.8 Delta phase growth at $T \geq 240$ °C.

Figure 8.8 shows the δ phase growth at 440, 500 and 550 °C.

The rate of growth of the δ phase is strongly temperature dependent and the thickness presents a big gain between 500 and 550 °C. The δ phase thickness formed at 440 and 500 °C is of a similar order of magnitude than the ϵ and η one formed for at 400 °C after similar HT time, while at 550 °C it strongly increases. The thickness formed after 48h and 45min at 550 °C is about 500 μm .

	T range [°C]	E [Kj/mol]	k_0 [cm^2/sec]
η	150 to 227	102 ± 5.94	$2.12 \cdot 10^{-5} \pm 3.35 \cdot 10^{-5}$
ϵ	150 to 227	52.3 ± 3.19	$3.35 \cdot 10^{-11} \pm 2.83 \cdot 10^{-11}$
ϵ	227 to 415	98.4 ± 2.74	$1.29 \cdot 10^{-6} \pm 7.11 \cdot 10^{-7}$
δ	350 to 582	412 ± 10.9	$2.22 \cdot 10^{14} \pm 3.82 \cdot 10^{14}$

Table 8.2 Estimate of E and k_0 for ϵ , η and δ phase in solid diffusion for different temperature ranges.

The thickness, time and temperature measurement of ϵ , δ and η in solid diffusion have been fitted for each phase to obtain an estimate of E and k_0 by minimizing the χ^2 function using the parabolic growth model (equation 8.3). For a comparison between the measured and expected distribution of the data the plots of the thickness versus HT time and temperature, resulted from the fit, are shown in Appendix A.

The estimate of E and k_0 are shown in Table 8.2.

The estimate of E and k_0 are consistent with the values found in literature [55, 56, 57, 58].

8.2.5 Discussion

The evaluation of the E and k_0 for η , ϵ , and δ phase developing in liquid diffusion allows to predict the intermetallic thickness in function of the HT parameters either for a constant and for a variable HT temperature.

The phase growth kinetics investigation shows that for temperatures above 440 °C the δ phase growth is associated with the formation of voids and segregations that may result in cracks along the diffusion path. This phenomenon hinders the diffusion process between Cu and Sn. For this reason the low temperature HT performed over the composites wires to diffuse the Sn in the Cu matrix, should not be performed above 400 °C. Moreover voids when in contact with a Nb₃Sn filament, may introduce stress concentration that decrease the superconducting parameters [59].

The study performed over the Cu-Sn models shows also that for temperatures below or equal to 210°C the diffusion process is slow and a very long time is required to diffuse the Sn in the Cu. As discussed above a long time HT leads to high costs especially for the “Wind and React” approach. Above the melting point of the Sn the rate of growth undergoes a substantial increase both for η and ϵ phase. The most efficient temperature, in terms of HT time, to homogenize the Cu and Sn in solid diffusion below 440 °C is found to be 400 °C. It has shown that already after 24h at 400 °C 60µm of ϵ phase forms, which is the radius of most of the strand subelements.

8.3 CU-SN PHASES GROWTH KINETICS OVER THE STRANDS

The reaction cycle required to produce the superconducting Nb_3Sn phase by a diffusion process of the Tin through the Copper matrix is a critical step in the manufacturing process of a magnet both in terms of superconducting properties and of cost. The latter is mainly related to the long time HT performed on the magnet in the “Wind and React” approach. The final properties of the superconducting wire can be damaged because of the potential movement of the Nb filaments immersed in liquid phases. This phenomenon can allow the contact with adjacent Nb filaments thus increasing hysteresis losses [60]. For this reason during the low temperature HT the low melting point Sn and η phase should be converted into the higher melting point ϵ phase prior they can reach the Nb filaments [61, 62].

Risk of wire burst and Sn leaks due to the overpressure caused by the thermal expansion of the Sn and of the different Cu-Sn phases may also happen [63, 64].

By improving the understanding of the Cu-Sn diffusion process taking place in the strands, it is possible to reduce the risks and the cost of the heat treatment.

The possibility to apply the parabolic growth law and the E and k_0 values obtained from the Cu-Sn models to predict the ϵ intermetallic thickness that forms in the strands in function of the HT parameters is also investigated. This evaluation is performed by comparing the thickness growth versus HT parameters developing in the strands to the one developing in the Cu-Sn models. The comparison is necessary because of the differences between the wire and Cu-Sn models mainly due to the effect of the non “infinite” source of Sn and Cu, to the non planar geometry and to the tensile stresses concentration induced during the wire manufacturing.

8.3.1 Heat treatments

The Cu-Sn growth kinetics study is performed over IT and MJR strands, which characteristics are listed in section 3.4 Table 3.3 and 3.5, for a temperature range between 210 and 400 °C.

This range of temperature has been chosen out of the results of the Cu-Sn models diffusion process investigation. It has been observed that for temperatures above 440 °C the δ phase growth is associated with the formation of voids and segregations that may result in cracks along the diffusion path, therefore hinders the diffusion process between Cu and Sn is prevented.

The study performed over the Cu-Sn models shows also that for temperatures below or equal to 210°C the diffusion process is slow and a very long time is required to diffuse the Sn in the Cu. As discussed above a long time HT leads to high costs especially for the “Wind and React” approach.

However in this range of temperature no liquid phases are present in the strand. An investigation of the Cu-Sn phase growth kinetics in the strand at 210°C is therefore interesting in relation to Sn leaks that may occur after the melting of the Sn. It has to be noticed that 210 °C and 1 week is the HT commonly advised by the manufacturing companies to avoid the problems related to liquid phases.

In order to better understand the processes taking place at this temperature, the diffusion growth kinetics is investigated over the strands also at 210 °C.

For the HT durations at 210, 240, 340 and 400 °C see Table 8.1.

8.3.2 Samples observation and comparison between the thickness growths

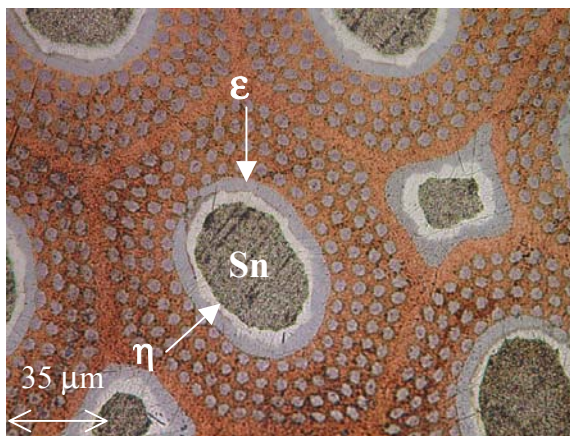


Figure 8.9 ITER strand cross section after 1 week at 210 °C.

After HT the strands are observed at the optical microscope and the average thickness of the Cu-Sn phase is evaluated. Each step is performed following the procedures described in section 5.5. Some examples of the strands cross section after HT are discussed and presented together with the Cu-Sn phase

thickness growth comparison between the IT strand and the Cu-Sn models.

Figure 8.9 shows the sections of the IT strand after 7 days at 210 °C. Both ϵ and η phase thickness is uniform along the interface, as observed for solid/solid interfaces in the models. It should be noted that the layer of the η phase appearing around the Tin pools between the subelements is thicker than the same layer growing inside the subelements. The ϵ phase growing around the Sn pool between the subelements seems to have preferential growth directions.

The acceleration of the ϵ phase growth along some preferential directions may be due to the mechanical induced tensile stresses in the Cu-Nb matrix, caused during the wire manufacturing [60].

It has to be noted that after this HT commonly advised from the manufacturing companies as liquid phases removal problems, most of the Sn is still unreacted. The unreacted Sn will melt above 232 °C. In relation to Sn leakages, however some considerations can be made: the ϵ layer could work as a container for the overpressure due to the Sn melt against Sn leakage.

Figure 8.10 shows the ϵ and η thickness growth comparison between the Cu-Sn models and the IT strand at 210 °C. The ϵ phase thickness difference between the two cases is smaller than the statistical error, besides at 24h, where the thickness in the strand is slightly bigger than in the model. It has to be noticed that the thickness of ϵ phase after 1 week is only about 1 μ m bigger than the one obtained after 3 days. This suggests to evaluate the possibility to shorten the HT time of 1 week normally adopted against Sn leaks.

The η phase growth in the strand is considerably smaller than the one in the

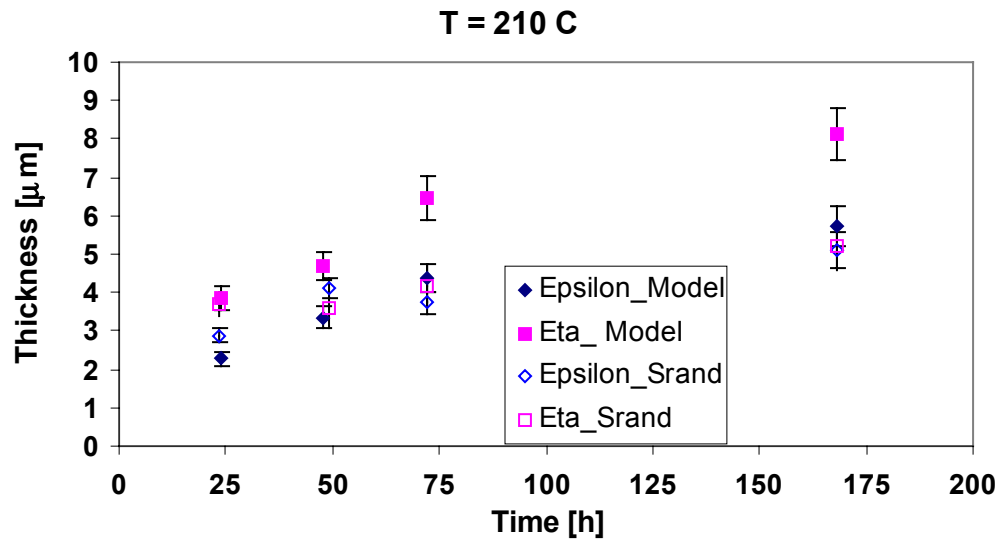


Figure 8.10 Epsilon and Eta phase growth in the ITER strand and in the Cu-Sn models at 210 °C.

Cu-Sn models beside at short times reaction (24h).

Figure 8.11 shows a solid/liquid interface at 240 °C. As observed for the Cu-Sn models, the thickness of the η phase developing inside the liquid is not

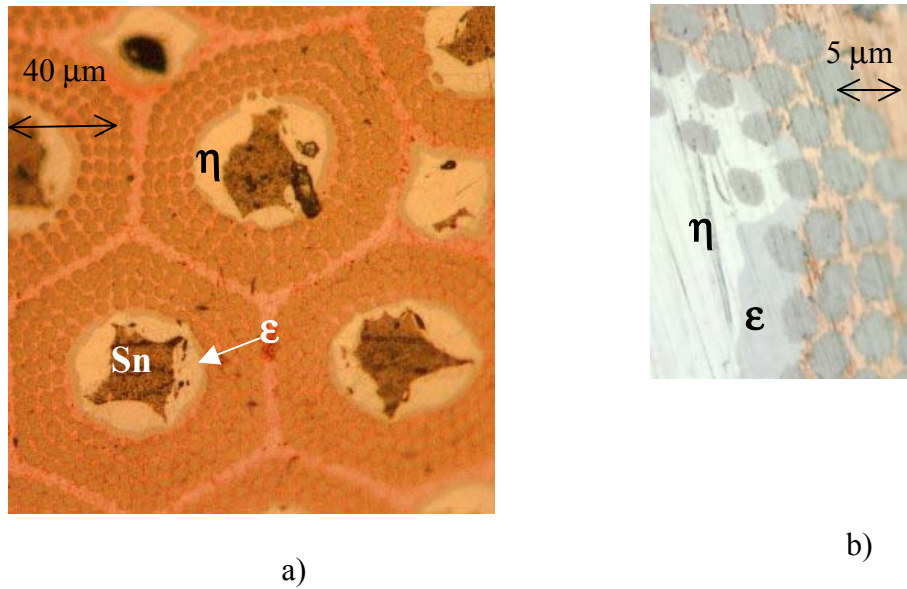


Figure 8.11 ITER strand cross section at 240 °C a) after 12h b) after 78h.

uniform along the interface (Figure 8.1). In this case, however, there seems to be some preferential growth directions, both inside the subelements and around them. This may be due to the different stress concentration inferred during the drawing to the strand as seen at 210 °C [60].

In some cases, the η phase reaches the Nb filaments. This may happen both at short and long time reaction as shown from Figure 8.11. In these cases the Nb filaments are surrounded by a non homogeneous Cu-Sn phase matrix.

Figure 8.12 shows the comparison between the growth of ϵ and η phase in the Cu-Sn models and in the ITER strand.

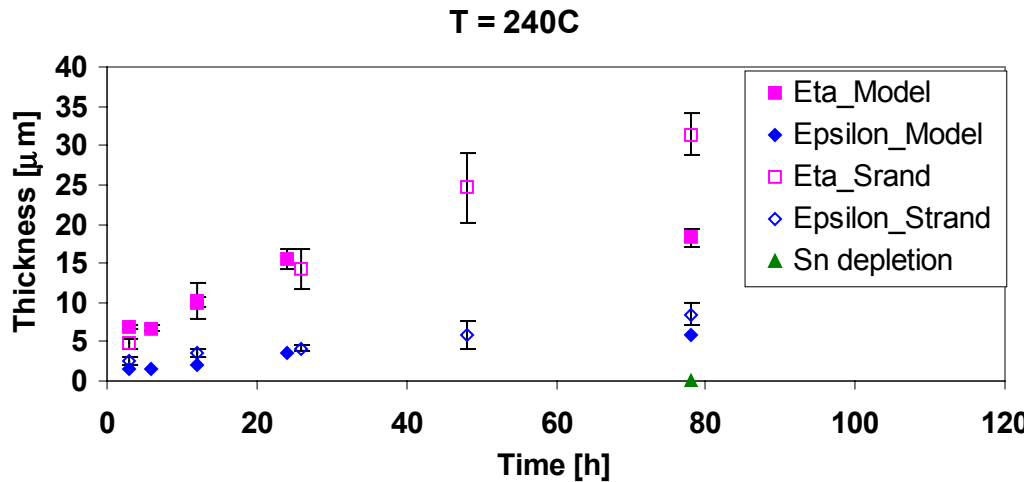


Figure 8.12 Epsilon and Eta phase growth in the ITER strand and in the Cu-Sn models at 240 °C.

The large η error bars reflect the scatter in size of the grains growing in the liquid Tin. Before the depletion of the Sn, the growth in the Cu-Sn models and in the ITER strand is similar both for η and ϵ phase, being the thickness difference less than the statistical error. When the Sn is exhausted (the phenomenon is observed at 78h), the η phase thickness is considerably bigger in the ITER strand than in the Cu-Sn models, while there is no substantial difference for the ϵ phase thickness.

Figure 8.13 shows the growth of ϵ and η phase at 340 °C. After 15h, some Sn is still unrecated, while after 24h and 20min the Sn is completely exhausted. In both cases the η phase thickness is not uniform along the interface.

As shown in Figure 8.13 η phase does not reach the Nb filament, while ϵ phase reaches only the first ring of the Nb filaments, this phenomenon has been for all the samples.

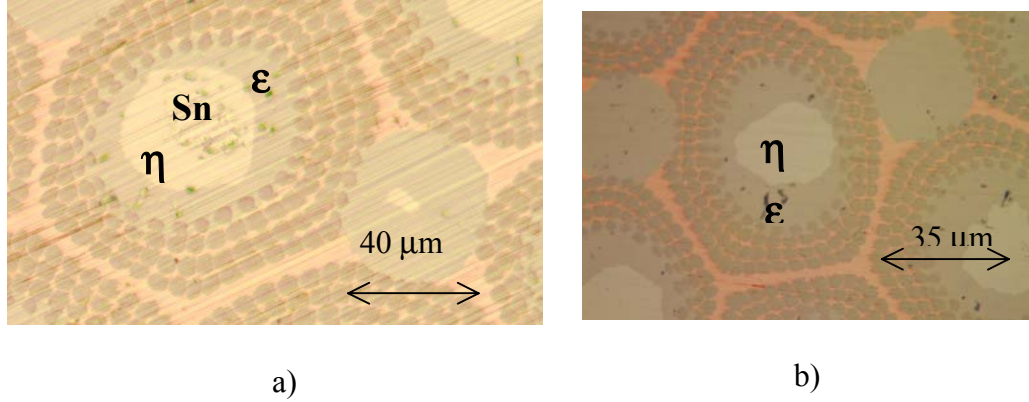


Figure 8.13 ITER strand cross section at 340 °C a) after 15 h b) after 24 h.

Figure 8.14 shows the comparison between the thickness growth of η and ϵ phase in the Cu-Sn models and in the ITER strands at 340 °C.

The growth of ϵ phase in the strand is similar to the one in the Cu-Sn models for short HT times. When approaching and after the Sn exhaustion the ϵ phase growth in the strand is smaller than in the Cu-Sn models. The η phase thickness is always smaller in the strands than in the Cu-Sn models, beside at 24h, time at

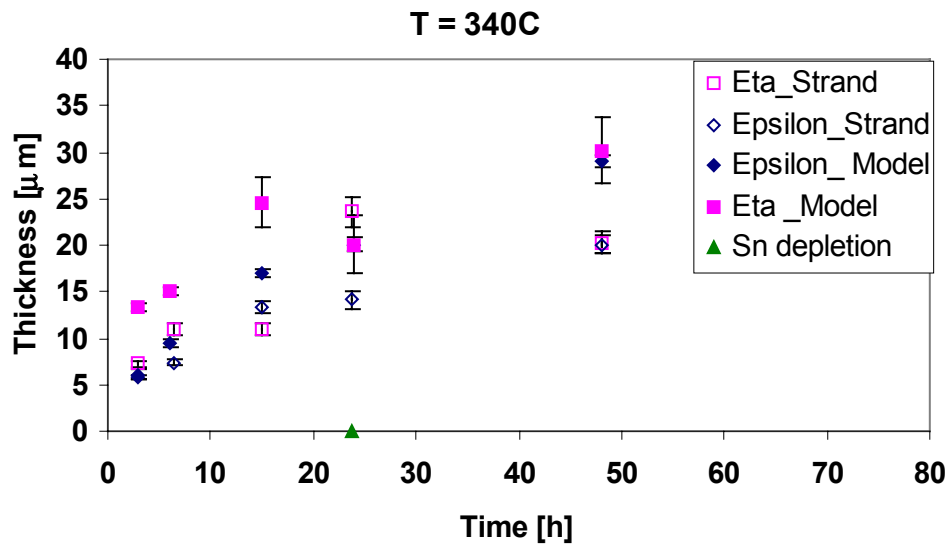


Figure 8.14 Epsilon and Eta phase growth in the ITER strand and in the Cu-Sn models at 340 °C.

which the exhaustion of the Sn is observed.

After the Sn source is exhausted, the η phase begin shrinking while the ϵ phase keeps growing.

Figure 8.15 shows the ITER strand cross section after 48h at 400 °C. The Tin has been completely converted into ϵ phase. For all the subelements the ϵ phase reaches uniformly only the second ring of Nb filaments. Some α phase begin

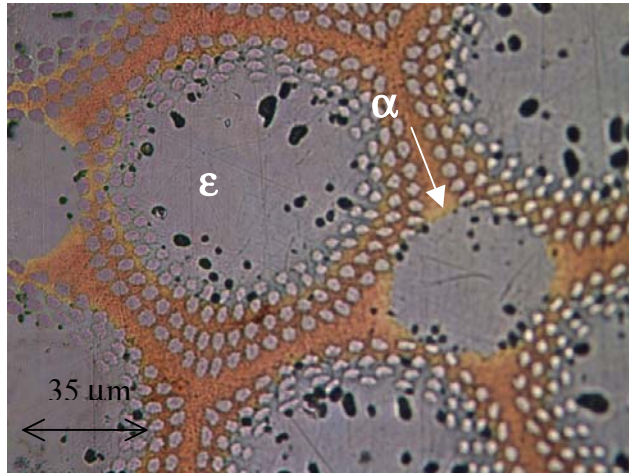


Figure 8.15 ITER strand cross section at 400 °C after 48h

appearing around the outer ring of the Nb filaments. It appears that it is not possible to obtain homogeneous conditions for all the Nb filaments.

Some voids have been formed inside ϵ phase, as observed in the Cu-Sn models.

Figure 8.16 shows the η and ϵ phase growth comparison between the Cu-Sn models and the ITER strand at 400 °C.

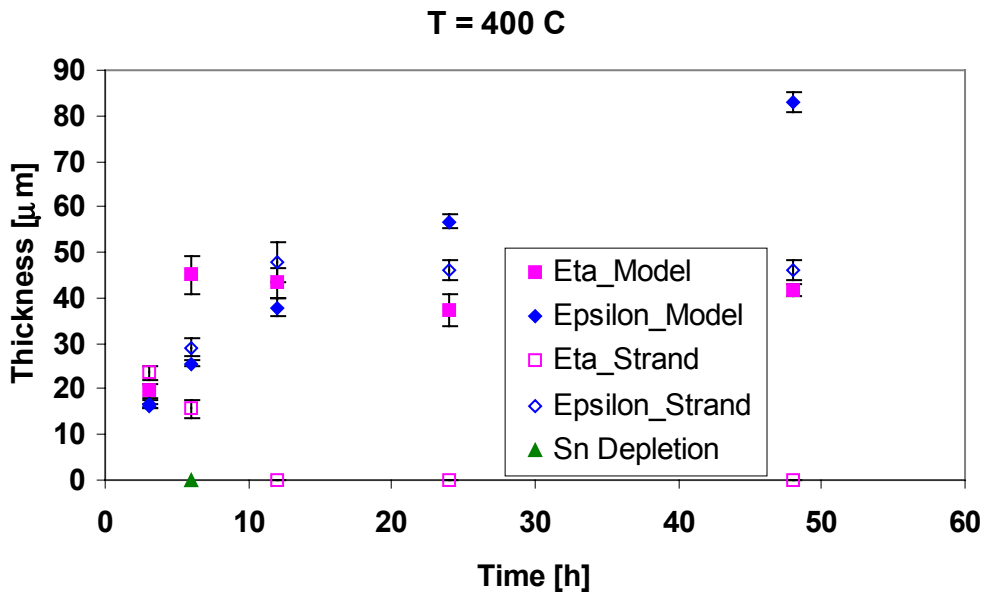


Figure 8.16 Epsilon and Eta phase growth in the ITER strand and in the Cu-Sn models at 400 °C.

Before the depletion of the Sn both the η and ϵ phase thickness is similar in the strand and in the Cu-Sn models, being the difference smaller than the statistical error. When the Sn is exhausted (phenomenon observed at 6h), the ϵ phase keeps growing and the η phase begin shrinking. When also the η phase is exhausted (phenomenon observed at 12h) the ϵ phase thickness seems slightly decreasing probably because of the growth of the α phase. It has to be noticed that already after 12h all the Sn is completed converted into ϵ phase.

The results obtained for the MJR strand, presented in Appendix B, are in agreement with the one obtained in the ITER strand.

8.3.3 Discussion about the Growth comparison

The result of the thickness growth investigation in ITER strands shows that before the depletion of the Sn, the average thickness of ϵ phase is similar to the one formed in the Cu-Sn models, being the thickness difference less than the statistical error. When the Sn of the original pool is exhausted, η phase supplies the Sn for the growth of the ϵ phase. When also the η phase is exhausted the ϵ phase stops growing and its thickness begin decreasing due to the formation of the α phase. However this latter phenomenon, observed only at 400 °C, seems to occur with a very slow rate.

Some local growth discrepancy observed inside the subelements and around them, could be due to the mechanical induced tensile stresses in the Cu-Nb matrix caused during wire manufacturing [60].

From these results it can be concluded that before the depletion of the Sn the ϵ phase average thickness can be predicted with small approximation in function of the HT time and temperature using the E and k_0 evaluated for the Cu-Sn models. The approximation is realistic, being the difference between the thickness in the ITER strands and in the Cu-Sn models less than the sum of the statistical errors. This occurs for all the HT investigated, besides at 210 °C after 24h; after this HT the ϵ thickness in the ITER strand is $\frac{1}{4}$ bigger than the one in the Cu-Sn models.

The η phase growth in the ITER strand is in general different from the one observed in the Cu-Sn models. Some causes can be related to the depletion of the Sn, to the tensile stress concentrations induced during the drawing, to the presence of the filaments and to the non planar geometry of the Cu-Sn interface.

8.3.4 Discussion about the heat treatment optimization

The strand cross section observation and the thickness growth investigation on the ITER strand shows that the Sn can not be uniformly and homogeneously distributed around all the Nb filaments prior to the beginning of the A15 phase formation for an ITER composite strand with a subelement $\sim 125 \mu\text{m}$ in diameter and with the composition listed in Table 3.3.

The low melting point Sn and η phase can totally be converted into the higher melting point ϵ phase and some traces of α phase at 400°C already after 12h, without the liquid phases reach the filaments. This prevents the damage of the superconducting wire because of the potential movement of the Nb filaments immersed in liquid phases.

However the limited content of Sn does not allow the formation of an ϵ pool with a radius at least equal to one of the subelement. Therefore the inner ring of the Nb filaments is immersed into ϵ phase, while the outer ring is immersed in α phase and/or pure Cu leading to different surrounding conditions around the Nb filaments at the formation of the Nb_3Sn compound.

As for the mechanical problems related to liquid phases, it has to be mentioned that no wire burst or Sn leakages has been observed in the virgin strands. This introduce a discussion on the necessity to perform the long hold step at temperatures below the melting point of the Sn, made in order to allow the formation of higher melting point Cu-Sn phases via solid state diffusion prior to an increase in the HT temperature.

Even if Sn leakages did not occur in the virgin strands they resulted to occur during the HT performed over the magnets [63] therefore it would be necessary to study this phenomenon on cables to better understand the relation between Sn leakages and the HT performed on the magnets.

The results of the study on the strands show that a complete transformation of the pure Sn into a higher melting point phase occurs in a very long time at temperatures below the melting point of the Sn. Figure 8.9 shows that after 1 week at 210 °C, the usual manufacturers' suggested liquid phases removal problems hold step, a large fraction of the Sn is still unreacted. However the hold steps HT at temperature below 232 °C, allows the formation of an ϵ phase thin layer that may eventually work as a container against the overpressure of the liquid Sn above 232 °C.

However the ϵ phase thickness formed at 210°C after 1 week is about only 1 μm bigger than the one formed after 3 days (the thickness formed after 72h is 4.4 μm , while after 168h is 5.7 μm). Because of the great influence of the HT time on the cost of the magnet manufacturing especially in the “Wind and React” approach, it should be considered to check on the cables the possibility to shorten the HT time at 210°C.

8.4 EFFECT OF PARTIALLY REACTING Nb_3Sn BEFORE WINDING ON THE STRAND CRITICAL CURRENT

The feasibility of winding partly reacted cables to reduce the HT time of the magnet is explored [50, 51]. ITER and MJR strands, which characteristics are given in section 3.4 Table 3.3 and 3.5, have been partially reacted to convert the Sn into the ϵ and η phase and then plastically strained to figure out a cabling and/or a winding degradation [52, 53, 54,]. After completion of the reaction cycle, the critical current is measured and compared with that obtained with an uninterrupted HT cycle.

The pre-HT are chosen out of the previous work performed on the Cu-Sn growth kinetics. The Pre-HT at 210 °C and 1 week is chosen because of the interest in this step due to the liquid phase problems, as discussed in section 8.3 The HT at 400 °C and 2 days is chosen because it leads in a short time to the best homogenization of the Cu-Sn matrix among the HT investigated; hence, after 48h

at 400°C the Sn and η phase are completely transformed into ϵ phase and small traces of α phase.

After the pre-HT, which parameters are given in Table 8.3, the samples are wound on grooved cylindrical Ti-alloy barrels to figure out a winding degradation, and held in place by two removable end rings. Then the samples are heat treated at 700 °C to form the Nb₃Sn compound. The procedures used to prepare and HT the samples are detailed described in chapter 6.

After completion of the HT cycle, Cu rings replace the Ti-alloy end rings, and the sample voltage-current characteristics are measured with the set up described in section 6 for magnetic field ranging from 6T to 15T.

Pre-reaction	Ramp rate, [°C/h]	25	25
	Temperature, °C	210	400
	Duration, h	168	48
Nb₃Sn formation	Ramp rate [°C/ h]	6	6
	Temperature [°C]	700	700
	Duration [h]	40	40
Reference HT	Ramp rate, °C/h	30	30
	Temperature, °C	400	400
	Ramp rate, °C/h	6	6
	Temperature, °C	700	700
	Duration, h	40	40

Table 8.3. Heat treatment cycles.

It is worthwhile to mention that the winding of the strands was not difficult and that the strands were not brittle as completely reacted Nb₃Sn strands are. The strands had less spring back than before the pre-HT, especially the one heat treated at 400 °C. This may be due to the recrystallization of the Copper.

The results of the I_c measurement are compared to the reference values measured on the same strands. The reference values are average values of 7 measurements in the case of the ITER strand and of 5 measurements in the case of

the MJR strand. The measurements used to determine the reference values all use strands HT at 700 °C during the HT final step.

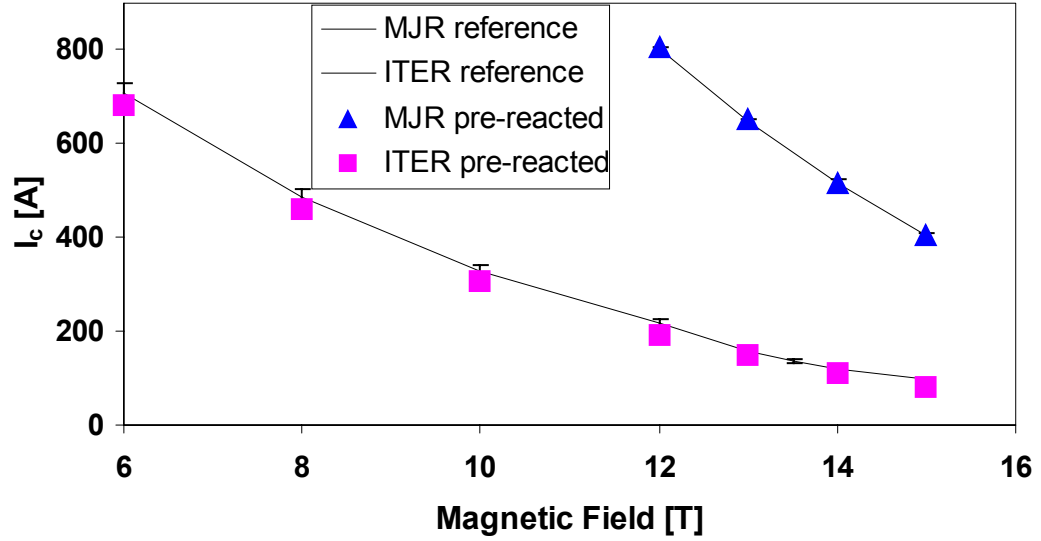


Figure 8.17 Critical current of the pre-reacted ITER and OST strands compared to reference values for each strands. Pre-reaction cycle:7 days at 210°C

No substantial I_c degradation due to the pre-HT to convert the Sn into η and

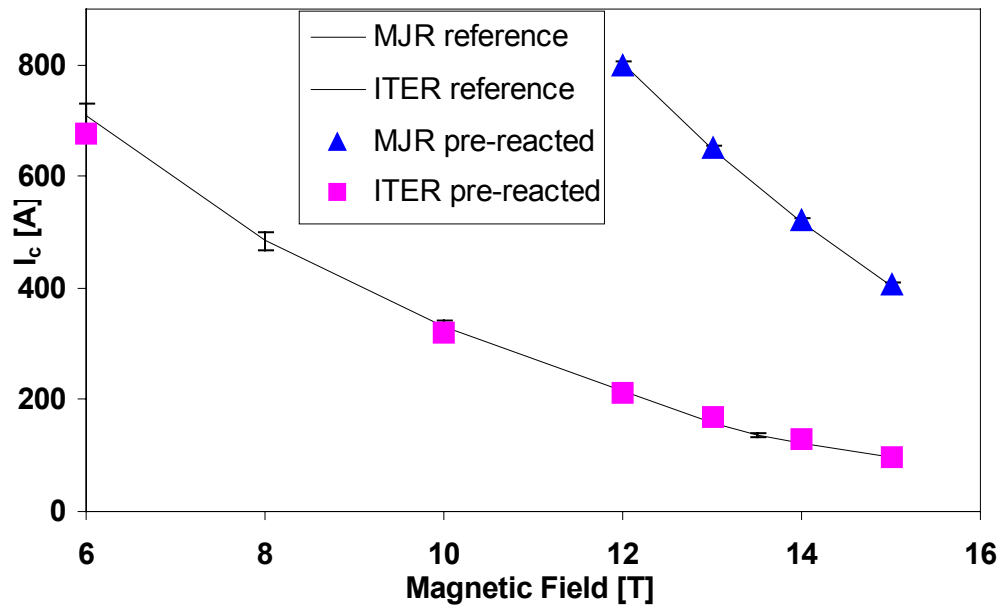


Figure 8.18 Critical current of the pre-reacted ITER and MJR strands compared to reference values for each strands. Pre-reaction cycle:48 h at 400°C

ϵ intermetallic phases is observed for both the two pre-HTs and strands technology, as shown respectively in Figure 8.17 and 8.18

	ITER Strand	MJR Strand
Reference	184 ± 40	23 ± 1
Pre-treatment 210°C - 7 days	257 ± 34	$17 \pm$
Pre-treatment 400°C - 2 days	$203 \pm$	37 ± 3

Table 8.4. *RRR* measurements after the heat treatment cycles

The *RRR* of the strands has also been measured at the end of the HT. The results are presented in Table 8.4. The difference in *RRR* as a consequence of the pre-HT is attributed to the difference in technologies used to manufacture the strands.

As shown from the results of the I_c the preliminary heat treatments on Nb_3Sn superconducting wires can be made to convert the Sn in the intermetallic phases η and ϵ prior to winding without generating degradation in the final superconducting properties of the strands. This result on the strands paves the way to the “Prereact-Wind-React” approach to reduce substantially the time needed for the coil reaction.

It has also to be observed that the I_c values obtained with the two different Pre-HT present not substantial difference both for the ITER and the MJR strand even if the two pre-HT lead to different homogenization condition of the Cu-Sn matrix. This suggests that the inhomogeneity after the low temperature HT step to mix the Cu and the Sn does not have a significant influence on the I_c of the subsequently formed A15 phase in fully reacted wires [65] in the two strands investigated.

8.5 SUMMARY

The phase growth kinetics investigation performed over Cu-Sn models allowed to evaluate the E and k_0 for ϵ , η and δ phase in solid diffusion using a parabolic growth model. This gives the possibility to predict the thickness of the three intermetallic phases in function of the HT parameters.

Moreover the study shows that for temperature above 400 °C the δ phase growth is associated to the formation of voids and segregation that hinders the diffusion process. For this reason the low temperature HTs performed over the superconducting strands to homogenize the Cu-Sn matrix, should not be performed above 400 °C.

It has also been showed that the growth of the Cu-Sn phases for temperatures below the melting point of the Sn is slow if compared to the one corresponding to higher temperatures.

The growth kinetics investigation performed over ITER and MJR strands shows that the most efficient temperature to homogenize the Cu-Sn matrix is 400 °C. Already after 12 h all the Sn and η phase are converted into ϵ phase. However due to the limited content of Sn the ϵ phase pool does not reach all the Nb filaments leading to not uniform conditions around them. The I_c results showed in section 8.4 suggest however that the different homogenization conditions (obtained at 400 C after 48 h and at 210 C after 1 week) of the Cu-Sn matrix does not lead to an appreciable difference of critical current.

It has been showed that the HT commonly advised to avoid liquid phases problems (210 °C and 1 week) does not remove all the Sn. The thin layer of ϵ phase formed at this stage that could work as a container against the overpressure due to the liquid Sn thermal expansion, is only 1 μm bigger than the one formed after 3 days. Due to the importance of reducing the HT cost in the “Wind and React” approach it should be considered to perform studies on the cables to check the necessity of performing a long hold step a 210 °C.

The possibility to shorter the HT time of the magnet performing the low temperature HT to homogenize the Cu-Sn matrix, prior the winding shows that no critical current degradation has been observed in the ITER and MJR prereacted-wound-reacted strands. This paves the way to prerecat cables before winding the magnet.

IX

RESULTS ON THE Nb₃Sn FORMATION AND SUPERCONDUCTING PROPERTIES

9.1 INTRODUCTION

The development of high critical current density (J_c) multifilamentary Nb₃Sn wires is fundamental for many technological applications, including the design of high field accelerator magnet, as discussed in section 3.5. Up to now the J_c is still below the required value of 3000 A/mm² [33].

Although extensive studies of superconducting properties of these composites have been performed very small metallurgical information is available on the formation of the A15 compound from the composites. Hence it is of great value to investigate and understand the kinetics mechanisms involved in the formation and growth of these compounds. Such an understanding of the factors involved in the compound formation and the effect of various heat treatments upon its structure will contribute to the improvement of the superconducting properties.

The I_c of Nb₃Sn superconducting strand depends on numerous factors among which the amount, the stoichiometry and the grain dimensions of the A15 compound. The dependence of J_c on stoichiometry has been widely studied [66, 67] as the dependence on grain dimensions in relation to the flux-pinning force, (see chapter 2), [68, 69, 70, 71].

Both the three parameters are strongly dependent on the high temperature heat treatment performed over the strand.

In order to optimize the superconducting properties of Nb₃Sn in function of the HT parameters the growth kinetics of Nb₃Sn is investigated and the superconducting properties are evaluated after each HT. The Nb₃Sn thickness is measured after each HT and the area is calculated over the entire cross section of the strand. I_c measurements are performed for each HT at different magnetic fields ranging from 15 to 4 T. The J_c is calculated over the Nb₃Sn area. In order to distinguish the critical current density calculated over the Nb₃Sn area (J_{cl}) from the one usually calculated over the non-Cu area, this will be indicated as J_{cl} . The B_{c20} is evaluated by fitting the I_c data versus magnetic fields, accordingly to Summers parameterization, as described in section 6.7.

By correlating the superconducting properties of Nb₃Sn to the HT parameters and to the amount of A15 compound formed it is possible also to predict the optimum Nb filament size with respect to the superconducting properties taking into account the technological and magnetic field quality issues [72].

9.2 Nb₃Sn GROWTH KINETIC INVESTIGATION

The Nb₃Sn growth kinetics process is investigated mainly to obtain a relation between the volume of the A15 compound and the HT parameters. The study is performed over two different strands technologies: IT and PIT, which characteristics are given in section 5.3.1 (Table 5.1) and in section 3.4.4 (Table 3.6), using a very large filaments designs in order to allow measuring the Nb₃Sn area with the optical microscope at its highest magnification (100X). Both the two

strands have an excess of Sn respect to the stoichiometry, so in principle it is possible to transform all the Nb into Nb₃Sn. The Sn content however is not “infinite” and during the diffusion process between Nb and the bronze matrix in the IT strand or between Nb and the NbSn₂ matrix in the PIT strand, the matrix undergoes a depletion of Sn. Hence the concentration at the boundary between the Nb₃Sn layer and the matrix is not constant. Under this condition the rate of growth of the Nb₃Sn compound depends on the concentration difference at the boundaries of the interlayer and the growth of the Nb₃Sn compound is expected not to follow the parabolic growth law. As an approximation equation 4.19 (see section 4.2) can be used to fit the thickness data versus time and temperature to obtain some reference values for the Nb₃Sn growth kinetics relatively to the geometry and composition of the strands investigated.

9.2.1 Heat treatments

IT and PIT short samples for thickness measurements, and coils for the critical current measurement, (see section 6.3), are heat treated together for the same HT duration, with the procedures described in section 6.3 and 5.3.2.

The HT performed over the IT strand consists of two steps: the first step at low temperature, to homogenize the Cu-Sn matrix, the second step at high temperature to form the Nb₃Sn. The low temperature step has been determined out of the study performed over the Cu-Sn system, discussed in previous chapter. The temperature of 400 °C has been chosen because it allows obtaining a homogeneous ϵ phase in the shortest time with no damage observed in the virgin strands.

The duration of the HT has been determined as the time needed to obtain an ϵ pool with a diameter equal to the one of the entire subelement. In this condition all the Nb filaments would be immersed in a homogeneous ϵ phase, if the Sn did not exhausted. As observed in previous chapter, the low Sn content of the 19 subelements IT strands does not allow obtaining an epsilon pool immersing all the Nb filaments.

To obtain the estimate of the subelement dimension the radius of 16 subelements has been measured and the average value of 60 μm has been calculated. The duration of the first HT step has been calculated with the parabolic growth law (equation 4.10) using the activation energy and diffusion frequency values estimated for the ϵ phase, as discussed in previous chapter, in the temperature range of 227-410 $^{\circ}\text{C}$. The time needed to form an ϵ phase pool of 60 μm in radius at 400 $^{\circ}\text{C}$ is found to be 33 h and 12 minutes. The duration has been increased to 80 h to take into account eventual thickness growth discrepancy due to the different geometry and composition between the IT strand and the Cu-Sn models used to obtain the activation energy and diffusion frequency estimate.

The second step of the heat treatment is performed both over the IT and PIT strands simultaneously. The temperature range has been chosen taking into account the values advised by the manufacturing companies, (see section 3.4) and taking into account the temperature limitation imposed by the react and wind technique.

A scheme of the heat treatment is presented in Table 9.1.

		IT	PIT
Pre-HT	Temperature [$^{\circ}\text{C}$]	400	
	Duration [h]	80	-
	Ramp Rate [$^{\circ}\text{C}/\text{h}$]	150	
HT	Temperature [$^{\circ}\text{C}$]	750	750
	Duration [h]	2, 5, 10, 20, 40	2, 5, 10, 20, 40
	Temperature [$^{\circ}\text{C}$]	700	700
	Duration [h]	5, 10, 20, 40, 80	5, 10, 20, 40, 80
	Temperature [$^{\circ}\text{C}$]	650	650
	Duration [h]	50, 100, 200, 400	50, 100, 200, 400
	Ramp Rate [$^{\circ}\text{C}/\text{h}$]	150	150

Table 9.1 Heat Treatments performed over IT and PIT strands

9.2.2 Diffusion samples observation

The cross section of each strand is observed at the optical microscope after heat treatment to investigate the growth process of Nb₃Sn. Some examples are shown and discussed.

Figure 9.1 shows the IT section after 5h and 40 h at 750 °C. The Nb₃Sn thickness is uniform along the interface and no voids form inside the superconductor. Voids however are present inside the Cu-Sn matrix and they came also in contact with the Nb₃Sn compound. The amount of voids increases in correspondence to the increase of the Nb₃Sn volume. Voids, observed in all the samples investigated, when in contact with the Nb₃Sn may reduce the superconducting properties introducing local stress concentration [62].

Figure 9.1 shows that the composition of the Cu-Sn matrix undergoes a consistent Sn depletion during the diffusion process: at 750°C after 5 h some rich Sn phases are still present in the matrix, while after 40 h only α phase is left.

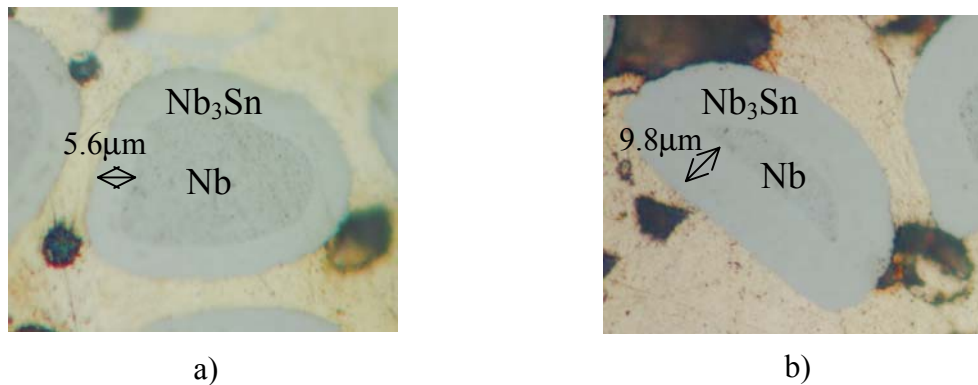


Figure 9.1 IT strand cross section at 750 °C a) 5h; b) 40h.

Figure 9.2 shows the PIT cross section after 5 h and 40 h at 750 °C. The Nb₃Sn-Nb interface is uniform, while the Nb₃Sn-Sn interface presents some irregularities. Voids are present inside the Sn pool already after 5h and their amount increases after 40h. It should be noticed that after 5h at 750 °C a substantial amount of Nb₃Sn, if compared with the one formed after 40h, already forms. After 40h at 400 °C almost all the Nb is converted in Nb₃Sn and the Nb barrier thickness is significantly reduced. The reduction of the Nb barrier can lead

to the contamination of the Cu in the matrix with a decrease of the stabilizing effect of the Cu matrix, as discussed in section 3.2. No contamination of the Cu matrix has been observed in any sample, however the results of the *RRR* measurement, discuss in section 9.3.4, shows that the resistivity of the Cu matrix substantially decreases with the HT time, *i.e.* the Nb₃Sn area.

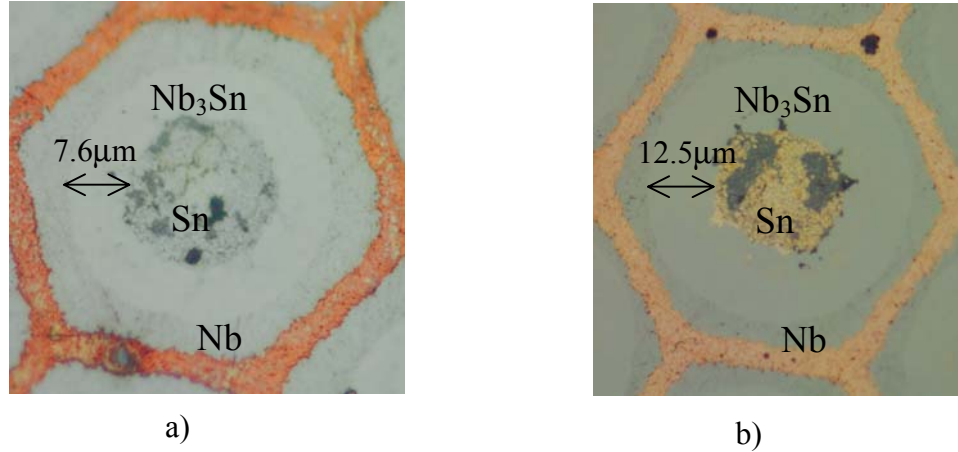


Figure 9.2 PIT strand cross section at 750 °C a) 5h; b) 40h.

9.2.3 Nb₃Sn Growth Kinetic

Figure 9.3 shows the Nb₃Sn thickness growth in IT strand at 650, 700 and 750 °C. As it can be observed, the Nb₃Sn growth is strongly temperature dependent and presents a big gain between 700 and 750°C. This could be due to the melting of most Cu-Sn phases above 700 °C.

As discussed above, due to the Sn depletion in the matrix, the trend of the Nb₃Sn thickness versus time and temperature can not be described by a parabolic growth law. The design weight percentage of the Sn in the matrix before the Nb₃Sn formation is 20%; after hypothetical Nb full reaction the calculated Sn weight percentage is around 4.3%.

In order to have a rough estimate of the growth at the three different temperatures the data are fitted for each temperature with equation 4.19 using the least square method.

The value of the exponent n results to be very different between the three temperatures: 2.3 at 750 °C, 1.46 at 700 °C and 0.88 at 650 °C. Only at 750 °C, n

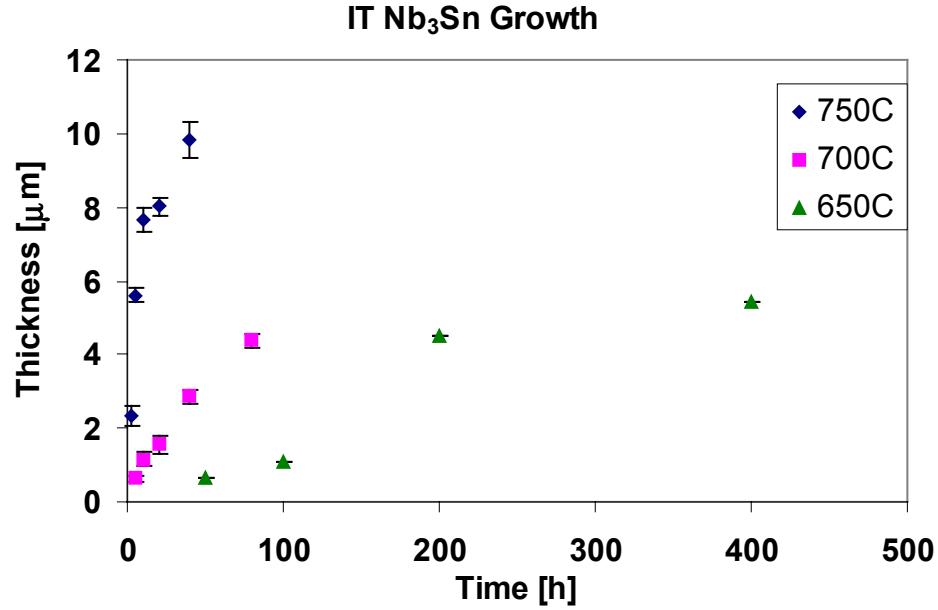


Figure 9.3 Nb₃Sn growth kinetics in IT strand in function of the HT time at 750, 700 and 650 °C

is close to 2. As mentioned in section 4.5.2, the deviation from the parabolic growth law can be attributed to the depletion of the Sn inside the matrix for $n > 2$, or to crack in the layer for $n < 2$, that accelerate the diffusion process. However some deviations in this case can also be due to the non planar geometry of the system and to the variation of the Sn concentration gradient along the Nb₃Sn interlayer during the growth. The non constant concentration gradient is due to the large range of composition of the Nb₃Sn intermetallic compound (18%a-25%a Sn). The composition of the Nb₃Sn layer seems also to vary with the HT temperature and time, as it is shown by the trend of the B_{c20} , discussed in section 9.3.1. This could also explain the different growth law exponent found for the three temperatures.

The value of the rate of growth for the three temperature resulted to be: $6.53 \cdot 10^{-17} \text{ m}^{2.3} \text{ sec}^{-1}$ at 750 °C, $5.45 \cdot 10^{-14} \text{ m}^{1.46} \text{ sec}^{-1}$ at 700 °C, $2.01 \cdot 10^{-11} \text{ m}^{0.88} \text{ sec}^{-1}$ at 650 °C.

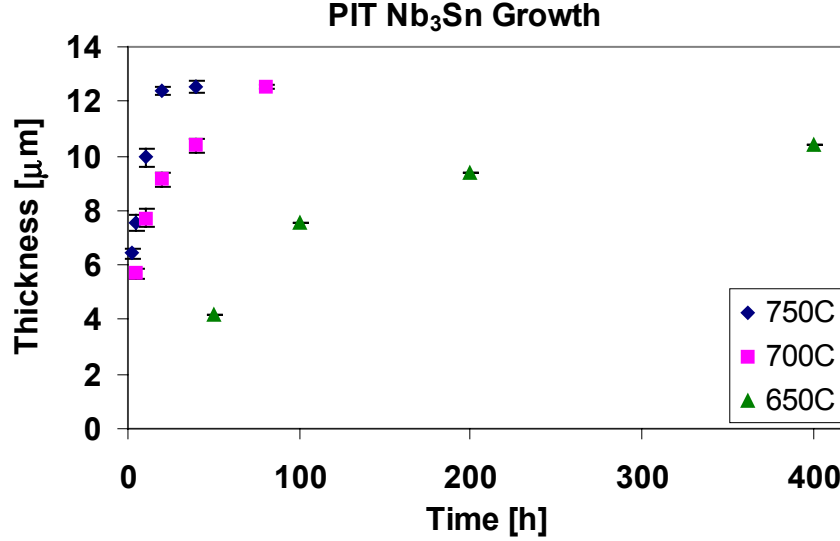


Figure 9.4 Nb₃Sn growth kinetics in PIT strand in function of the HT time at 750, 700 and 650 °C

Figure 9.4 shows the Nb₃Sn thickness growth in PIT strand at 650, 700, 750 °C. It can be observed that the Nb₃Sn growth is strongly temperature dependent and presents a big gain between 650 and 700 °C. It has also to be observed that the growth at 650 °C is bigger in the PIT than in the IT strand. A consistent amount of Nb₃Sn forms after a very short time heat treatment at 700 and 750 °C: almost half of the thickness formed after 40h at 750 °C and after 80 h at 700 °C forms after respectively 2 h and 5 h. As discussed in section 7.2.4, in the PIT strand a substantial amount of Nb₃Sn forms during the heating and cooling transients of the HT for all the three temperatures investigated. This leads to a systematic difference between the measured thickness value and the one that would form during the HT measured time and temperature. The systematic effect correction on the data is shown in Figure 9.5.

The thickness data have been fitted using equation 4.19 with the least square method in order to obtain a rough estimate of the exponent n and of the rate of growth. The exponent n and the rate of growth are found to be: 3.7 and $6.92 \cdot 10^{-24} \text{ m}^{3.7} \text{ sec}^{-1}$ at 750 °C, 3.6 and $1.19 \cdot 10^{-23} \text{ m}^{3.6} \text{ sec}^{-1}$ at 700 °C, 2.3 and $5.04 \cdot 10^{-18} \text{ m}^{2.3} \text{ sec}^{-1}$ at 650 °C.

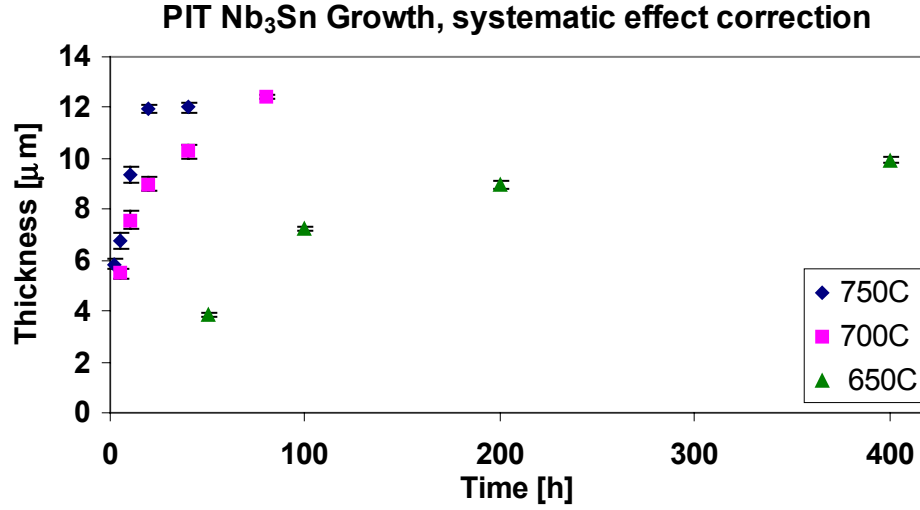


Figure 9.5 Nb₃Sn growth kinetics in PIT strand in function of the HT time at 750, 700 and 650 °C after systematic effect corrections

The value of the exponent n is different for each temperature and, as found for the IT strand, it decreases with the temperature.

The considerations on the deviation from the parabolic growth law made for the IT strand can be applied also to the PIT strand.

Also in this case both the concentration of Sn at the interface with the Nb₃Sn and the Sn concentration gradient along the Nb₃Sn interlayer are not constant during the diffusion process and, as observed for the IT strand, the trend of the B_{c20} , discussed in section 9.3.3, indicates that the composition of the Nb₃Sn layer varies with the HT temperature and time.

The estimate of the exponent n and of the rate of growth of the Nb₃Sn obtained for the PIT and for the IT strands are reference values for the growth at 750, 700 and 650 °C in the two particular strands investigated. Since the rate of growth of the interlayer depends on the composition of the matrix at the interface with the Nb₃Sn, the growth law depends on the composition of the strand. Hence in general the exponent n and the rate of growth obtained for the IT and PIT investigated can not describe the growth in strands of different geometry and composition without making an error. These values are nevertheless useful to have an order of magnitude of the growth of Nb₃Sn at 750, 700 and 650 °C.

9.3 SUPERCONDUCTING PROPERTIES

The superconducting properties of the multifilamentary strands are evaluated after each HT and the Nb₃Sn area is calculated over the entire cross section of the strand. This procedure consent to find a relation between the HT parameters, the superconducting properties and the Nb₃Sn volume and consent to estimate the dimension of the filament that allows the complete the transformation of Nb into Nb₃Sn with the best measured superconducting properties, compatibly with technological and magnetic field quality issues and with the stabilizing properties [72]

I_c measurements are executed after each HT using the experimental set up and criterion described in chapter 6. The measurements are performed for an external magnetic field ranging from 15 T, to 4 T, depending on the maximum transport current value with respect to the power supply. In order to obtain the J_c over the Nb₃Sn area, the Nb₃Sn area and unreacted Nb area are measured over four filaments. The Nb₃Sn area is then calculated assuming a circular geometry of the filaments; the average value is then multiplied by the number of filaments in the strand to obtain the total Nb₃Sn area formed after the HT.

The B_{c20} is evaluated by fitting the I_c data versus magnetic fields, accordingly to Summers parameterization, as described in section 6.7.

The RRR and n value are evaluated after each HT to have an estimate of the Cu matrix contamination and of the homogeneity of the Nb₃Sn filaments [33] in function of the HT parameters.

9.3.1 I_c , J_{cl} , B_{c20} for IT strand

Figure 9.6 shows the I_c measurements for the IT strand in function of the HT time at 750, 700 and 650 °C. The critical current is strongly dependent on the HT parameters and it increases for all the temperatures with increasing the HT time, *i.e.* the Nb₃Sn area. At 750 °C the I_c reaches a plateau after about 20h.

The maximum I_c values are obtained at 750 °C after 40h and at 700 °C after 80h.

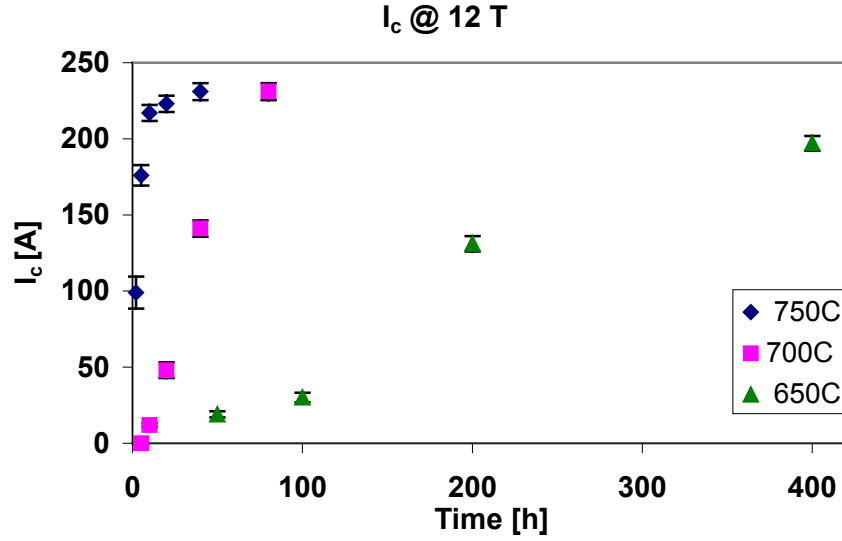


Figure 9.6 I_c for IT strand as a function of HT time at . 750, 700 and 650 °C

The I_c data in function of the Nb₃Sn area are illustrated in figure 9.6 The I_c values for all the temperatures and for short time reaction follow almost the same

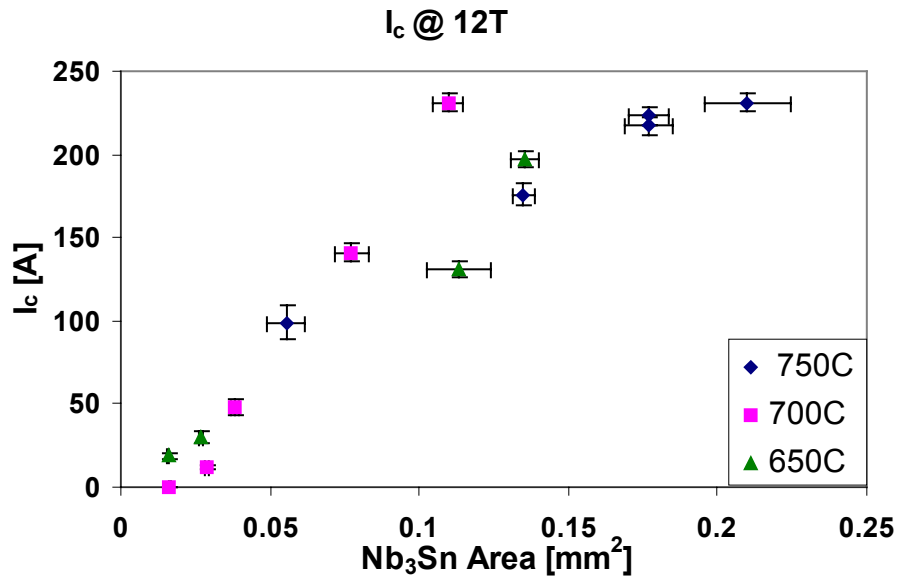


Figure 9.7 I_c for IT strand as a function of Nb₃Sn area formed at 750, 700 and 650 °C.

linear trend. After 2h at 750 °C and after 100h at 650 °C the I_c growth rate decreases and the values of I_c obtained at these temperatures are smaller than the ones obtained at 700 °C with smaller Nb₃Sn area. About the same maximum I_c are

obtained at 700 °C after 80h and at 750 °C after 40h, but the Nb₃Sn area needed at 700 °C is about half the one needed at 750 °C.

It has to be noticed that at 700 °C after 5h the IT strand is not superconducting at any magnetic field even if a layer of 0.6 μm (see Figure 9.3) of Nb₃Sn intermetallic compound formed. At the same temperature after 10h the I_c was measured to be zero above 14T.

Figure 9.8 shows the relation between J_{cl} and the HT time at the three temperatures investigated. It has to be noticed that the maximum J_{cl} is obtained at 700 °C after 80h. This HT is the one that gives also the maximum I_c together with the HT at 750 °C 40h, but it can be observed that for the latter HT the J_{cl} is about half the one for the HT at 700 °C and 80h.

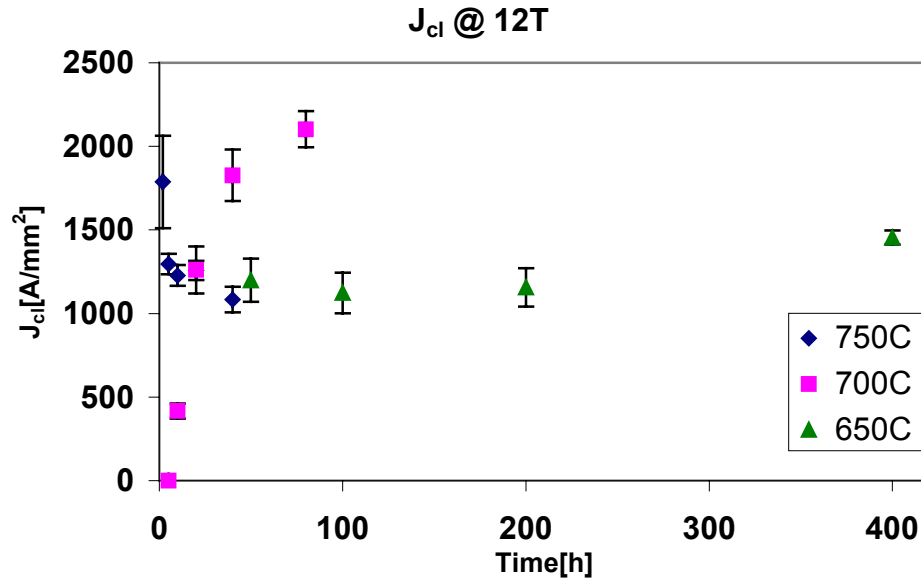


Figure 9.8 J_{cl} for IT strand as a function of HT time at 750, 700 and 650 °C.

At 750 °C the J_{cl} has its peak after the first duration of the HT (2h) and then it decreases with increasing the HT time. A qualitative explanation of this result can be made by taking into account the grain size variation during the Nb₃Sn layer growth. As discussed in section 3.3 grain boundaries are the primary magnetic flux line pinning centers for Nb₃Sn compound hence the growth of the grain dimension with HT time, causing a decrease of the pinning centers number, leads to a decrease of the pinning force [69].

At 650 °C the J_{cl} seems to slightly increase with the HT time. While at 700°C the J_{cl} strongly increases with increasing the HT time. This phenomenon could be related to the initial off-stoichiometry of the Nb₃Sn compound formed at short time reaction at 700 and 650 °C [68]. The off-stoichiometry of the Nb₃Sn compound could also explain the smaller values of the J_{cl} after a short HT time at 650 and 700 °C than at 750°C.

The results found for the J_{cl} are in agreement with the data of the B_{c20} versus time, showed in Figure 9.9. The B_{c20} value for short time reaction at 700 and 650 °C ranges between 19 and 23 T, while increasing the HT time it reaches about 31 T suggesting an initial off stoichiometry composition of the Nb₃Sn compound that approaches to an ordered stoichiometric state when increasing the heat treatment time. The B_{c20} at 750°C is observed to be constant, suggesting that the composition does not significantly change with the HT time

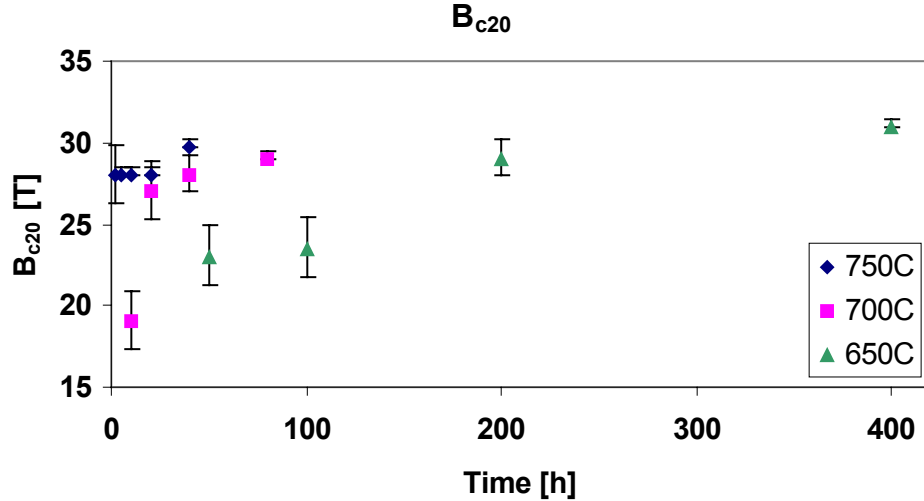


Figure 9.9 B_{c20} for IT strand as a function of HT time at 750, 700 and 650 °C.

Summarizing a qualitative explanation of the J_{cl} trend is related to the different grain growth versus time and temperature and to the Sn deficient composition with respect to the stoichiometry at 700 and 650°C for low reaction time. The values of the J_{cl} and B_{c20} in function of the Nb₃Sn area are shown in Appendix C.

9.3.2 RRR and n value for IT strand

Figure 9.10 shows the RRR data versus HT time at 750, 700 and 650 °C. The RRR decrease with the Nb₃Sn area, *i. e.* with the HT time, and decrease also with

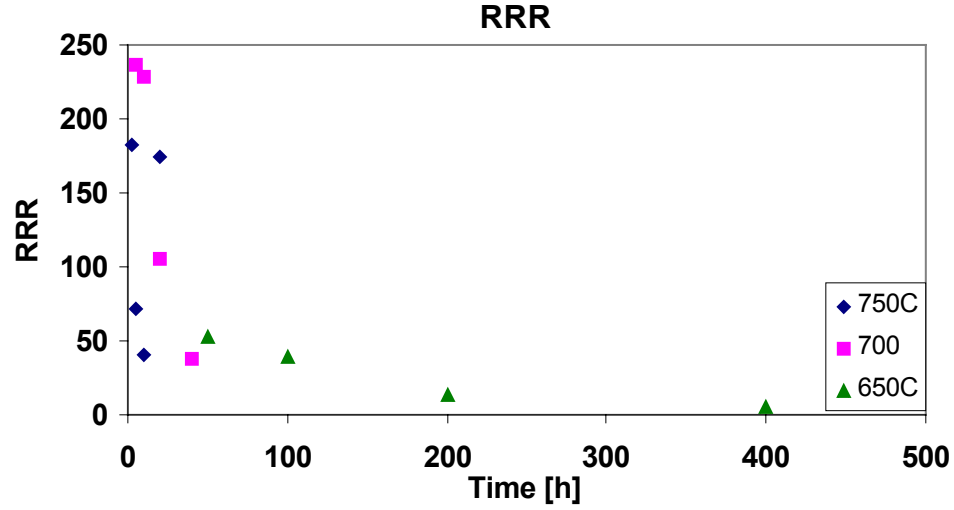


Figure 9.10 RRR for IT strand as a function of HT time at 750, 700 and 650 °C.

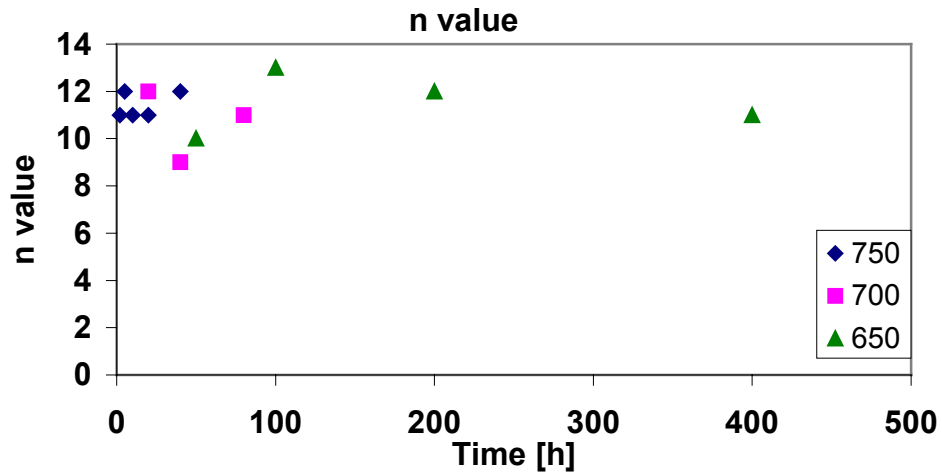


Figure 9.11 n value for IT strand as a function of HT time at 750, 700 and 650 °C.

the temperature for the same Nb₃Sn area, (see Appendix C). The maximum value is obtained at 700 °C after 10h, but its value is still above the required limit of 100 at 700 °C after 40h. It has to be noticed that at 650 °C the RRR is below 100 (see section 3.5, Table 3.8) for all the HT times investigated.

The n value, showed in Figure 9.11 in function of the HT parameters, has a quiet constant trend for all the HT investigated and it seems not to depend on the HT parameters.

9.3.3 I_c , J_{cl} , B_{c20} for PIT strand

Figure 9.12 shows the I_c measured for the PIT strand in function of the HT time at 750, 700 and 650 °C. As observed for the IT strand, the critical current is strongly dependent on the HT parameters and it increases for all the temperatures with increasing the HT time, *i.e.* the Nb₃Sn area. At 750 °C and 700 °C the I_c reaches a plateau at about respectively 20 h and 40 h.

The maximum I_c value of 956 A is obtained at 650 °C after 400h, however this value is similar to the one of 920 A obtained at 700 °C after 80h and to the one of 898 A obtained at the same temperature of 700 °C after half the HT time (40h).

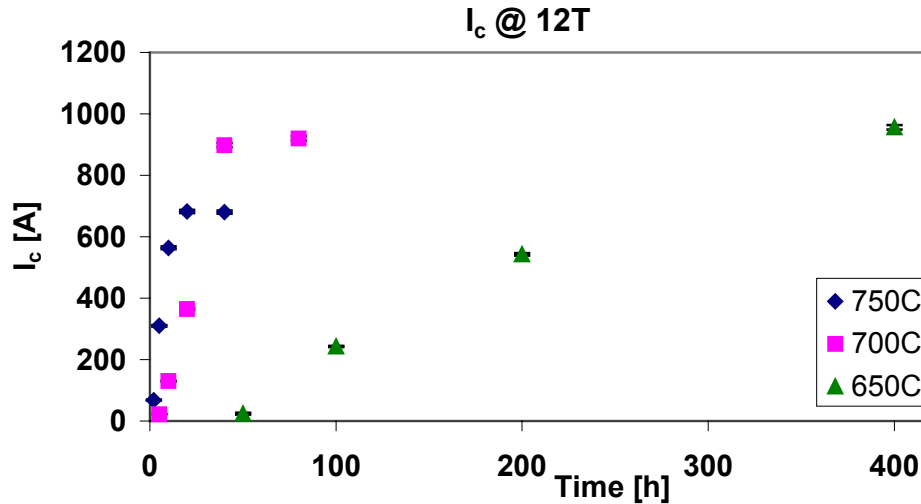


Figure 9.12 I_c for PIT strand as a function of HT time at 750, 700 and 650 °C.

The I_c data in function of the Nb₃Sn area are illustrated in Figure 9.13. The I_c values for all the temperatures and for short time reaction follow with some approximations the same linear trend.

After 10h at 750 °C and after 40h at 700 °C the I_c growth rate decreases. It has to be noticed that even if the Nb₃Sn area at 700 °C after 80h is about equal to the

one obtained at 750 °C after 40h, the I_c obtained for the former HT is significantly bigger than the one obtained for the latter HT. The maximum I_c is obtained at 650 °C after 400 h even if the Nb₃Sn area is smaller than the one formed at 750 °C after 40 h and at 700 °C after 80 h.

Differently from the IT strand the PIT strand is superconducting after 5 h at 700 °C.

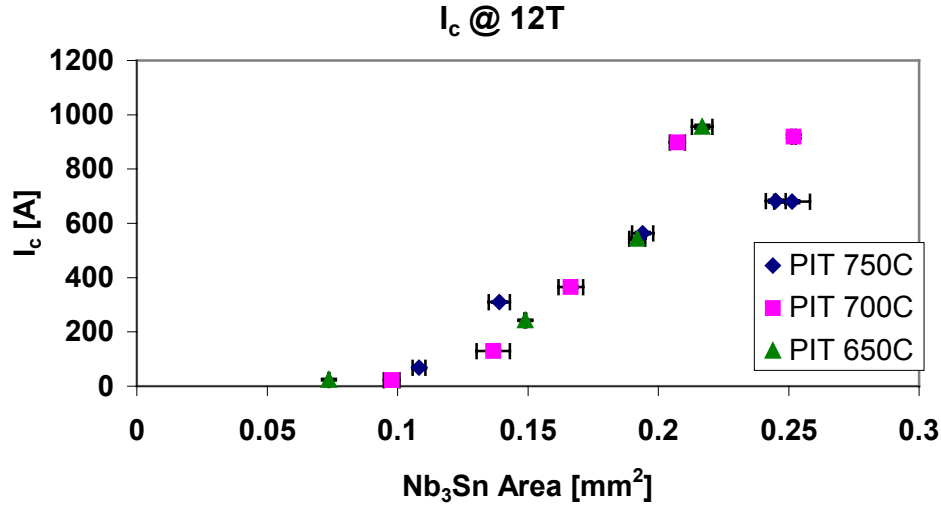


Figure 9.13 I_c for PIT strand as a function of Nb₃Sn area formed at 750, 700 and 650 °C.

Figure 9.14 shows the relation between J_{cl} and the HT time at the three temperatures investigated. It has to be noticed that the maximum J_{cl} is obtained at 650 °C after 400 h, but a similar J_{cl} value is obtained at 700 °C after 40 h. These HT are the ones that gives also the maximum I_c together with the HT at 700 °C and 80 h that gives similar I_c values. For the latter HT however the J_{cl} is significantly smaller than the one obtained at the same temperature after a smaller time reaction.

Both at 750 °C and at 700 °C the J_{cl} increases with the HT time till it reaches a peak and then decreases. A qualitative explanation of the J_{cl} decrease can be made by taking into account the grain size variation during the Nb₃Sn layer growth, as observed for the IT strand at 750 °C.

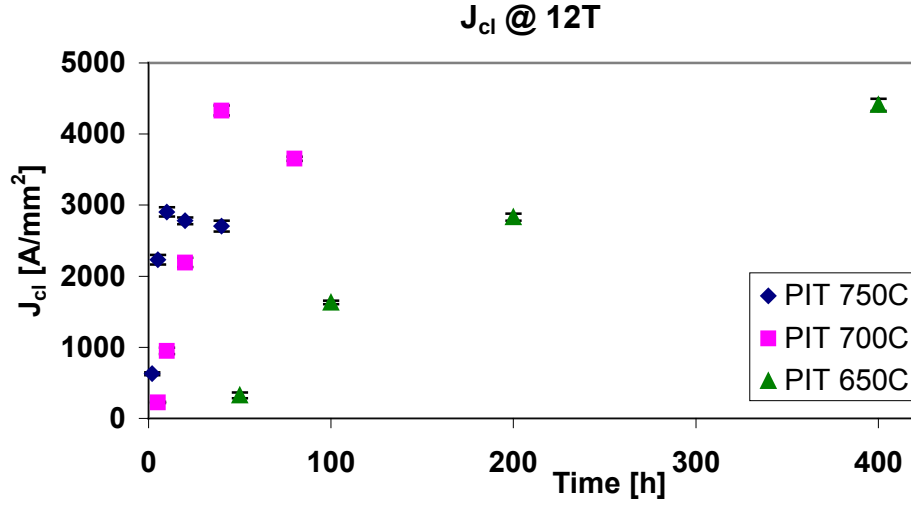


Figure 9.14 J_{cl} for PIT strand as a function of HT time at 750, 700 and 650 °C.

The J_{cl} increase with the HT time, observed at all the temperatures, can be related to the initial off-stoichiometry of the Nb₃Sn compound formed at short time reaction as observed at 700 and 650 °C for the IT strand.

It has to be noticed that the J_c peak value at 750 °C is smaller than the one obtained at 700 °C, as it has been observed for the corresponding I_c values.

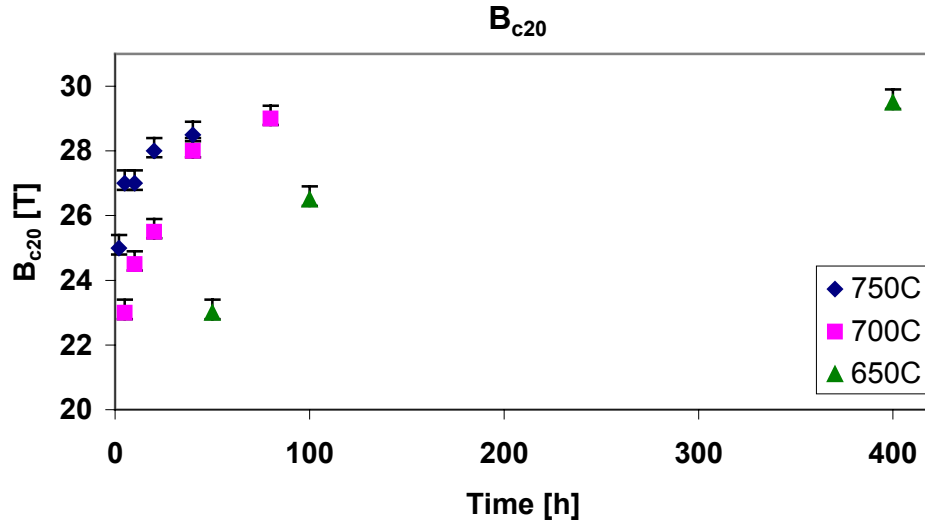


Figure 9.15 B_{c20} for PIT strand as a function of HT time at 750, 700 and 650 °C.

The results found for the J_{cl} are in agreement with the data of the B_{c20} versus time, showed in figure 9.15. The B_{c20} value for short time reaction at all the temperatures ranges between 22 and 25 T, while increasing the HT time it reaches higher values suggesting an initial off stoichiometry composition of the Nb₃Sn compound that approaches to an ordered stoichiometric state when increasing the heat treatment time as observed for the IT strand at 700 and 650 °C.

9.3.4 RRR and n value for PIT strand

Figure 9.16 shows the RRR data versus HT time at 750, 700 and 650 °C. The RRR decreases with the HT time, *i. e.* with the Nb₃Sn area, and decreases also with the temperature for the same Nb₃Sn area, as can be seen from the plot of the RRR in function of the Nb₃Sn area shown in appendix C.

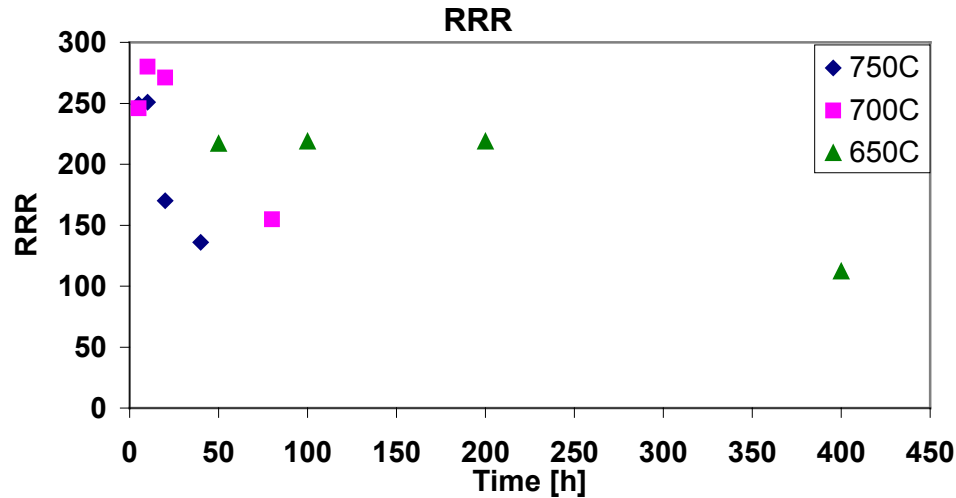


Figure 9.16 RRR for PIT strand as a function of HT time at 750, 700 and 650 °C.

The maximum value is obtained at 700 °C after 10 h as for the IT strand. After this HT the Nb₃Sn thickness is about 7.7 μm, as shown in Table 9.4 and Figure 9.2. It has to be noticed that the RRR value is above the required limit of 100 (see Table 3.8) for all the HT investigated.

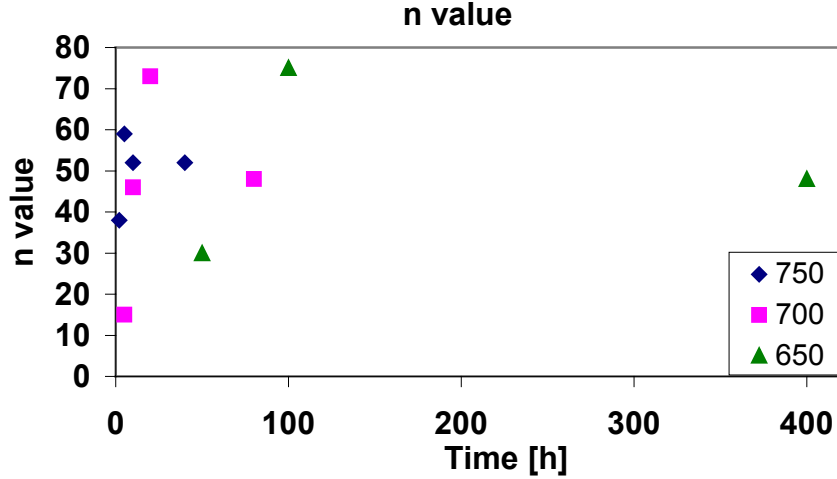


Figure 9.17 n value for PIT strand as a function of HT time at 750, 700 and 650 °C.

The results of the n value, showed in Figure 9.17, suggest that the n value reaches a peak for all the temperatures after a certain HT time and then decreases.

The peak value is obtained for at 700 °C after 10 h, which is the HT that gives also the RRR peak value. In Appendix C the plot of the n value in function of the Nb₃Sn area is shown.

9.3.5 Discussion

It has been observed that both for IT and PIT strand the I_c is determined by the combination of three factors: the Nb₃Sn volume increasing with the HT time and temperature, the composition and the grain dimension of Nb₃Sn.

For the IT strand the I_c increases with the HT time at all the three temperatures, however at 750 °C it approaches to a plateau after a short time reaction (20h) and it possible to suppose that it will decrease at longer time due to the decrease of the J_{cl} with the grain dimensions growth. Therefore the gain in Nb₃Sn volume with the HT time is vanished by the grains growth after a long time reaction.

The maximum value of the I_c is obtained either at 750 °C after 40h and at 700 °C after 80h, but for the latter HT the J_{cl} is almost twice the one obtained for the former HT. Since a big fraction of the Nb filament is still unreacted after 80h at 700 °C it is possible to suppose to obtain a higher I_c for the same strand diameter

by increasing the number and decreasing the diameter of the Nb filaments in order to complete the Nb transformation in Nb₃Sn with the highest J_{cl} at 700 °C and 80h. Since the Nb₃Sn thickness formed after 80h at 700 °C is about 4.4 μm the Nb filament diameter that allows obtaining a higher I_c should be less or equal to 9 μm. This dimension is an estimate affected by the uncertainty that the parameters measured and evaluated for a particular geometry could be not exactly reproducible for other geometry.

Moreover the high J_{cl} and B_{c20} obtained after a very short HT time (2h) at high temperature (750 °C) due to the fast approach to an ordered stoichiometric composition, and the slow grain growth at low temperature (700 and 650 °C) [71] suggest that an improvement in I_c could be obtained by a two stage HT. The first stage at low temperature to convert all the Nb in Nb₃Sn with a fine grain dimension and the second stage at 750 °C for a very short time reaction (less than 2h) to obtain the stoichiometric composition. This procedure should allow to improve the I_c without significant loss in pinning force. The smallest Nb filament should be chosen in this case to allow the Nb complete transformation in Nb₃Sn at low temperature in a very short time in order to have the smallest grain dimensions. However the Nb filament diameter should be higher than 1 μm because below this limit the wire is found to be not superconducting as shown in Figures 9.6 and 9.7. The two stage reaction associated to a small filament diameter would allow also to reduce the HT time (with a 2μm diameter filament less than 40 h at 700 °C and less than 2 h at 750 °C) thus to reduce the cost associated to the “Wind and React” technique. Also the RRR that with one stage HT seems to decrease below the required limit of 100 for HT times longer than 40 h at 700 and 650 °C and than 10 h at 750 °C, should be improved by the short time reaction with the two stage HT.

For the PIT strand the I_c increases with the HT time at all the three temperatures investigated, however at 750 °C it begin slightly decreasing after a short time reaction (20h) and at 700 °C it reaches a plateau after 40h, due to the decrease of the I_c with the grain dimension growth. Thus the gain in Nb₃Sn

volume with the HT time is vanished by the grains growth after a long time reaction as found for the IT at 750 °C after 20 h and suggested for longer time HT at lower temperatures.

The peak value of I_c at 750 °C, obtained after 20h, is well below the one at 700 °C obtained after 80 h. Therefore for the PIT strand is not convenient to perform HT at high temperature (~750 °C) probably due to the fast grain growth.

Two similar maximum I_c values are obtained at 700 °C after 80 h and at 650 °C after 400 h. Also two maximum J_{cl} values are obtained at the same temperatures but after a shorter HT time (40 h) at 700 °C. The time required to obtain the high I_c and J_{cl} at 650 °C is however very long if compared to the ones required at 700 °C. Moreover the *RRR* associated to the HT at 650 °C after 400 h is just above the required limit of 100. For these reasons the HT at 700 °C is preferable to the one at 650 °C.

Since a fraction of the Nb filament is still unreacted after 40 h at 700 °C it is possible to suppose to obtain a higher I_c with the same strand diameter by increasing the number and decreasing the diameter of the Nb filament. As for the IT strand, this procedure should allow to complete the maximum Nb transformation in Nb₃Sn with the highest J_{cl} at 700 °C and 40 h. However a layer of unreacted Nb should be present after the HT to prevent the contamination of the Cu matrix. The estimate of the Nb filament diameter that should lead to an improvement in I_c is evaluated by subtracting the Nb unreacted thickness at 700 °C after 40 h to the filament diameter leaving a margin for the Nb barrier. The unreacted Nb thickness is measured over 6 filaments. The average value is found to be 7 µm. The margin for the Nb barrier is evaluated as 2 µm. This value corresponds to the smallest average unreacted Nb thickness measured among all the HT that leads to an acceptable *RRR*; this value is evaluated at 750 °C after 40h. Since the diameter of the Nb filament is about 50 µm the filament diameter that should allow to obtain an improvement in I_c should be about equal to 40 µm. This dimension is an estimate affected by the uncertainty that the parameters measured

and evaluated for a particular geometry could be not exactly reproducible for other geometry.

9.4 SUMMARY

The growth of the Nb₃Sn intermetallic compound has been related to the HT time at 750, 700 and 650 °C for the two strand technologies IT and PIT with the design parameters specified in Table 5.1 and 3.6. Reference values for the growth rate and for exponent n of the polynomial growth law has been evaluated. With some approximations, mainly due to the different composition of the strand, they can be applied to strands of different design parameters to obtain an estimate of the Nb₃Sn volume versus HT time at the three temperatures investigated.

After each HT the superconducting properties of the wires in terms of I_c , J_{cl} and B_{c20} have been evaluated.

The results of the I_c versus HT allows to optimize the superconducting properties of the two strands investigated if function of the HT parameters. For both the strands technology PIT and IT with large filament design, the HT that gives the highest I_c have been evaluated.

The evaluation of the J_{cl} (calculated over the Nb₃Sn area) and of the B_{c20} is of great interest since it gives the possibility to obtain a qualitative relation between the effects of the grain growth and of the composition changes in function of the HT parameters. The information on the superconducting properties of the wires is therefore obtained independently from the volume of the Nb₃Sn. The HT that leads to the highest J_{cl} is evaluated for both the two strands technology. Thanks to the correlation between the Nb₃Sn volume and the HT parameters it has been possible to obtain an estimate of the filament size for the two strands technology IT and PIT that should lead to an improvement of I_c by the complete transformation of Nb into Nb₃Sn with the highest J_c (leaving a Nb barrier in the PIT strand to prevent the contamination of the Cu matrix).

For the IT technology moreover the possibility to improve the I_c and shorten the HT time has been prospected by performing a two stage HT over fine Nb filaments design IT strands; the first step at low temperature to obtain fine grained Nb₃Sn and the second at high temperature to obtain high B_{c20} values. The achievement of short HT time leads to the reduction of the HT cost for the “Wind and React” approach and should allow also to obtain high RRR values.

CONCLUSIONS

The initial goal of this thesis was to study the kinetics of phase growth during the low temperature HT performed over the superconducting strands focusing the attention to both the superconducting properties, the risk and the cost of this stage. For this purpose measurement of intermetallic thickness were acquired. The experimental set up has been improved and an accurate error evaluation on the data has been performed. This allowed to estimate the growth law for ϵ , δ , η Cu-Sn intermetallic phases in function of the HT parameters. This information consents to best homogenize the Cu-Sn matrix before the Nb_3Sn formation for different IT and MJR strand designs. Moreover important information to prevent the wire structure and the superconducting properties damage during this stage was obtained. The feasibility to perform the low temperature HT before winding has been demonstrated on the strands; this paves the way to reduce the magnet manufacturing cost by the “Prereact-Wind-React” approach.

This first phase lasted about six months mostly due to the very long thermal reaction durations. In a second phase, a strong effort was devoted in investigating the Nb_3Sn growth kinetics and in characterizing the superconducting properties of different strands technologies in order to improve the critical current density for the development of high field accelerator magnets.

The critical current has been optimized in function of the HT parameters for the IT and PIT wires investigated. Moreover the evaluation of the layer critical current density (calculated over the Nb_3Sn area) and of the upper critical field

gave the possibility to obtain the relation between the wires superconducting properties and HT parameters independently from the Nb₃Sn volume. This is of great interest since it allowed to estimate the best Nb filament size in order to improve the wire critical current.

Furthermore the qualitative relation between the effects of the grain growth and of the composition changes in function of the HT parameters addressed towards possible HT cycles to improve the critical current.

APPENDIX A

Results of the fit performed over the Cu-Sn models to evaluate the E and k_0 values.

The thickness data versus HT time and temperature have been fitting minimizing the function using a parabolic growth model (equation 8.3).

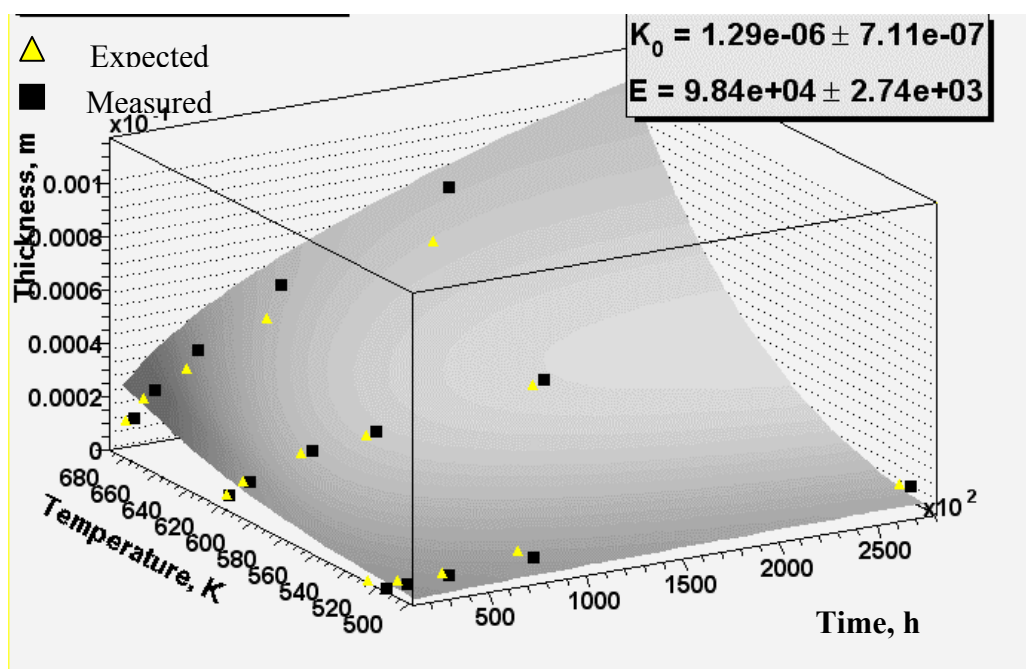


Figure 1 Epsilon phase measured and expected thickness values versus HT time and temperature for $T \geq 240$ °C.

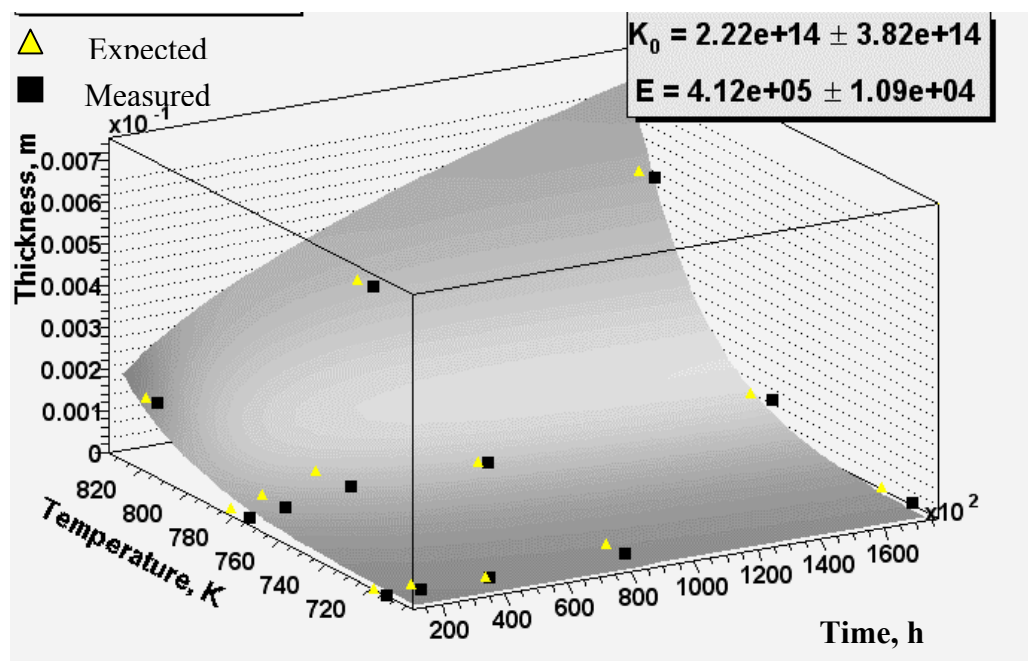


Figure 2 Delta phase measured and expected thickness values versus HT time and temperature for $T \geq 440$ °C.

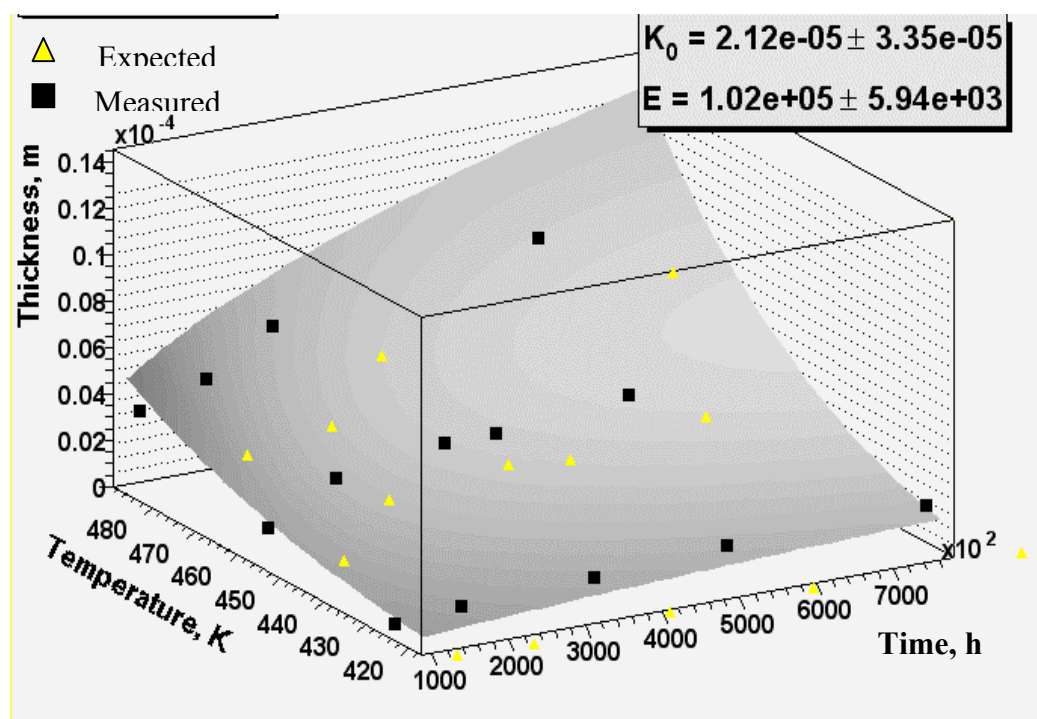


Figure 3 Eta phase measured and expected thickness values versus HT time and temperature for $T \leq 210$ °C.

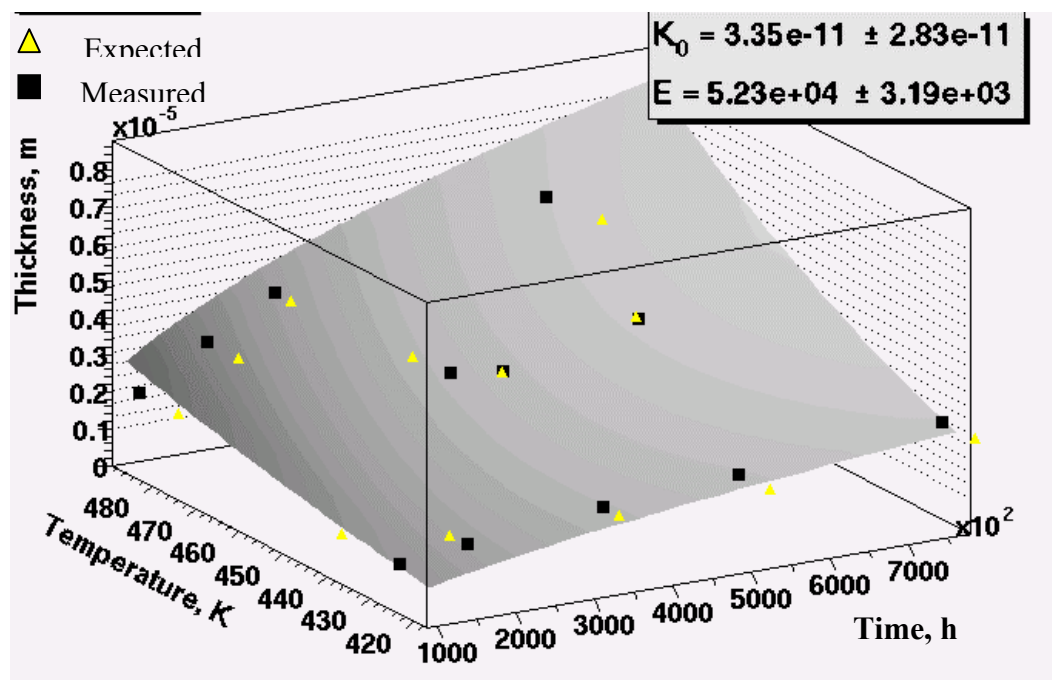


Figure 4 Epsilon phase measured and expected thickness values versus HT time and temperature for $T \geq 240$ °C.

APPENDIX B

Results the growth kinetic investigation performed over the MJR strand.

The thickness data versus HT time and temperature have been acquired for 210 and 240 °C; above these temperatures the ϵ phase reaches the Nb filaments and it is not possible to measure its thickness.

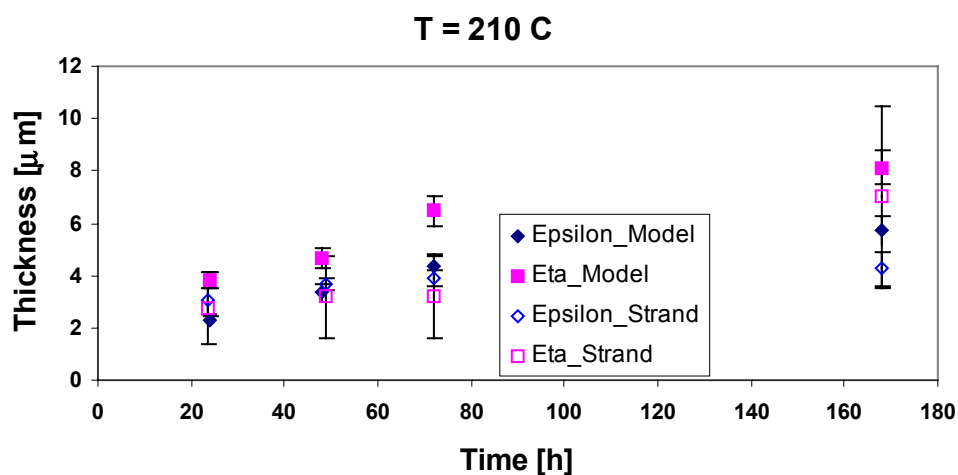


Figure 1 Epsilon and Eta phase growth in the MJR strand and in the Cu-Sn models at 210 °C.

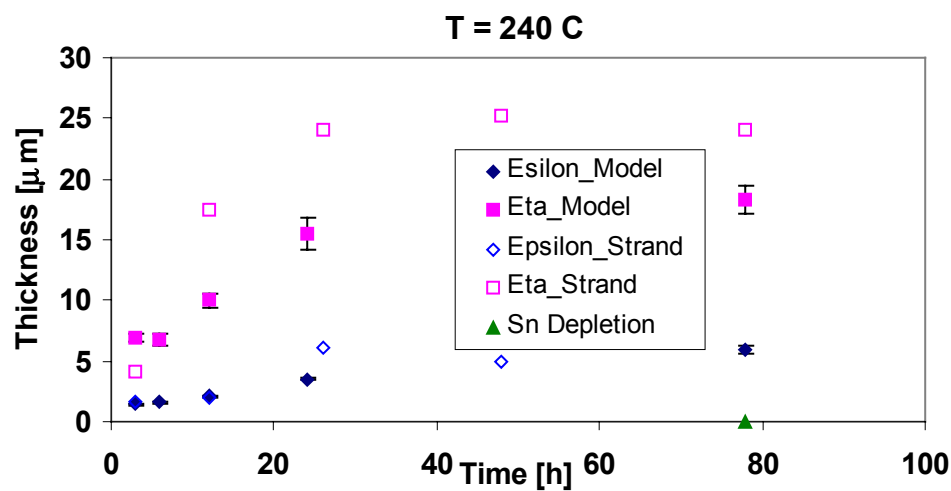


Figure 2 Epsilon and Eta phase growth in the MJR strand and in the Cu-Sn models at 240 °C.

APPENDIX C

Superconducting properties measured and evaluated on IT and PIT strands (which characteristics are given in Table 5.1 and 3.6) in function of the Nb_3Sn area formed after HT.

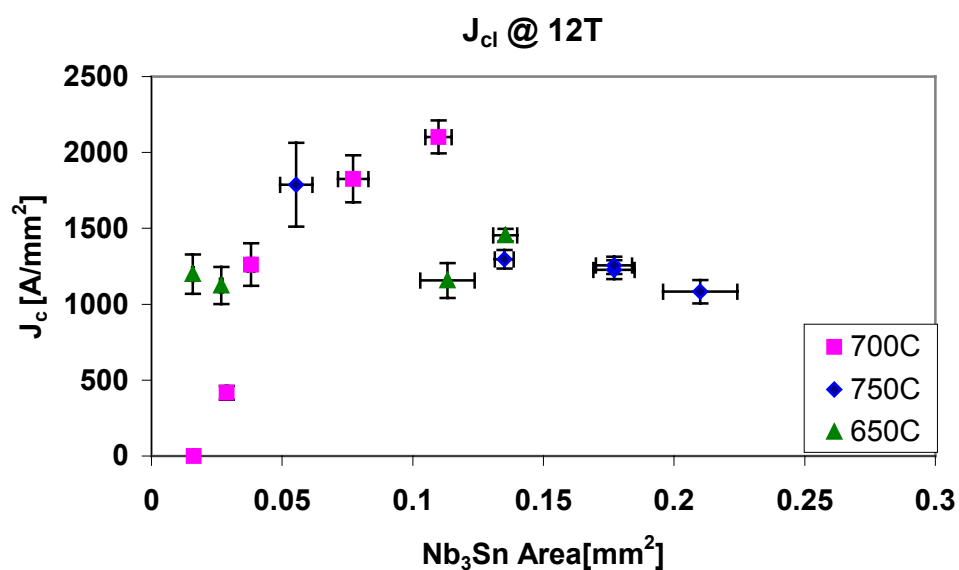


Figure 1 J_{cl} for IT strand as a function of Nb_3Sn area formed after different HT time and temperature (T).

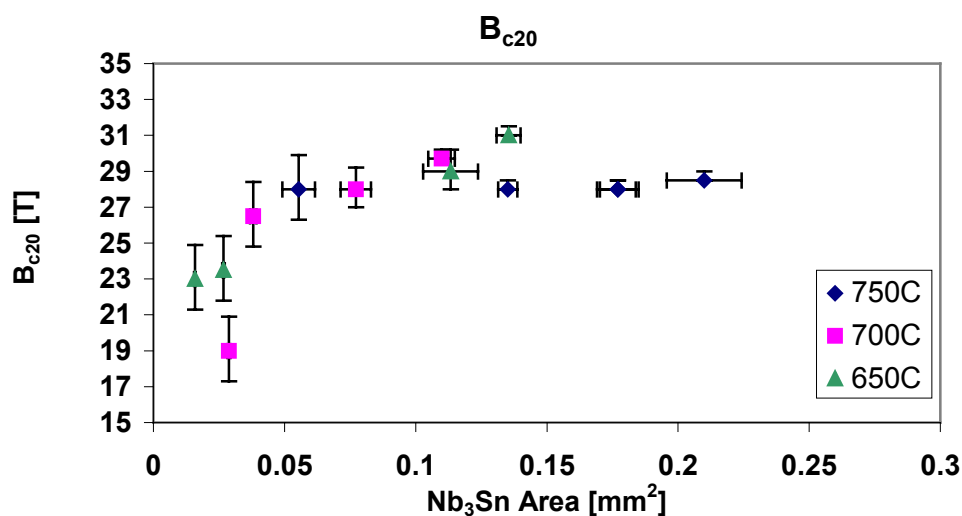


Figure 2 B_{c20} for IT strand as a function of Nb_3Sn area formed after different HT time and temperature (T).

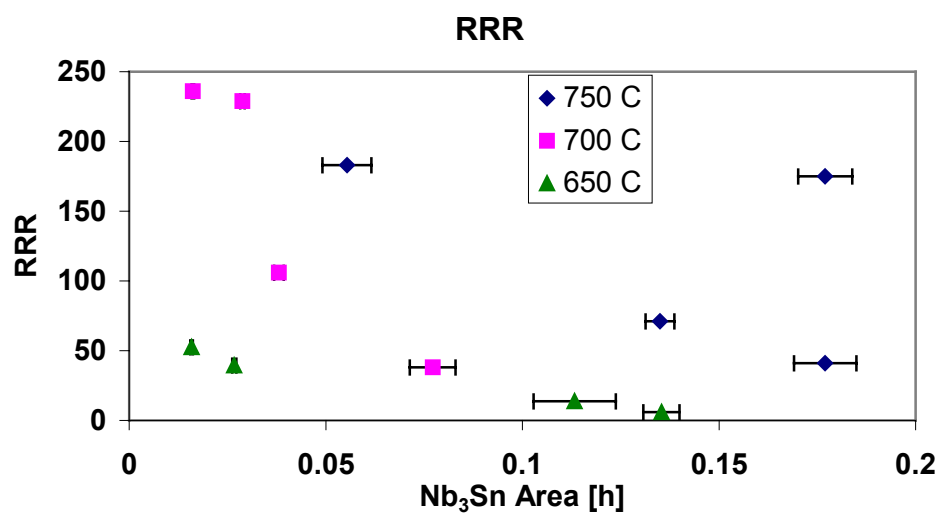


Figure 3 RRR for IT strand as a function of Nb₃Sn area formed after different HT time and temperature (T).

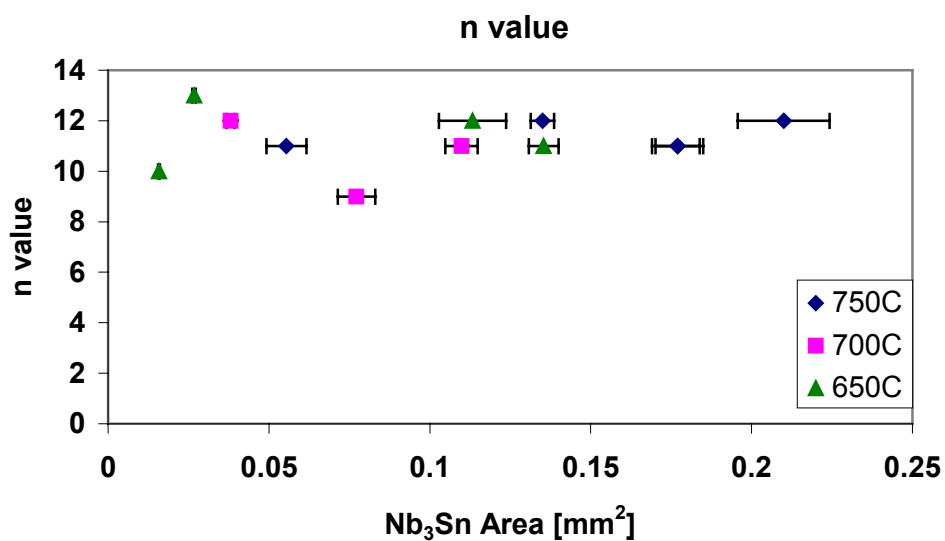


Figure 4 *n* value for IT strand as a function of Nb₃Sn area formed after different HT time and temperature (T).

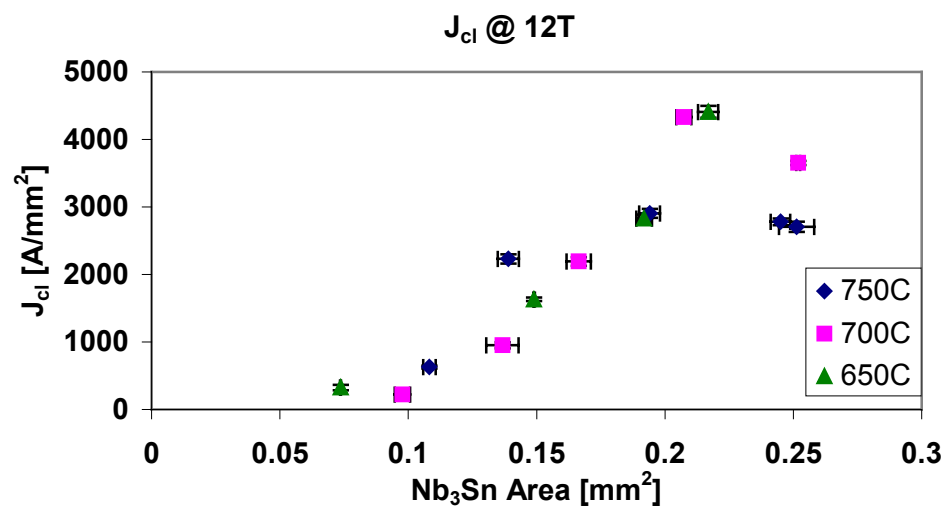


Figure 5 J_{cl} for PIT strand as a function of Nb_3Sn area formed after different HT time and temperature (T).

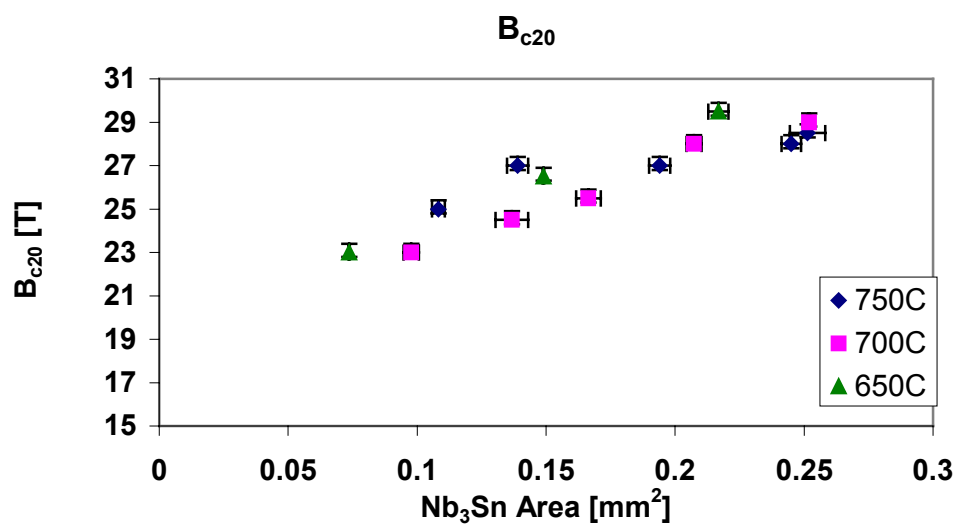


Figure 6 B_{c20} for PIT strand as a function of Nb_3Sn area formed after different HT time and temperature (T).

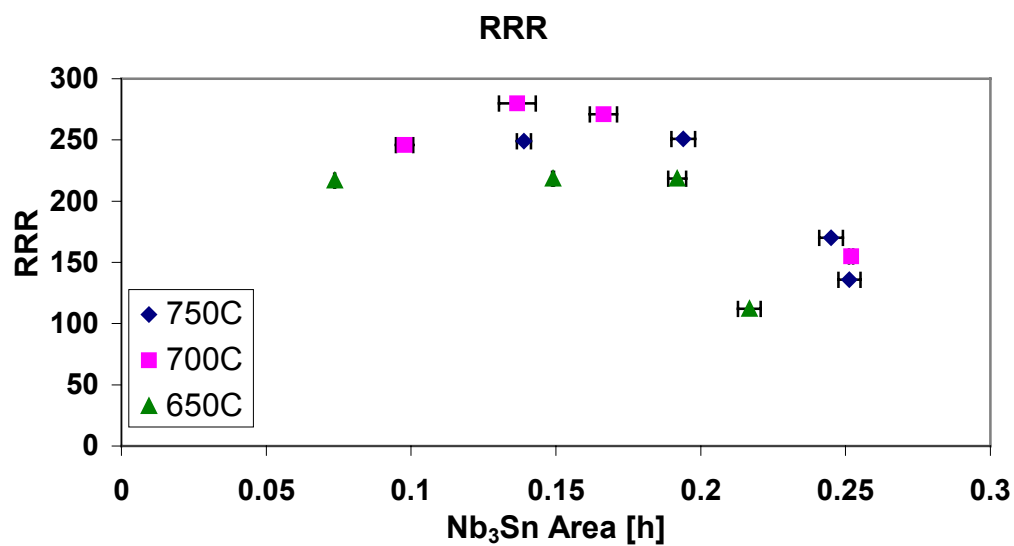


Figure 7 RRR for PIT strand as a function of Nb₃Sn area formed after different HT time and temperature (T).

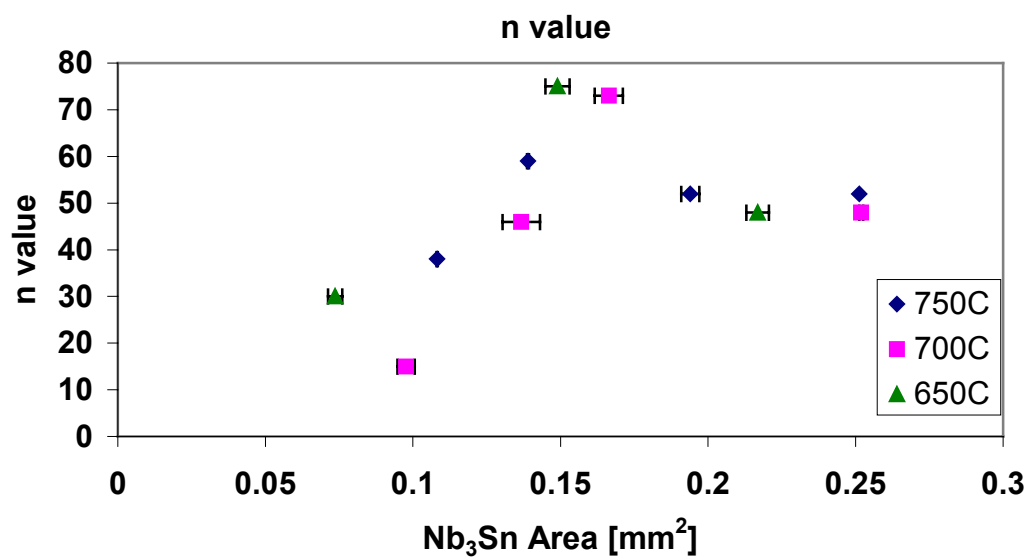


Figure 8 *n* value for PIT strand as a function of Nb₃Sn area formed after different HT time and temperature (T).

BIBLIOGRAPHY

- [1] E. Malamud, *The Very Large Hadron Collider*, FERMILAB-Conf-98/274
September 1998
- [2] P.J. Limon, *VLHC R&D at Fermilab*, Physics Accelerator Conference 1998
- [3] R. Yamada, *25-TeV center of Mass Hadron Collider in VLHC Booster
Tunnel*, Fermilab FN-681, May 1999
- [4] VLHC Design Study Group, *Design Study for a Staged Very Large Hadron
Collider*, FERMILAB-TM-2149 June 2, 2001
- [5] S. Feher, *Superconducting Accelerator Magnets*, GSA Summer School
August 1999
- [6] G. Vidali, *Superconductivity the Next Revolution?*, Cambridge University
Press (1993)
- [7] Rudolf de Bruyn Ouboter, *Heike Kamerlingh Onnes's Discovery of
Superconductivity*, Scientific American (1997)
- [8] H. Kamerlingh Onnes: Leiden Comm. **122b**, 124 (1911)
- [9] P. Grassman, Phys. Z., **37**, 569 (1936)
- [10] H. Kamerlingh Onnes: Leiden Comm. **139**, (1914)
- [11] W. Meisser, R. Ochsenfeld: Naturwiss. **21**, 787 (1933).
- [12] F. London, H. London: Proc. Roy. Soc. **A149**, 71 (1935)

- [13] F. London: Proc. Roy. Soc. A152, 24 (1935); Phys. Rev. **74**, 562 (1948)
- [14] V. L. Ginzburg, L. D. Landau: Zh. Eksp. Teor. Fiz. **20**, 1064 (1950).
- [15] L. D. Landau, E. M. Lifshitz: Statistical Physics, 3rd edn., part 1 (Nauka, Moscow 1976) [English transl.: Pergamon Press, Oxford 1980].
- [16] A. A. Abrikosov: Zh. Eksp. Teor. Fiz. **32**, 1442 (1957) [English transl.: Sov. Phys. JETP **5**, 1174 (1957)].
- [17] J. Bardeen, L. Cooper, J. Schrieffer, *Theory of Superconductivity*, ed. by N. N. Bogolyubov, p. 103 (Inostrannaya Literatura, Moscow 1960).
- [18] Terry P. Orlando, Kevin A. Delin, *Foundations of Applied Superconductivity*, Addison Wesley (1990)
- [19] V. V. Schmidt, *The Physics of Superconductors*, Springer
- [20] W. J. de Haas and J. Voogd, Leiden Communication, **208 b** (1930)
- [21] A. A. Abrikosov, JETP, **32**, 1442, (1957)
- [22] L. P. Gor'kov, JETP, **37**, 835 (1959)
- [23] *Superconductor Material Science*, S. Foner, B. B. Schwartz, Plenum Press, N. Y., (1981)
- [24] C.P. Bean, Phys. Rev. Lett. **8**, 250 (1962)
- [25] Martin N. Wilson, *Superconducting Materials for Magnets*, CERN Accelerator School on Superconductivity in Particle Accelerators, pp. 47-70 (1996)
- [26] R.M. Scanlan, D.R. Dietderich, and H.C. Higley, *Conductor Development for High Field Dipole Magnets*, Magnet Technology Conference, MT16, September (1999)
- [27] R. Flukiger, *Atomic Phase Stability and Superconductivity in Bulk and Filamentary Al5 Type Compounds*, PHD Thesis
- [28] N. Andreev, E. Barzi, D.R. Deepak, S. Mattafirri, A. V. Zlobin, *Volume expansion of Nb₃Sn strands and cables after heat treatment*, ICMC (2001)
- [29] Fred M. Asner, *High Field Superconducting Magnets*, Oxford Science Publications (1999)

- [30] C. Boffo, *Magnetization Measurements at 4.2 K of Multifilamentary Superconducting Strand*, Technical Division TD-99-074 Fermilab, December (1999)
- [31] C. S. Pande and M. Suenaga, *A Model of Flux Pinning by a Grain Boundaries in Type-II Superconductors*, Applied Physics Letters, vol. 29 (1976)
- [32] E. Gregory, *Practical Fabrication Method for Nb₃Sn*, IEEE, vol. 77, 8 (1989)
- [33] E. Barzi, G. Ambrosio, P. Bauer, J. -M. Rey, R. Yamada, A. Zlobin, *Progress Report on Strand and Cable R&D*, Technical Division TD-01-013 Fermilab, February (2001)
- [34] E. Gregory, E. Gulko, T. Pyon, and L. F. Goodrich, *Properties of Internal Tin Nb₃Sn Strand for the International Thermonuclear Experimental Reactor*, *Advances in Cryogenic Engineering*, vol. 42 (1996)
- [35] Ryuji Yamada, *Summary report on PIT type conductor*, Fermilab Technical Division internal report, July 8th (1999)
- [36] J.H. Lindenhovius, E.M. Hornsvelt, A.den Ouden, W.A.J. Wessel, and H.H.J. ten Kate, *Progress in the Development of Nb₃Sn Conductors based on the "Powder in Tube" Method with Finer Filaments*, IEEE Trans. on Applied Superconductivity **9**, 1451 (1999)
- [37] D. R. Chichili, N. Andreev, E. Barzi, V.V. Kashikhin, I. Terechkine, S. Yadav, R. Yamada, and A. V. Zlobin, *Nb₃Sn Cos(θ) Dipole Magnet, HFDA-02 Production Report*, Technical Division TD-01-036, May (2001)
- [38] *Intermetallic Compounds, Principles*, vol.1. Edited by J.H. Westbrook and R.L. Fleischer, (1994)
- [39] R. E. Reed-Hill, *Physical Metallurgy Principles*, Reza Abbaschian, PWS Publishing Company, Boston (1991)
- [40] V. M. Falchenko, L. N. Larikov and V. R. Ryabov, *Diffusion Process in Solid-Phase Welding of Materials*, Mashinostroenie Publishers, Moscow, (1975)
- [41] G. Tamman and J. J. Rocha, *Zeit. Fur. Anorg. Chemie*, **199**, 289 (1931)

- [42] G. V. Raynor, J. Less-Common Metals, **29** (1972)
- [43] T. S. Luhman, O. Horigami, and D. D. Hughes, Appl. Polymer Symp., **29**, 61 (1971)
- [44] M. Suenaga, O. Horigami, and T.S. Luhman, *Effects of Sn concentration on the critical current density of Nb₃Sn at the Nb-(Cu-Sn alloy) interface*, Applied Physics Letters, **25**, 10, (1974)
- [45] H. H. Farrel and G. H. Gilmer, *Grain Boundary Diffusion and Growth of Intermetallic Layers: Nb₃Sn*, Applied Physics Letters., **45**, 9 (1974)
- [46] J. Goldstein, D. Newbury, P. Echlin, D. Joy, A. Romig, C. Lyman, C. Fiori, E. Lifshin, *Scanning Electron Microscopy and X-Ray Microanalysis II* Edition, Plenum Press, New York and London, (1991)
- [47] E. Barzi, C. Boffo, J.P. Ozelis, *J_c Measurements at the short sample test facility*, Technical Division TD-98-057 Fermilab, (October 1998)
- [48] L.T. Summer, M.M.W. Guinan, J.R. Miller, P.A. Hahn, A model for the prediction of Nb₃Sn critical current as a function of field, temperature, strain and radiation damage, IEEE Trans. Magn., **27** (2): 2041-2044, (1991)
- [49] E. Barzi *Error Analysis of Short Sample J_c at the Short Sample Test Facility*, Technical Division TD-98-055, (September 1998).
- [50] S. Mattafirri, E. Barzi, J.-M. Rey, F. Fineschi, Kinetics of phase growth in the Cu-Sn system and application to composite Nb₃Sn strands, submitted ASC (2002)
- [51] J. M. Rey, E. Barzi, S. Mattafirri, J. Hoffman, R. Yamada, *Effect of Partly Reacting Nb₃Sn before Magnet Winding on the Strand Critical Current*, CEC/ICMC, (2001)
- [52] E. Barzi, C. Boffo, D. R. Chichili, J. P. Ozelis, R. M. Scanlan, H. C. Higley, and A. V. Zlobin, *Study of Strand Critical Current Degradation on a Rutherford Type Nb₃Sn Cable*, Cryogenic Engineering Conference, July 1999
- [53] E. Barzi, G. Abrosio, N. Andreev, D. Chichili, M. Fratini, L. Elementi, J. Hoffman, P. J. Limon, S. Mattafirri, J.-M. Rey, R. Yamada, A. V. Zlobin,

Superconductor and Cable R&D for High Field Accelerator Magnets at Fermilab, CEC/ICMC, (2001)

- [54] N. Andreev, E. Barzi, E. Borissov, D. Chichili, L. Elementi, S. Mattafirri, R. Yamada, A. Zlobin, *Assessment of Nb₃Sn Strands for High Field Accelerator Magnets at Fermilab* submitted ASC (2002)
- [55] S. Dabritz, D. Bergner and V. Hoffmann, *Phase Growth Between Copper and Different Tin Solders*, Diffusion in Materials, pp:579-584 (1997)
- [56] S. Dabritz, V. Hoffmann, G. Sadowski and D. Bergner, “*Investigations of Phase Growth in the Copper-Tin System*”, Diffusion in Materials, pp:1575-1580 (2001)
- [57] K. F. Dreyer, W. K. Niels, R.R. Chromik, D. Grosman, and E.J. Cotts, *Calorimetric study of the Energetics and Kinetics of interdiffusion in Cu/Cu₆Sn₅ Thin Film Diffusion Couples*, Diffusion in Materials, pp:579-584 (1997).
- [58] R.R. Chromik and E. J. Cotts, *Thermodynamic and Kinetic study of phase transformations in solder/metal systems*, Mat. Res. Soc. Symp. Proc. Vol. 445, pp. 31-36 (1997)
- [59] M.T. Naus, P.J. Lee, D.C. Larbalestrier, *The interdiffusion of Cu and Sn in Internal Sn Nb₃Sn Superconductors*, IEEE Transactions on Applied Superconductivity, vol. 10 (1), pp.983-987 (2000)
- [60] B.A. Glowacki, *Changes of T_c, J_c and Stoichiometry of Nb₃Sn Phase Formed During Internal Tin Diffusion Process*, IEEE Trans. Magn., **32** (1996)
- [61] M.T. Naus, P.J. Lee and D. C. Larbalestrier, *The influence of the starting Cu-Sn phase on the Superconducting Properties of Subsequently Reacted Internal-Sn Nb₃Sn Conductors*, IEEE Transactions on Applied Superconductivity, vol. 11, p.3569 (2001)
- [62] R. Taillard and C. Verwaerde, *Phase Transformations during the manufacturing process of Nb₃Sn superconducting composites* Proc. Euromat95, Venice, pp 471-474 (1997)

- [63] D. R. Chichili, N. Andreev, E. Barzi, V.V. Kashikhin, I. Terechkine, S. Yadav, R. Yamada, and A. V. Zlobin, *Nb₃Sn Cos(θ) Dipole Magnet, HFDA-02 Production Report*, Technical Division TD-01-036, May 2001
- [64] E. Barzi and J.M. Rey *Risk of Sn Burst in Superconducting Nb₃Sn Strands during Reaction Cycle*, Technical Division TD-01-010, August 2001 Euromat95, Venice, pp 471-474, 1995
- [65] M.T. Nauss, M.C. Jewell, P.J. Lee and D.C. Larbalestrier Lack of Influence of the Cu-Tin mixing Heat Treatment on the Superconducting Properties of two High-Nb Internal-Tin Nb₃Sn Conductors, IEEE Trans on applied superconductivity
- [66] M. Suenaga, O. Horigami, and T.S. Luhman, *Effects of Sn concentration on the critical current density of Nb₃Sn at the Nb-(Cu-Sn alloy) interface*, Applied Physics Letters, **25**, No 10, (1974).
- [67] R. Flukiger, *Atomic ordering, phase stability and superconductivity in bulk and filamentary A15 type compounds*
- [68] W. Schauer and W. Schelb, *Improvement of Nb₃Sn high field critical current by a two stages reaction*, IEEE Trans. Magn., **17**, (1981).
- [69] L. D. Cooley and P. J. Lee, Shift of flux-pinning force curve in Nb₃Sn thin films with very fine grain size, (2000),
- [70] A.W. West, R.D. Rawlings, *A transmission electron microscopy investigation of filamentary superconducting composites*, Journal of Materials Science 12, (1977)
- [71] J.D.Livingstone, *Grain size in A-15 reaction layers*, Phys. Stat. Sol. **44**, 295 (1977)
- [72] V.V. Kashikhin and A.V. Zlobin, *Correction of the persistent current effect in Nb₃Sn dipole magnets*, ASC (2000)